Scramjet Operability Range Studies of an Integrated Aerodynamic-Ramp-Injector/Plasma-Torch Igniter with Hydrogen and Hydrocarbon Fuels

Aristides M. Bonanos

Dissertation submitted to the Faculty of the
Virginia Polytechnic Institute and State University
In partial fulfillment of the requirements for the degree of

Doctor of Philosophy
In
Aerospace Engineering

Joseph A. Schetz, Chair
Walter F. O'Brien
Christopher P. Goyne
Richard W. Barnwell
Joseph J. Wang

August 2005
Blacksburg, Virginia

Keywords: **Scramjets, Supersonic Combustion, Aeroramp Mixing and Injection, Hypersonic Propulsion, Plasma Torch**

Scramjet Operability Range Studies of an Integrated Aerodynamic-Ramp Injector/Plasma Torch Igniter with Hydrogen and Hydrocarbon Fuels

Aristides M. Bonanos

Abstract

An integrated aerodynamic-ramp-injector/plasma-torch-igniter of original design was tested in a $M_\infty = 2$, unvitiated, heated flow facility arranged as a diverging duct scramjet combustor. The facility operated at a total temperature of 1000 K and total pressure of 330 kPa. Hydrogen (H_2), ethylene (C_2H_4) and methane (CH_4) were used as fuels, and a wide range of global equivalence ratios were tested. The main data obtained were wall static pressure measurements, and the presence of combustion was determined based on the pressure rises obtained.

Supersonic and dual-mode combustion were achieved with hydrogen and ethylene fuel, whereas very limited heat release was obtained with the methane. Global operability limits were determined to be $0.07 < \varphi < 0.31$ for hydrogen, and $0.14 < \varphi < 0.48$ for ethylene. The hydrogen fuel data for the aeroramp/torch system was compared to data from a physical 10^o unswept compression ramp injector and similar performance was found with the two arrangements. With hydrogen and ethylene as fuels and the aeroramp/plasma-torch system, the effect of varying the air total temperature was investigated. Supersonic combustion was achieved with temperatures as low as 530K and 680K for the two fuels, respectively. These temperatures are facility/operational limits, not combustion limits.

The pressure profiles were analyzed using the Ramjet Propulsion Analysis (RJPA) code. Results indicate that both supersonic and dual-mode ramjet combustion were achieved. Combustion efficiencies varied with φ from a high of about 75% to a low of about 45% at the highest φ. With a theoretical diffuser and nozzle assumed for the configuration and engine, thrust was computed for each fuel. Fuel specific impulse was on average 3000 and 1000 seconds for hydrogen and ethylene respectively, and air specific impulse varied from a low of about 9 sec to a high of about 24 sec (for both fuels) for the $T_o = 1000K$ test condition.

The GASP RANS code was used to numerically simulate the injection and mixing process of the fuels. The results of this study were very useful in determining the suitability of the selected plasma torch locations. Further, this tool can be used to determine whether combustion is theoretically possible or not.

Acknowledgements

First and foremost I would like to thank my family for their support, encouragement and patience throughout my studies. Without them, this would not be possible.

I would like to thank my advisor, Dr. Joe Schetz, for giving me the opportunity to work on such an interesting and educational project. His guidance, advice and experience were vital during this research and helped make it ultimately a success. I would also like to thank Dr. Walter O'Brien for his insights regarding the plasma torch and Dr. Chris Goyne for his help with the experimental work.

Special thanks to my research partner Darius Sanders for accompanying me on the endless trips to UVA for more results! Thanks to Steve Edwards for making everything that didn't work, work and to the AOE machine shop and main office staff for putting up with my endless requests.

There are many people to thank and, unfortunately, listing all of them is impossible. However, certain people need to be mentioned individually. Thanks to my roommate and good friend Laki Lambros for making the time at Blacksburg more enjoyable. My friends Joe, Joey, Tim and Ignacio for their support. All my friends from the Aerospace department and the Greek community in Blacksburg for the memories they have given me.

TABLE OF CONTENTS

LIST OF FIGURES

LIST OF TABLES

Nomenclature

A	=	Area
C_f	=	Skin-friction coefficient
C_p	=	Specific heat capacity at constant pressure
d	=	Diameter
E_a	=	Activation energy
$\mathscr{F}$	=	Thrust
FSR	=	Fuel-to-air stoichiometric ratio
h	=	Altitude
h	=	Film coefficient
I	=	Plasma torch current
I_{sp}	=	Fuel specific impulse
k	=	Thermal conductivity
L	=	Combustor length
M	=	Mach number
$\dot{m}$	=	Mass flow rate
n	=	Number of injectors in aeroramp array
$\mathscr{P}$	=	Torch power
P or p	=	Pressure
PCE	=	Combustor exit pressure (RJPA notation)
Pr	=	Prandtl number
PSPCI	=	Pre-combustion shock pressure rise (RJPA notation)
Q	=	Heat loss due to combustor wall cooling
$\bar{q}$	=	Jet-to-freestream momentum flux ratio
R	=	Gas constant
r	=	Recovery factor
Re	=	Reynolds number
S_a	=	Air-specific impulse
T	=	Temperature
t	=	Wall thickness
u	=	Velocity magnitude
V	=	Plasma torch voltage

Greek

α	=	Mass fraction concentration
γ	=	Ratio of specific heats
η_c	=	Combustion efficiency
ρ	=	Density
φ	=	Equivalence ratio

Subscripts

a,w	=	Adiabatic wall
e	=	Boundary layer edge condition
eq	=	Equivalent (referring to diameters)
j	=	Jet property
o	=	Stagnation condition
w	=	Wall condition
∞	=	Freestream condition

C h a p t e r 1

1. Introduction and Literature Review

1.1. Introduction – Ramjets and Scramjets

Throughout the history of aviation, propulsion devices aimed at propelling vehicles in the atmosphere higher and faster have been built, extending the flight speed envelope. The evolutionary path of engines has gone through many steps, from propellers to turbojets, turbofans, ramjets and finally to scramjets. Their common attribute is that they all rely on atmospheric air to achieve thrust, and hence are called airbreathing. Each iteration yields a more efficient design capable of higher thrust levels and speeds.

Cheaper access to space is a strong driving force in the hypersonic industry. Designing a launch vehicle capable of achieving single-stage to orbit is the ultimate goal. However, for a vehicle to reach orbit, it must first fly at hypersonic velocities. From a cycle-efficiency viewpoint, airbreathing engines are much superior to other types of chemical propulsion engines because they use the oxygen from the atmospheric air [Ferri, 1973]. This also makes sense from a systems perspective, since not carrying onboard the fuel oxidizer allows for a larger payload [Heiser, 1994].

The idea of using the pressure increase associated with decelerating air as it enters an inlet to achieve thrust is not a new one. The ramjet was proposed as early as 1913, by Renè Lorin of France [Heiser, 1994], however its development at that time was not pursued due to its inability to produce thrust at static and low speed conditions. A schematic of the ramjet is presented in Figure 1.1. The flow is compressed by passing through a series of oblique shocks, terminating in a normal shock. Fuel is then injected into the subsonic flow and combustion occurs. The products are accelerated through a converging-diverging nozzle to produce thrust.

At flight Mach numbers above the 3-6 range, decelerating the flow to subsonic conditions for combustion will produce temperatures that will melt most known materials [Heiser, 1994]. Further, the increased temperatures cause combustion products to dissociate, limiting the temperature rise that can be obtained in the engine and reducing thermal

efficiency [Dugger, 1970, Gilreath, 1990]. The burner entry pressure is the highest pressure to be found in the engine, and mechanical and thermal loads increase with increasing pressure [Heiser, 1994]. Decelerating the flow to subsonic conditions would cause large pressures in the combustor, leading to increased weight to withstand the structural loads [Kutschenreuter, 2000].

To reach higher Mach numbers, the heat addition from combustion into the engine flow must occur at supersonic velocities. This allows for maximum potential flight Mach numbers, say for hydrogen fuel, between 25 and 30 to be reached [Ferri, 1973]. Thus, the supersonic combustion ramjet engine, or scramjet, becomes the necessary alternative for hypersonic flight applications [Ferri, 1960, Ferri, 1964, Swithenbank, 1966, Dugger, 1970, Ferri, 1973, Heiser, 1994].

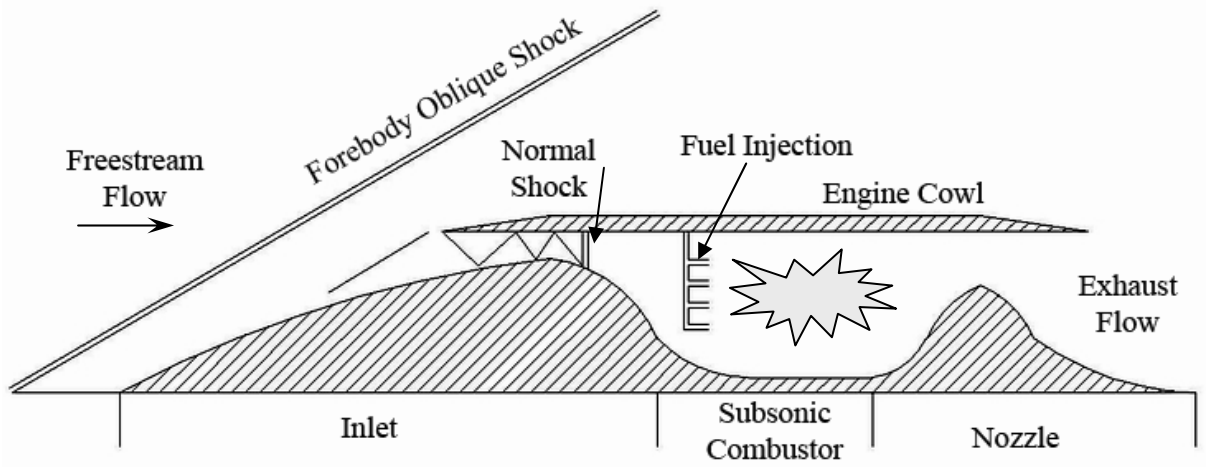

Figure 1.1. Schematic diagram of a ramjet engine.

A schematic of a scramjet is shown in Figure 1.2. Flow is compressed and decelerated through a series of oblique shocks, however fuel injection and combustion occur while the flow is still supersonic. Products are again expanded through a diverging nozzle, and thrust is obtained. The problem with this configuration is that a large enough pressure rise in the combustor may lead to inlet unstart. The solution to this was the addition of a constant area section ahead of the combustor, called the isolator, and the development of the dual-mode combustion ramjet. The isolator contains the oblique shock train preventing unstart. Its function is to produce inlet conditions for the combustor anywhere between the inlet freestream and those of a normal shock ahead of the combustor. Dugger and Billig [1959] were the first to report experiments were positive thrust was produced from supersonic combustion.

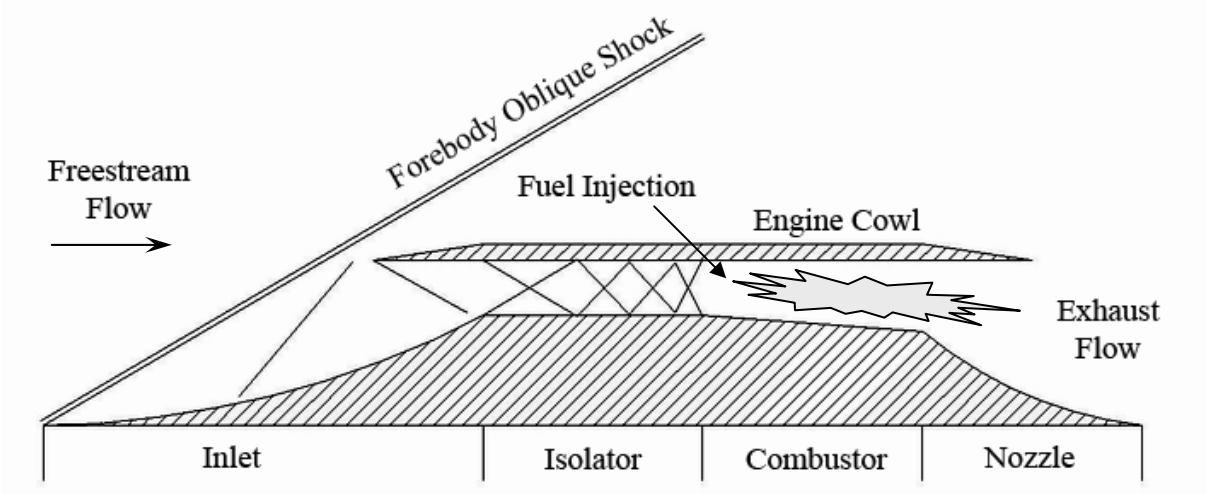

Figure 1.2. Schematic of a scramjet engine.

Ramjet/Scramjet Combustion

A schematic of a dual-mode ramjet/scramjet combustor is presented in Figure 1.3 [Curran, 1996]. The principal features of the dual-mode engine are the isolator and the absence of physical throats. The isolator is a feature that allows control of the flow conditions in station 3 (combustor entry), namely any Mach number and static pressure condition between those of station 2 and those corresponding to a normal shock at station 2 can be achieved.

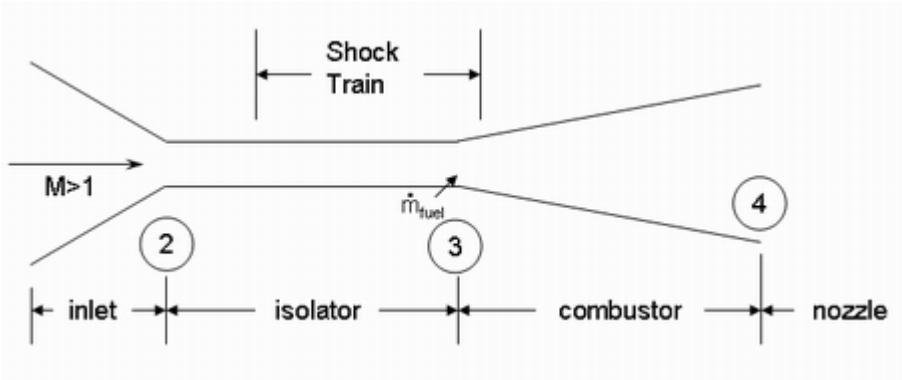

Figure 1.3. Schematic of generic dual-mode scramjet defining engine geometry, adapted from Curran, 1996.

In the scramjet mode, the flow throughout the engine is entirely supersonic. In this mode, the isolator serves the purpose of preventing engine unstart in the event of sudden increase in combustor pressure. This would cause the boundary layer to separate in the presence of an adverse pressure gradient, and the increased pressure would propagate

upstream causing the unstart. However, with the isolator, an oblique shock train with a supersonic core forms to prevent such a possibility.

In the ramjet mode, the flow at some point downstream of the isolator is choked (M = 1) causing a large back pressure at the burner entry. In turn, this causes a normal shock train with a subsonic core to form in the isolator. By operating in the range between the two conditions described above, the isolator is capable of providing any intermediate flow condition, as mentioned earlier. This is done by varying the amount of heat release into the combustor, and specifically by varying the equivalence ratio, φ.

A typical pressure profile for the described engine is shown in Figure 1.4. The pressure in the isolator remains fairly constant until the point where the oblique shock train begins. The pressure subsequently increases because of the heat release from the combustion process and reaches a maximum where it remains constant over some length. At this point the rate of area increase is just sufficient to relieve the thermal blockage resulting from the heat release. Finally, the pressure decreases as a result of either the slower rate of heat release or larger rate of area increase.

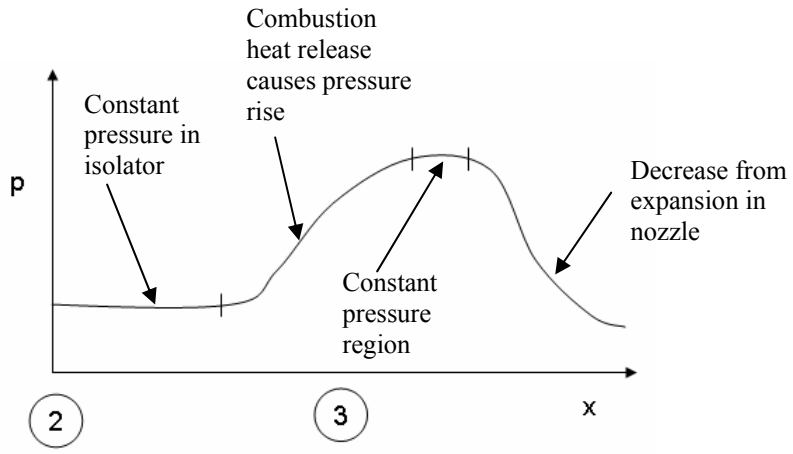

Figure 1.4. Typical axial distribution of wall pressure for scramjet mode operation, adapted from Heiser, 1994.

One parameter of importance is the transitional equivalence ratio, from supersonic to dual-mode combustion. At this value of φ, the combustor is critically at thermal choke conditions; a further increase in heat release will result in a normal shock train forming in the isolator, and the combustion becoming subsonic. In order to obtain an estimate of the pressure ratio required for thermal choke to occur in the current configuration, a Rayleigh flow analysis is performed. The Rayleigh line describes the effect of heat addition into a constant area duct on flow Mach number. Adding heat to a system tends to drive the Mach

number towards unity, namely in the subsonic case the flow is accelerated and in the supersonic case the flow is decelerated. Assuming uniform heat addition into a constant area duct, a calorically perfect gas and neglecting viscosity effects, the pressure ratio is given by [Oosthuizen, 1997]:

$$\frac{p_4}{p_2} = \frac{1+\gamma M_2^2}{1+\gamma M_4^2} \tag{1.1}$$

In a case with $M_2 = 2$ and $M_4 = 1$ (assuming thermal choke), this results in a pressure ratio $p_4/p_2 = 2.75$.

Several countries have lead efforts to develop scramjet powered vehicles. The programs mentioned below are by no means exhaustive, but they simply serve to illustrate the advances in and extent of hypersonic research. In the United States, from 1964 to 1974 the Hypersonic Research Engine was developed, followed by the X-30 National Aerospace Plane (NASP) from 1987 to 1995 and finally the Hyper-X, or X-43, from 1996 to present. An excellent overview of NASA's experimental research regarding supersonic combustion is presented by Rogers et al. [1998]. Research at Arnolds Engineering Development Center is summarized by Rubins and Bauer [1993], whereas Billig [1993] gives an overview of the work performed at the Applied Physics Laboratory of the Johns Hopkins University. Notable programs have been developed in Australia (University of Queensland), Russia (Central Institute of Aviation Motors), Japan (Japan Aerospace Exploration Agency) and France (ONERA – Office National d'Etudes et de Recherches Aerospatiales). Papers presenting the advances of these programs are compiled in the AIAA Progress in Astronautics and Aeronatics book "Scramjet Propulsion" [Curran, 2000].

1.2. Identified Difficulties with Supersonic Combustion

Supersonic combustion might greatly extend the flight-speed envelope of hypersonic vehicles; this does not come, however, without additional difficulties that need to be overcome. There are more stringent mixing and cooling requirements for these types of engines, not present for subsonic combustion engines, and also losses due to shock waves and skin friction are amplified.

To overcome such difficulties, Ferri [1973] proposes that "heat addition is based on generating a flame whose propagation speed is controlled by transport properties such as conduction or diffusion, and not by the rate of chemical reaction", something he called mixing-controlled supersonic combustion. For supersonic flows, high local temperatures are

reached in the combustion regions, so chemical reaction rates are accelerated. Ignition delay times for hydrogen and hydrocarbon fuels can remain the driving force behind engine designs for low hypersonic Mach number operation. Hydrogen is relatively easy to burn and has very low ignition delay time compared with hydrocarbons, but it lacks the energy density required for long-range hypersonic vehicles.

Another difficulty present in supersonic combustion systems is the requirement to anchor the flame. This is traditionally achieved by creating a subsonic region in the flow by means of a physical obstruction, and that comes with the tradeoff of large pressure losses. Such flameholding systems are only required for the low hypersonic Mach number range, between Mach 5 and 8; at higher Mach numbers the local temperatures are large enough to cause fuel auto-ignition.

1.3. Supersonic Mixing Methods

The role of the fuel injector is to spread, as uniformly as possible, the fuel throughout the combustor while minimizing losses occurring during this process. Considering that typical scramjet combustor velocities are on the order of a thousand meters per second, the demands on mixing are more stringent than for a typical subsonic engine. Several configurations have been tested over the years, such as transverse jets, cavities, step injectors, ramps, wedges/struts and pulsed jets. These methods attempt to enhance mixing through various physical means, such as production of vorticity (in ramps) and acoustic excitation (cavities). Most of the aforementioned injector designs are passive, namely the device itself does not produce fluidic phenomena to enhance mixing, but active devices, such as pulsed jets, have also been investigated. Here, a brief overview of the most common injection systems will be give, namely of transverse, cavity and ramp injectors.

1.3.1. Transverse Jet Injection

The simplest scheme for fuel injection is through single transverse jets. Schetz et al. [1990] give a thorough review of experiments involving transverse and wall jets in supersonic flows. Various injector geometries have been investigated, namely circular, elliptical, rectangular and diamond injectors with varying aspect ratios as well as the effect of injection angle. Normal injectors display excellent penetration characteristics; the penetration has been found to grow according to power law curve fits [Gruber, 1995], with the elliptical injectors suffering slightly compared to the circular ones. Numerical studies performed by Foster and Engblom [2003] simulated circular, square, diamond and slot injectors and found that the slot injectors lag in penetration performance. Further, they found that diamonds had

superior penetration characteristics from all injector types investigated, however their simulations were inconclusive regarding mixing characteristics. The high penetration displayed by these injectors is attributed to the lifting effects of the increased streamwise vorticity their geometries generate.

The problem with such injectors is that they introduce large pressure losses to the system. A detached bow shock is formed upstream of the injector. This shock has pressure losses associated with it, the strength depending on the injection angle, but it also causes a subsonic recirculation region upstream of the injector. Another recirculation region exists just downstream of the injector. A schematic of the shocks and separation regions caused by transverse jet injection is shown in Figure 1.5, along with an experimentally obtained schlieren photograph indicating the same regions. Ben-Yakar [1998] proposes the use of these recirculation regions as flame holders, however admits that other injector types would be more suitable for such use. Further, injecting normal to the freestream wastes the momentum of the jet; if it is injected at a smaller angle with respect to the freestream the jet momentum can be added to the thrust, a contribution that can be quite significant.

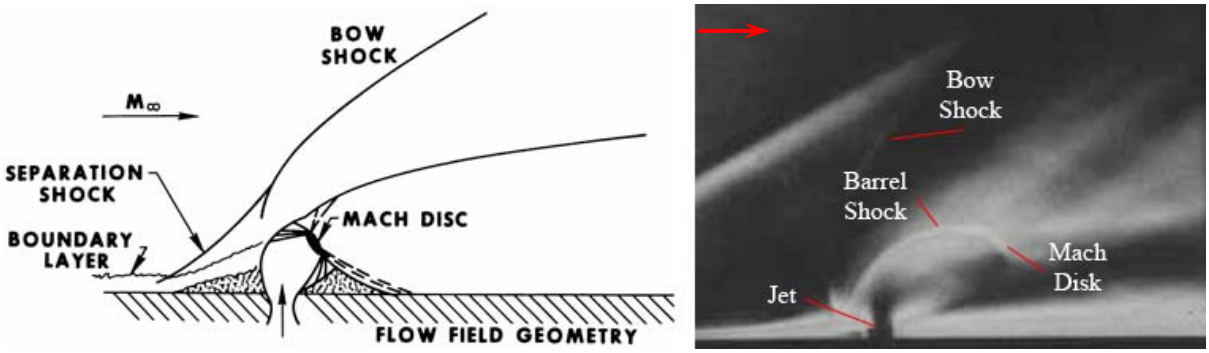

Figure 1.5. Shock structures and separation regions caused by transverse jet injection into a supersonic cross-flow, left is a schematic [United Aircraft Research Laboratories, 1970] and right is a schlieren of a jet in a $M_\infty = 2.4$ crossflow [Schetz, 2005].

If some of the penetration is sacrificed, significant reduction in pressure losses can be achieved by decreasing the injection angle. Mays et al. [1989] report that angled jet injection causes a decrease in near-field mixing; however there is no effect on downstream/far-field mixing. Fuller et al. [1992] extended this work to investigate the effect of injector yaw angle. They found that, even though mixing rates were not increased, the overall plume cross-sectional area increased, increasing the mixing region. Both studies showed that matched pressure jets produced faster mixing compared to under-expanded jets.

Tomioka et.al. [2003] report on mixing and penetration characteristics of diamond injectors at normal and angled injection with respect to the freestream. These authors found that at low dynamic pressure ratios the diamond injector produced larger penetration than a circular injector, and that regardless of the dynamic pressure ratio, mass fraction decay rates were identical. Further, they discovered that the addition of 15-degree yaw to the diamond drastically increased the penetration; but further increase in yaw did not produce additional benefit.

1.3.2. Cavity and Step Injectors

Several scramjet combustor designs implement cavities to enhance performance. Cavities serve two purposes: 1) to create a hot, subsonic, recirculation zone to anchor combustion, and 2) to increase mixing by means of acoustic excitation. Cavity flows can be categorized into two basic flow regimes, depending primarily on the length to depth ratio (L/D). For L/D < 10, the shear layer formed at the separation corner spans the entire length of the cavity and reattaches along the cavity back face. This is called an open cavity. Open cavities have two operational modes, again depending on L/D, based on the dominating oscillation mechanism. Small aspect ratio cavities (L/D < 2-3) are controlled by transverse oscillation mechanism, whereas in larger aspect ratio cavities, longitudinal oscillation becomes the dominant mechanism. When L/D > 10, called a closed cavity, the shear layer is unable to span the cavity length and reattaches to the floor [Gruber, 1999]. Closed cavities display larger drag coefficients, and thus are not favored for scramjet combustor designs. A schematic of cavity types flow character is shown in Figure 1.6 [Gruber, 1999].

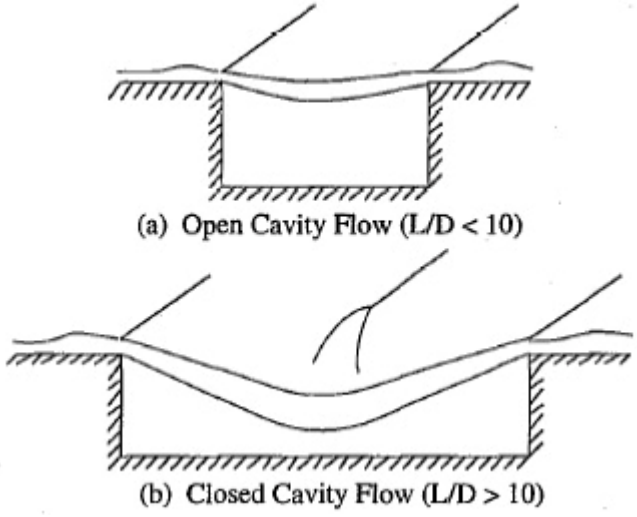

Figure 1.6. Characteristics of cavity flows, adapted from [Gruber, 1999].

Extensive research has been done at the Air Force Research Laboratory (AFRL) investigating a cavity-based fuel injector/flameholder for scramjet applications [Mathur, 1999]. Results prove the success of cavities in scramjets, yielding high combustion efficiencies (near 80% for $\varphi = 0.75$ reported). Other reacting-flow investigations [Davis, 1997 & Yu, 1998] show correlations between cavity length, aft angle and flame intensity, demonstrating the effectiveness of a correctly designed cavity as a flameholder.

Cavities exhibit pressure fluctuations as well as resonances whose frequency, amplitude and harmonics depend on cavity geometry. These oscillations can be used to enhance the fuel-air mixing process. An extensive overview of research on cavities as flameholders and flame stabilizers is given by Ben-Yakar [2001].

The introduction of a large subsonic recirculation region into a supersonic main stream with the aforementioned benefits does not come without a penalty. Cavities have large form drag coefficients, increasing the engine thrust requirements. The primary contributor to the drag problem of the cavities is the high pressure on the downstream cavity wall.

Eliminating the rear wall of the cavity altogether leads to a different type of injector, the rearward facing step. Just downstream of the step, a subsonic recirculation region is created that can be used to anchor the flame, and an ignition device can be placed within this region. Mohieldin and Tiwari [1998] studied the mixing through single and tandem step injectors, shown in Figure 1.7. They found that the tandem configuration displays superior mixing characteristics. Again though, the shock and expansion fan structures formed will lead to large total pressure losses.

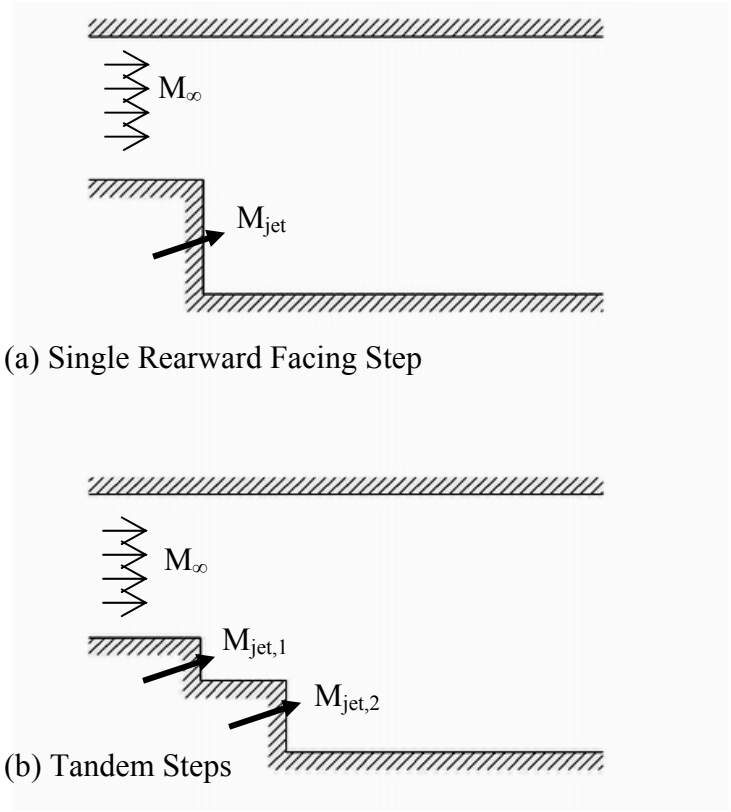

Figure 1.7. Step Injectors with (a) single and (b) tandem configuration.

1.3.3. Ramp Injectors

Ramp injectors are passive mixing devices that work by producing counter-rotating streamwise vortices to enhance fuel-air mixing, and have been extensively studied by many researchers [Davis, 1991, Northam, 1992, Waitz, 1993, Hartfield, 1994, Riggins, 1995, Riggins & Vitt, 1995]. There are two types of ramp injectors, compression and expansion, and each type can have converging or parallel side walls, called swept and unswept. The various ramp geometries are illustrated in Figure 1.8. Supersonic flow over a ramp generates shock and expansion waves that lead to the production of baroclinic torque, essentially the misalignment of the pressure and density gradients at a point, which induces the vortical motions that enhance mixing. The ramp provides vortex shedding off the edges and a local separation region at the base. Fuel is injected through the base into the counter rotating vortex pair, creating a very dynamic mixing environment.

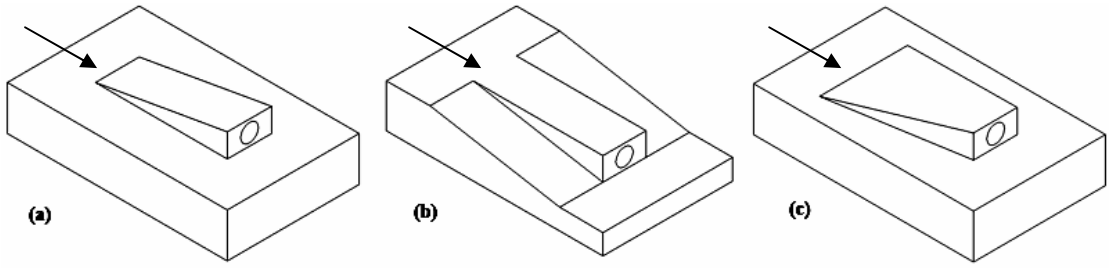

Figure 1.8. Physical ramp injection geometries (a) Unswept compression ramp, (b) Unswept expansion ramp and (c) Swept compression ramp.

Several researchers employed ramp injectors with various geometries in supersonic combustors, with good results. Northam et al. [1992] found higher combustion efficiencies reached with swept ramps (compared with an unswept ramp) and mixing performance similar to that of tangential injection. Stouffer et al. [1993] found that ignition in expansion ramps required a larger length to initiate, but once started, combustion occurred at more rapid rates than with compression ramps, indicating that smaller overall combustor lengths could be achieved.

Ramp injectors have been widely studied for supersonic combustion applications. They have the advantage of good mixing due to the vorticity generation mentioned above and also provide a small subsonic region downstream of the ramp face for anchoring the flame. However, the introduction of an object, such as the ramp, into a supersonic freestream has the disadvantage of the pressure losses and added drag due to its intrusive presence into the freestream. This also creates "hot spots", which increase thermal loads on the system, and may be prohibitive for use with all materials. Further, they depend highly on maintaining their geometry intact, which is challenging in the harsh, high-enthalpy environments existing in scramjet combustors.

1.4. Aerodynamic Ramp Injectors

1.4.1. Aeroramp Development and Past Designs

An aerodynamic ramp injector, or aeroramp, consists of an array of flush wall injectors arranged such as to create vorticity and utilize jet interaction to enhance mixing and penetration characteristics. The aeroramp concept is credited to Schetz [1998], and he provides an interesting discussion of its unique design process. The design is aimed at

reducing the pressure and thermal losses associated with supersonic injection. A schematic of the original aeroramp injector with its dimensions is shown in Figure 1.9.

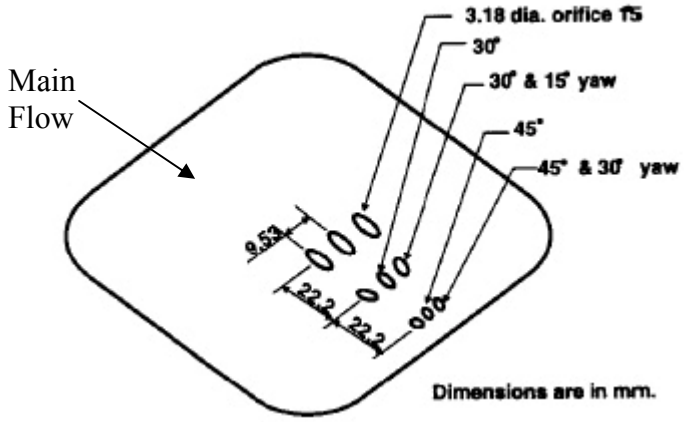

Figure 1.9. The original 9-hole aeroramp [Schetz, 2005].

The first studies of the aeroramp were introduced in a paper by Cox-Stouffer et al. in 1994, where the idea of arranging an array of flush-wall jets in such a way as to induce large vortical structures was experimentally and numerically investigated, in a Mach 3 cross flow. This work proved that the large vortex structures aimed for could be created. The aeroramp was also found to outperform a swept ramp and single angled jets as far as mixing was concerned.

Fuller et al. [1996] investigated the mixing and penetration characteristics of the aeroramp, as well as the losses introduced by the system. They found that increasing the jet-to-freestream momentum flux ratio from 1 to 2 significantly increased the performance of the aeroramp, whereas in a physical ramp arrangement the performance hardly changed. Further, the aeroramp exhibited lower losses than the physical ramp arrangement. In fact, the same authors later published further work comparing the aeroramp and the physical ramp, where they defined a pressure loss parameter to quantitatively measure the associated losses [Fuller, 1998], again demonstrating that the aeroramp had less associated pressure losses.

A series of studies were made to study injector spacing [Cox-Stouffer, 1998], yaw [Cox-Stouffer, 1999] and other design considerations [Cox-Stouffer, 1999]. In these reports the mixing, penetration, and pressure losses are all considered in the overall optimization of the design.

At the same time, simpler aeroramp designs were also being investigated. Jacobsen et al. [1998] investigated a 3-hole aeroramp arrangement and reported on the effect of injector toe-in angle. They found that a moderate toe-in angle (between 15 and 30 degrees) increases

penetration over the 0-degree case, but further increase gives no additional benefit. Jacobsen et al. [1999] also investigated the effect of jet swirl on the mixing. They discovered that the addition of swirl not only increased mixing, but also reduced total pressure losses.

In an effort to further reduce pressure losses of the aeroramp, Jacobsen et al. [2003] propose a 4-hole aeroramp design, and compare it to a single-hole injector in a Mach 2.4 cross-flow. Results showed that the 4-hole aeroramp had slightly higher pressure losses and lower penetration that the single-hole, however much better mixing was demonstrated by the aeroramp.

In other work, Eklund and Gruber [1999] numerically studied the integration of the 9-hole aeroramp with a cavity flameholder and concluded that favorable combustion conditions, based on fuel concentrations, were created. Anderson and Schetz [2005] proposed a simpler 2-hole aeroramp for use with liquid fuels, and investigated the penetration and atomization characteristics of this aeroramp. Maddalena et al. [2005] looked into expanding the operating range of the 4-hole aeroramp by testing it in a Mach 4 cross-flow.

1.4.2. Aeroramp Injector in the Present Study

The 4-hole aeroramp developed by Jacobsen [2003], a schematic of which is shown in Figure 1.10, was used in the present study. A picture of the actual aeroramp is shown in Figure 1.11. The two columns of jets are symmetrical about the injector axis. The upstream jets have a transverse angle (pitch) of 20 degrees with respect to the horizontal (freestream flow direction) and a toe-in angle (yaw) of 15 degrees. The downstream jets have transverse and toe-in angles of 40 and 30 degrees, respectively. The jets are circular; however they have elliptical exit cross-sections due to their angles.

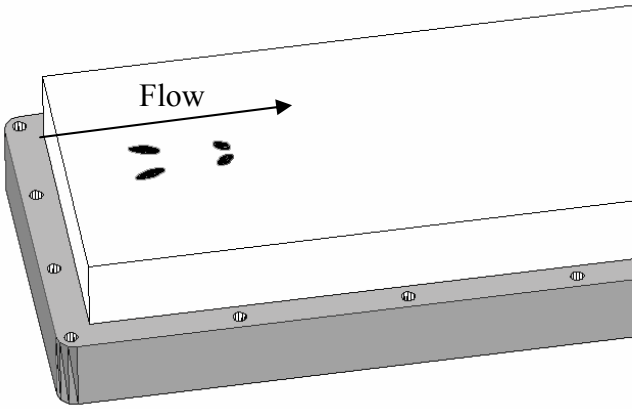

Figure 1.10. Schematic of the aerodynamic ramp injector. Note that the top surface aligns with the combustor wall.

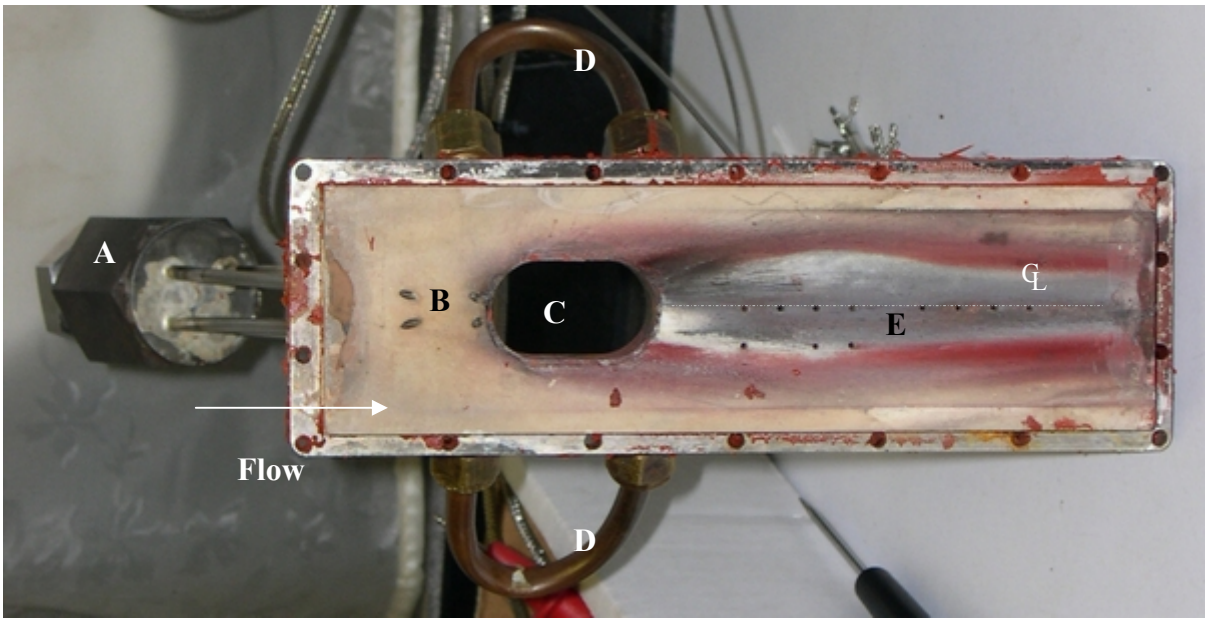

Figure 1.11. The aeroramp-injector insert/plasma-torch-igniter for the present tests. Visible are (A) the fuel feed system, (B) the aeroramp, (C) the plasma torch insert location, (D) the water cooling lines, (E) pressure tap locations. The surface of the insert is coated with zirconia, resulting in the white finish. RTV (high temperature silicone) was used to seal the injector, which is a red compound. The patterns around the pressure tap locations are due to RTV that was spread downstream from the flow.

Each jet had a diameter of 1.6 mm (1/16 inch) resulting in an equivalent diameter of 3.2 mm (1/8 inch). The equivalent diameter corresponds to the diameter a single circular injector would have such that its area is the same as the total area of the aeroramp jets. The equivalent diameter is defined as:

$$d_{eq} = d_j \sqrt{n} \tag{1.2}$$

where n is the number of injector jets (4 here), and d_j is the jet diameter. The equivalent diameter provides a convenient length scale for non-dimensionalizing distances, and it will be used as the reference length scale throughout this dissertation.

More detailed views of the injector, showing the jet angles and spacing are presented in Figure 1.12 and Figure 1.13 respectively.

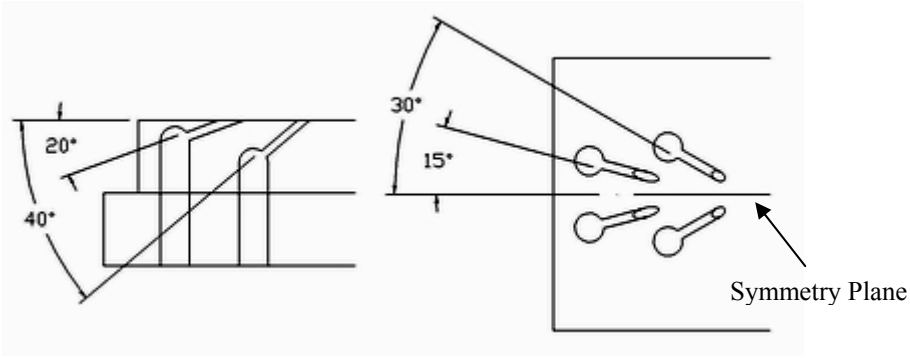

Figure 1.12. Detail showing transverse and toe-in angles of aeroramp injector. Injector symmetry plane is also shown.

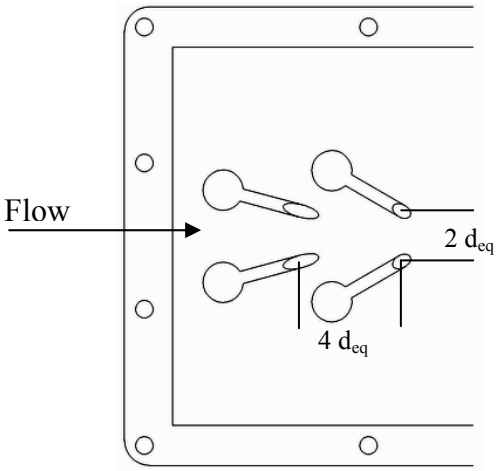

Figure 1.13. Schematic showing the spacing between the injectors of the aeroramp

A useful parameter for characterizing the behavior of a cross-stream injector is the momentum flux ratio, defined as:

$$\overline{q} = \frac{(\rho u^2)_j}{(\rho u^2)_\infty} = \frac{(\gamma p M^2)_j}{(\gamma p M^2)_\infty} \tag{1.3}$$

1.4.3. The Aeroramp Flowfield

The aeroramp, by design, is aimed at enhancing mixing and penetration characteristics compared to conventional injection designs. Its design provides a balance between performance and losses. Increasing the angle of the first injector will lead to larger penetration, but also a stronger shock will be generated, increasing the pressure losses. There are several design aspects contributing to the success of the aeroramp.

The first feature considered is the counter-rotating vortex pair structure generated by the injection into a supersonic cross-flow, similar to the structure observed from single-hole injectors and swept or unswept ramp injectors. The region immediately upstream of the injectors has a higher pressure than the freestream, due to the bow shock in front. Fluid spills from the top and sides of the fuel plume into this area generating vorticity. Vorticity in jets is known to increase mixing, so the benefits of this effect are realized. These vortices also serve in lifting the fuel plume off the wall, leaving little or no secondary fuel core near the surface. A schematic showing the counter-rotating pair of vortices, and the various shock features from a single-hole injector is presented in Figure 1.14.

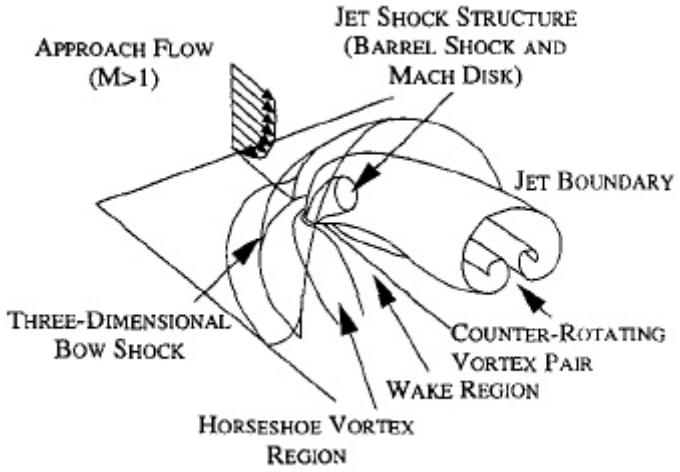

Figure 1.14. Perspective view of the three-dimensional flowfield created by transverse injection. The pair of counter-rotating vortices, as well as other shock structures, can be seen [Gruber, 1995].

As mentioned above, each jet in an aeroramp has a toe-in or yaw angle. The effect of angling jets in this fashion is to increase swirl and generate additional vorticity [Doerner, 1999, Jacobsen, 1999], further enhancing the mixing.

The downstream jets also create a bow shock just upstream of the injectors. The shock interaction with the main fuel plume from the upstream injector set, coupled with the additional injected mass, increases the penetration of the fuel jet. This effect can be seen in the schlieren image of Figure 1.15.

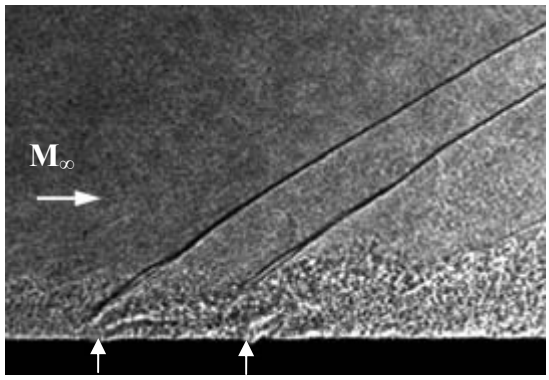

Figure 1.15. Schlieren image showing the bow shocks off the two rows of holes in the aeroramp injector. The jet locations are indicated by the upward pointing arrows. At the second set of jets, the shock interaction along with the additional mass tend to "push up" the plume increasing penetration [Jacobsen, 2001].

By increasing the jet-to-freestream momentum flux ratio, the strength of the shocks is also increased. If the shock becomes strong enough, it might cause additional baroclinic torque, through the breakdown of the vortices, again enhancing mixing. To the supersonic cross-flow, the combined injector jets look like a physical ramp. The schlieren photograph of Figure 1.16 shows the aeroramp in a Mach 2.4 flow. The bow shocks upstream of each injector row can also be seen.

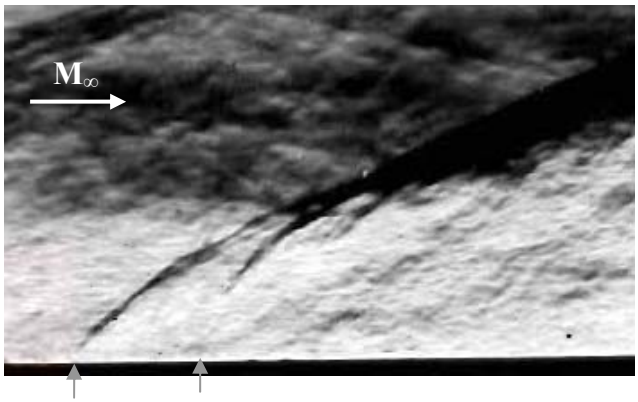

Figure 1.16. Schlieren of the aeroramp operating in a supersonic cross-flow. The jet locations are indicated by the upward pointing jets. To the main flow this looks like a physical ramp.

Subsonic recirculation regions exist in the region between the aeroramp jets. These regions on one hand can increase the losses of the system, but they can be useful as flameholding regions, to anchor the combustion in a scramjet.

1.5. Ignition and Flameholding techniques

Incorporating an ignition and flameholding scheme with the injector is a necessary step for a successful engine in the low hypersonic flight regime. Typically, a region with favorable local conditions for sustaining a flame is desired, such as the subsonic wake past a flow obstruction, to be used as a flameholder. Most of the injector designs described in the previous section include such a region, either by design (cavities, ramps) or by their nature (transverse jets).

At hypersonic flight Mach numbers, fuel ignition is usually not an issue; typical combustor temperatures and pressures are high enough to achieve fuel auto-ignition. However, for the low hypersonic Mach numbers, this is not the case. Therefore, in addition to a flameholding region, an ignition scheme needs to be considered.

The ignition delay time is defined as the time interval between the creation of a combustible mixture and the onset of a flame. For reasonable scramjet fuels, the relative ignition delay times have been found to be methane > JP-10 ≈ heptane > ethylene > hydrogen, i.e., hydrogen has the smallest ignition delay time and methane the largest [Colket, 2001]. Ignition delay times depend on temperature and pressure, but are typically (order of magnitude) 0.01 ms for hydrogen, 0.1 ms for ethylene and 1 ms for methane. In the high combustor velocities encountered in scramjets (order 10^3 m/sec), significant combustor lengths are thus required for ignition to occur. This dictates the need for a mechanism to accelerate ignition.

1.5.1. Ignition through Pyrophoric Mixtures

A common practice in experimental research on supersonic combustion is the addition of a pyrophoric substance to the fuel to reduce effective ignition delay times and achieve combustion. Such substances were employed by Billig in 1959 when he conducted the first experiment to produce net thrust from combustion in a supersonic stream [Gilreath, 1990]. Aluminum alkyls, namely triethylaluminum and trimethylaluminum, have been found to significantly reduce ignition delay and total reaction time for JP-10 [Ryan, 1995]. Most of the hypergolic substances tend to be toxic, and hence have associated environmental issues. A lot of emphasis is being placed on developing non-toxic propellant additives that perform similarly to their toxic counterparts [Funk, 1999]. Such a substance is silane, SiH_4. Northam et al. [1986] report on the effect of silane concentration in methane, for supersonic combustion applications. They found that a 20% silane/methane mixture autoignited at

temperatures where the pure methane would not. Further, combustion efficiencies around 70% were achieved.

Other hypergolic substances, such as fluorine, have also been used. Diskin and Northam [1986] developed an igniter pilot for scramjets, designed to yield fluorine atoms when pre-burned with a mixture of hydrocarbons.

Aside from the environmental issues associated with the hypergolic substances, use of such fuel additives is disadvantageous from a systems point of view as well. Their pyrophoric nature necessitates extra safety precautions, which come with a weight penalty to the vehicle, reducing payload weight.

1.5.2. Ignition through use of Electrical Discharges

A plasma torch is a device in which a flowing gas is passed through an electric arc, producing plasma. Plasma contains a mixture of ions, electrons and neutral particles. A commonly used definition for plasma is any gas over 3000 K. Plasmas are abundant with excited species and are useful in a wide range of applications, such as flame stabilization, lean burning in internal combustion engines and exhaust emission control. Plasma torches vary widely in design, but they are all primarily based on the production of an electric arc to dissociate a feedstock gas.

The use of electrical discharges to promote and stabilize flames has been suggested as early as 1924 by Southgate [Harrison, 1971], and, since then, has been extensively investigated [Chen, 1965, Warris, 1985, Weinberg, 1983]. More specifically, for scramjet applications, Northam et al. [1984] showed that a plasma torch operating at a net power of 2 kW is a good alternative to pyrophoric additives and can stabilize a flame when injection occurs either upstream or downstream of the torch. “The effectiveness of the plasma torch is thought to be related to the ability of hydrogen atoms to reduce ignition delay time of a hydrogen-air mixture. […] Calculations indicate that 0.1% hydrogen atoms are as effective as 20% silane in reducing ignition delay times [Wagner, 1989]”.

Analytical investigations of ignition delay times and burning velocities were conducted and found that the burning velocity increased proportional to the radical concentration and ignition delays decreased with increasing radical concentration [Takita, 1999]. The relative location of the plasma torch with respect to the injectors has also been investigated, finding higher combustion efficiency when placing the torch downstream of the fuel injector [Minato, 2003].

1.6. The VT Plasma Torch Igniter – Current Design

Virginia Tech has a long history of developing plasma torches, since the early 1980's. The current torch design draws many features from the "3rd generation VT torch", or the VTPT-3 of Gallimore [Gallimore, 2001]. This can be traced back to the original plasma torch used by Barbi [Barbi, 1986] and Wagner [Wagner 1989] and improved by Stouffer [Stouffer, 1989]. The current torch design is adapted from the VTPT-3 to utilize commercial components and take advantage of torch developments from industry. These design advancements were made by Dr. Jacobsen [Jacobsen, 2004], who needs to be thanked for his contributions to the torch design.

A schematic of the current plasma torch igniter design can be seen in Figure 1.17. The feedstock enters the torch axially through a supply tube that terminates at the cathode. The cathode is threaded, to screw into this supply tube. The negative potential is applied to the feedstock supply tube. An insulating sleeve is needed to isolate the cathode from the anode, since the anode must be at a higher potential in order for an arc to be established. Finally the anode is placed around the cathode. The anode has a sonic orifice through which the feedstock gas exhausts. The total length of the torch is approximately 20 cm.

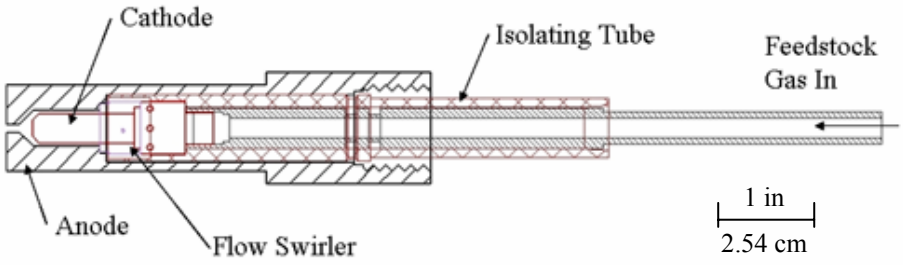

Figure 1.17. Schematic of the VT Plasma Torch Igniter.

The plasma torch follows the flush-wall design mentality of the aeroramp injector. It also has no protrusions into the freestream and is aimed at minimizing total pressure losses.

1.6.1. The Anode and the Cathode

The torch anode (shown in Figure 1.17) is designed to provide an exhaust orifice for the plasma produced by the arc. A choked orifice is employed in this torch, which is ensured by maintaining a high pressure in the feedstock line. As long as the pressure ratio between the feedstock (P_{feed}) and the exhaust ambient conditions (P_e) satisfy

$$P_{feed} / P_e \geq 1.893 \tag{1.4}$$

the orifice will be choked [Anderson, 2003].

The internal geometry of the anode consists of a constant area cylinder with a diameter of 7.24 mm (this region surrounds the cathode), which terminates in a cone with a 90 degree apex angle followed by a constant area cylindrical orifice with a 1.6 mm diameter and 2.5 mm long (see Figure 1.18). This design, along with the choked flow, ensures that the arc will attach on the external surface of the anode instead of the inside walls.

Plasma torches can operate in two modes, the high and low-voltage modes [Stouffer, 1989, Perbola, 1998]. "The high-voltage precludes the need for high current densities to achieve the necessary Joule heating and plasma generation. In this mode the lower current densities give rise to a diffuse as opposed to a constricted arc attachment at the anode, thereby minimizing anode erosion" [Loh, 1992]. It is important for the arc to attach on the external surface of the anode, because this ensures high-voltage mode operation. Also, for the present application, we want the excited species in the arc out in the combustible mixture of the combustor flow. "Evidence strongly suggests that once the arcjet jumps from low voltage to high voltage operation, the arc attachment point moves from the vicinity of the cathode tip, through the constrictor region, to into the nozzle expansion region. Observations made by viewing directly into the arcjet nozzle confirm the outside arc attachment when operating in the high voltage mode" [Grimes, 1991]. The arcjet attachment modes are shown in Figure 1.18.

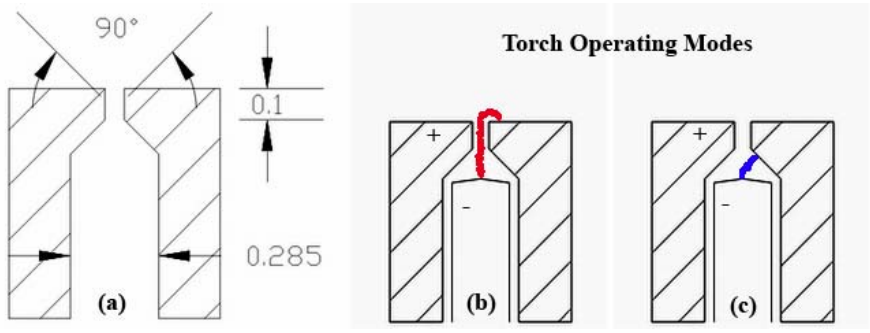

Figure 1.18. (a) Detail showing anode internal geometry and dimensions (in inches). (b) High-voltage mode – this is the desired operating mode for the torch. (c) Low-voltage mode.

The cathode used here was a commercial component, made by Thermal Dynamics®, the TD-8-7502, illustrated in Figure 1.19. The cathode has a threaded base to screw directly onto the feedstock line. The feedstock is turned and exits radially through eight holes in the cathode base. The body is copper; however it has a hafnium tip, which is where the arc attaches.

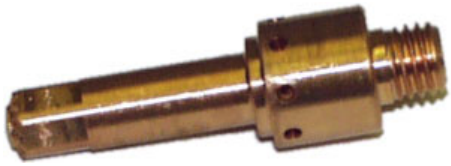

Figure 1.19. The Thermal-Dynamics TD-8-7502 cathode.

1.6.2. The Flow Swirler

A flow swirler is a device that imparts angular velocity to the feedstock gas. When the feedstock is accelerated to sonic conditions through the exhaust orifice, this angular velocity will be conserved. An electric arc established between the cathode and anode will tend to attach to the same location of the anode, but the swirl in the feedstock gas "drags" the arc along causing it to rotate on the anode face. Having sufficient swirl in the feedstock gas is very important to ensure long operating life cycles for the torch.

Two commercial flow swirlers were available for use with the selected cathode, the TD 8-7508 and the TD 8-7501. These are shown in Figure 1.20. Each has a set of angled holes drilled into the side of the swirler body through which the feedstock passes. The TD 8-7508 has three holes and the TD 8-7501 has six holes. A TD 8-7508 was modified by doubling the diameter of the holes. So, in effect, three swirlers were available for use with the torch.

Figure 1.20. The TD 8-7501 (left) has 6 holes and the 8-7508 (right) has 3 holes.

A correlation exists between the amount of swirl in a jet and the angle the jet plume produces [Schetz, 1980]. Specifically, the wider the angle, the more swirl exists in the flow. The three swirler designs described above were tested to find the most suitable design for the current configuration. Feedstock was passed through the torch with each swirler and exhausted into a quiescent test cell. A shadowgraph of the exhaust was taken, and the angles were measured to determine the most suitable swirler. These shadowgraphs are shown in Figure 1.21.

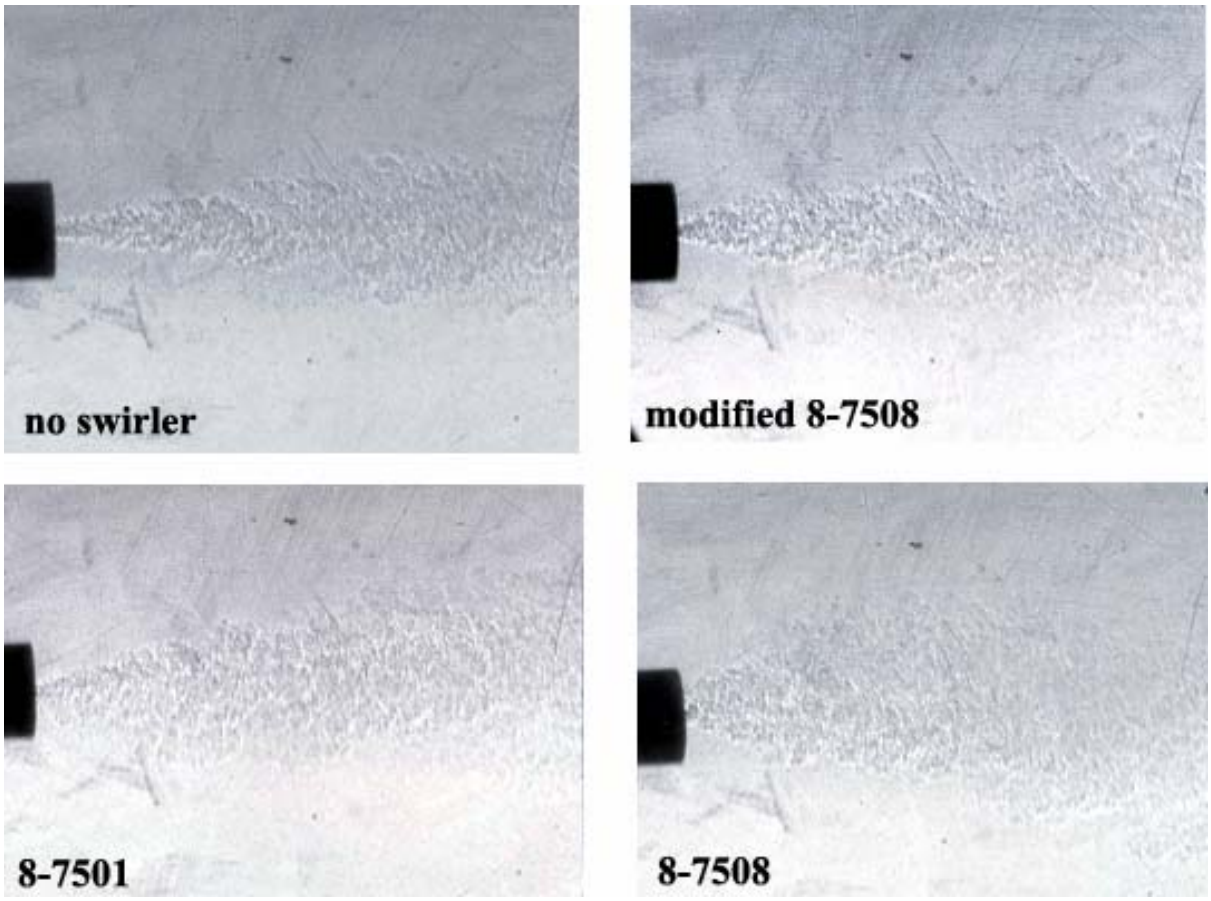

Figure 1.21. Shadowgraphs of torch exhaust plume (feedstock only) with different swirler configurations

Table 1-1 shows the plume angle produced for each swirler tested. The unmodified TD 8-7508 produced the widest plume angle and was used in the present supersonic combustion experiments.

Swirler type	Exhaust Angle
no swirler	20-degrees
modified 8-7508	30-degrees
TD 8-7501	40-degrees
TD 8-7508	50-degrees

Table 1-1. Exhaust angles for different swirler types

1.6.3. Materials Considerations

Past studies have proven copper to be an ideal material for the anode when a nitrogen or air feedstock is used with the torch. Copper is eroded at a much lesser extent with these feedstock gases than other materials, such as molybdenum or tungsten [Gallimore, 2001].

Materials for the cathode were dictated by the cathode selection, since a commercial component was used. The cathode body is made of copper, but it has a hafnium tip, which is where the arc strikes.

The feedstock supply tube was stainless steel, to ensure good electric conductivity, since the negative potential required to operate the torch was applied to this tube.

The isolator sleeve and flow swirler were made of DuPont's Vespel® SP-1. This material provides high electrical and thermal insulation [DuPont, 2005], ideal for the environments in the plasma torch.

1.6.4. Anode and Cathode Erosion

As the plasma torch operates, the anode and cathode get eroded at the point where the arc is attached. When the electrodes are eroded, the anode-cathode gap is typically decreased and the operating voltage is increased. This causes the power to drift slightly through the duration of the pressure scan. If erosion is severe enough, torch operation is disrupted. Figure 1.22 shows eroded anode and cathodes compared to new ones.

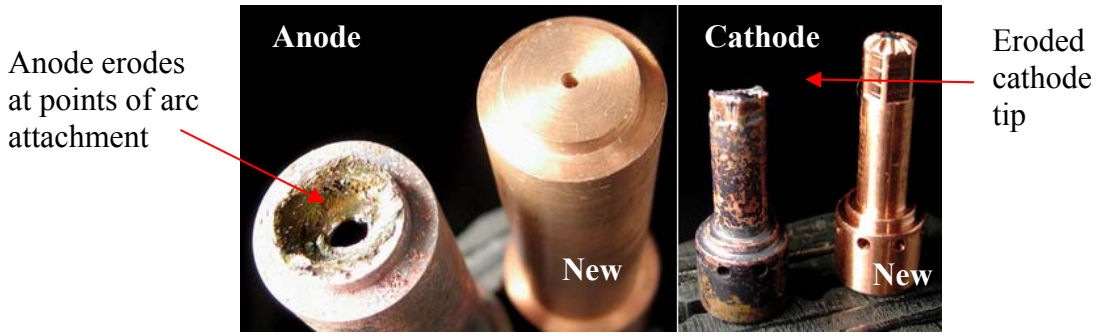

Figure 1.22. Erosion in the anode (left) and cathode (right), compared to new electrodes. On the left, the uniform erosion of the anode about the orifice indicates that the arc is swirling and not attaching only to one side of the anode, despite the supersonic crossflow.

1.6.5. Improvements on VTPT-3

There are two major improvements over the base design of the VTPT-3 torch. First of all, the anode-cathode distance is fixed. In the previous design, the cathode was connected to a micrometer drive, allowing for variable spacing between the two electrodes. The final distance was empirically determined and had to be reset prior to each torch run. Due to small asymmetries arising from machining errors or the torch assembly process, the cathode was not perfectly centered about the anode and this could result in the torch operating in the low-voltage mode. In the current design, the distance is fixed, avoiding this problem and ensuring high-voltage mode operation.

The second improvement is the adaptation of the torch to be able to use commercial components, namely the cathode and the flow-swirler. This significantly reduces cost and part-reproduction times, since they can be purchased at local welding-supply stores. Also, this takes advantage of the technology and development efforts of the designers of the commercial components, which lead to increased operating times for the overall configuration.

1.7. Aeroramp – Torch Integration

Both the aeroramp and the plasma torch serve the specific task for which they were designed, i.e., an injector with applications in supersonic flow and a fuel igniter. However, the goal of this study is to have them function as an integrated injector/igniter system for a supersonic combustion ramjet.

The early efforts of using the Virginia Tech plasma torch as a scramjet igniter and flameholder were led by Wagner [1989, Northam, 1984]. In these experiments, the plasma torch was placed in the recirculation region of a rearward facing step, with upstream pilot fuel injectors and main fuel injectors downstream of the torch. The rationale behind this was to reduce the required ignition energy by increasing residence time and temperature (downstream of the step) and use the pilot mixture to ignite the primary fuel.

Murakami et al. [2003] conducted plasma ignited scramjet combustion experiments and investigated the location of the plasma torch with respect to the injector, testing locations both upstream and downstream of the fuel injector. They found that placing the plasma torch downstream of the fuel injector results in more rapid combustion for all fuels tested (hydrogen, ethylene and methane).

From these two different approaches to the implementation of the plasma torch igniter concept, it becomes apparent that no clear guideline for injector/igniter integration exists.

Studies have been performed at Virginia Tech's cold-flow, blow-down type Mach 2.4 supersonic facility to evaluate different locations of the plasma torch with respect to the aeroramp injector [Jacobsen, 2001, Gallimore, 2001]. Aerothermodynamic probing and surface oil-flow visualization were employed to determine an ideal region to place the plasma torch. An oil-flow visualization image from this study is presented in Figure 1.23.

In these studies, the flush-wall design mentality aimed at minimizing pressure losses was followed. Thus, no steps in the wall could be employed for placing the plasma torch. Also, using a pilot injector would also incur further losses. The focus was on determining an ideal location for the torch downstream of the fuel injector.

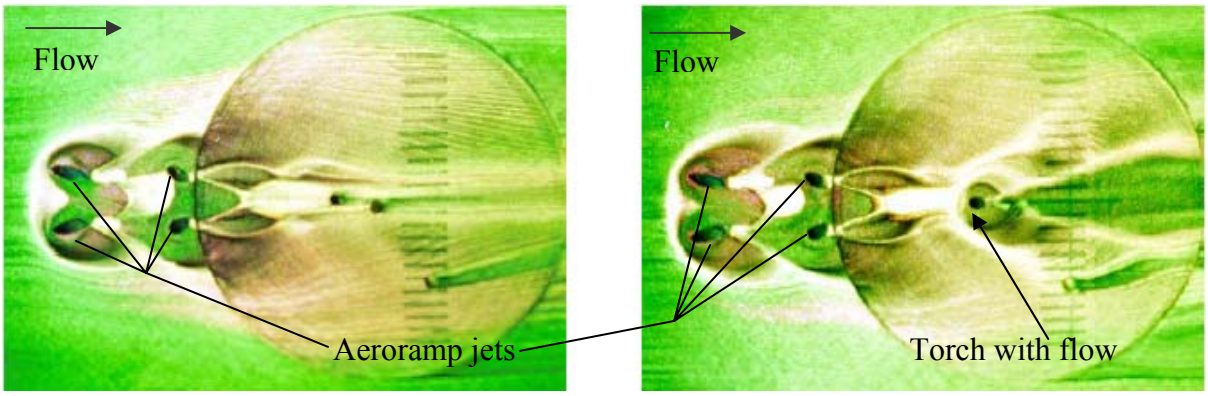

Figure 1.23. Surface oil-flow visualization of the aeroramp flow alone (left, $\overline{q}$ = 3.0, $\overline{q}_{Torch}$ = 0) and the aeroramp with the torch (right, $\overline{q}$ = 3.0, $\overline{q}_{Torch}$ = 2.7) [Jacobsen, 2001]. The regions of oil accumulation indicate recirculation zones, and the shape of the leading bow shock can also be discerned.

The conclusions of these studies were to settle on three potential torch stations, at x/deq = 6, 8 and 10, as measured from the center of the aeroramp injector. A schematic illustrating these locations is given in Figure 1.24. These locations were considered to be a good starting point for the current configuration and so were not modified. The current design was based on these studies, so provisions for placing the torch in the aforementioned locations were made.

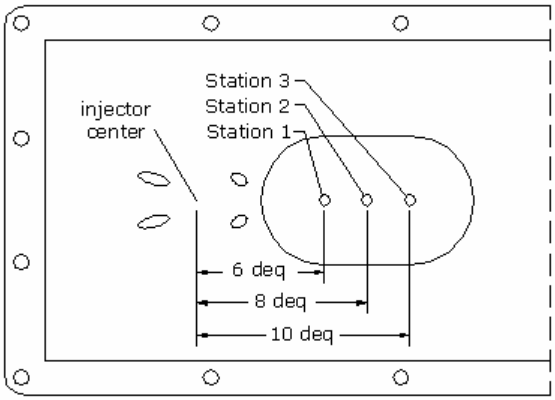

Figure 1.24. Available stations (1,2 or 3) for placement of the plasma torch at x/d_{eq} = 6, 8 and 10.

1.8. Research Goals

The goals of this research are:

- Prove that the integrated aeroramp-injector/plasma-torch-igniter can be used as a combustor system for scramjets.

- Establish operability range limits of the configuration in a heated Mach 2 cross-flow, with varying:
    - Fuels; hydrogen, methane and ethylene are tested
    - Total-temperature; the tunnel total temperature is varied between 500 and 1000 K corresponding to flight Mach numbers of 2.5 to 4.5.
- Prove the robustness of the plasma torch as an igniter/flameholder for supersonic combustion applications over conventional systems, such as silane.
- Use the Ramjet Performance Analysis (RJPA) code to extract performance characteristics of the configuration.
- Use Computational Fluid Dynamics (CFD) to:
    - Further understand the mixing process of the aeroramp and analyze the resulting flow field.
    - Determine the suitability of the available locations for the plasma torch.

1.9. Fuel Selection

Three fuels were tested, namely hydrogen (H_2), methane (CH_4) and ethylene (C_2H_4). Hydrogen was selected due to high reactivity and wide use in supersonic combustion experiments and scramjet test vehicles (NASA's X-43A and Australia's HyShot). It provides an excellent experimental base, to establish performance parameters for the injector/igniter configuration, and allows for direct comparison with other combustor configurations existing in the literature.

Hydrocarbon fuels are also of interest due to their higher density compared to hydrogen and thus lower storage volume requirements for a given mission range. Hydrocarbon fuels can be considered for experimental vehicles, such as NASA's X-43C and DARPA's Falcon.

1.10. Test Matrix

1.10.1. Fueling Conditions

A baseline case for each fuel is established at the tunnel total temperature conditions of T_o = 1000 K. Beginning from the leanest condition where a measurable pressure rise can be detected, the equivalence ratio will be increased until (a) a pressure rise near the normal-shock pressure rise is obtained or (b) a facility limit, based on heat release, is reached. For

Mach 2 flow, the normal-shock pressure rise is 4.5. The heat release limit is a safety limit imposed by the design materials of the facility.

1.10.2. Total temperature variation

In an attempt to simulate off-design flight conditions, the total temperature of the tunnel is varied. The facility has an operational limit between 530 and 1050 K. The lower limit is imposed by the mass flow rate that can be supplied through a valve in the air supply system, because a constant total pressure is maintained. The higher limit is imposed by the heating ability of the electrical heaters.

For each fuel, a baseline case is established at the highest tunnel total temperature. The temperature is then incrementally decreased, and attempts at combustion are made.

C h a p t e r 2

2. Experimental Setup

2.1. The Supersonic Combustion Facility

Experiments were conducted in the University of Virginia Supersonic Combustion Facility (SCF) at the Aerospace Research Laboratory of the University of Virginia. The primary reason this facility was selected for use is that it is a heated flow facility, allowing for simulation of conditions that exist at a physical point in the atmosphere. This is opposed to conditions in unheated, blow-down type facilities, where the total temperatures (and hence enthalpies) are extremely low, so a realistic for flight atmospheric point does not correspond to the test conditions. Also, since combustion applications are being considered, a high temperature facility aids the combustion process.

The overall configuration of the SCF consists of an oil-free, two-stage compressor, desiccant air dryers, ballast, and air storage tanks, a 14-stage electrical resistance heater, ceramic flow straightener, supersonic nozzle, constant area isolator, test combustor and exhaust tube. The facility is capable of continuous operation and provids a flow total temperature near 1200K [Goyne, 2001]. The electrical heater provides a hot test gas free of contaminants due to vitiation, such as water, NO, particles and other radical species [Krauss, 1992, Krauss, 1988]. At Mach 2, the test section static pressure is near 41 kPa with a total pressure of 330 kPa. Table 2-1 presents the average test conditions in the SCF and Table 2-2 gives typical tunnel lengths.

Average Test Conditions		
Total Pressure	[kPa]	330
Total Temperature	[K]	1050
Mach Number	--	2
Static Pressure	[kPa]	42
Static Temperature	[K]	610
Velocity	[m/s]	1000

Table 2-1. Average test conditions in the SCF. These conditions correspond to a scramjet flying at M = 4.5 at an altitude of 90,000 feet.

Description	Location (d_{eq})
Facility Nozzle Throat	-112
Facility Nozzle Exit	-96
Isolator Exit	-16.8
Aeroramp Injector	0
Plasma Igniter	8
2.9 deg Divergence	18.8
Exit to atmosphere	114.4

Table 2-2. Typical SCF dimensions.

The combustor flow-path consists of a two-dimensional Mach 2 nozzle, followed by a constant-area, rectangular isolator, a rectangular combustion duct and an exhaust nozzle. One of the combustor walls has a 2.9-degree divergence to relieve thermal blockage and avoid choking. The tunnel exhausts to atmospheric conditions. A schematic of the SCF along with detailed views of the test section and combustor are presented in Figure 2.1 (a) and (b). The arrangement of the integrated aeroramp-injector/plasma-torch igniter is detailed in Figure 2.1 (c). The coordinate system used is also defined in this figure. The center of the axis is located at the center of the aerodynamic ramp injector, and the x-axis is aligned with the flow. The z-axis is perpendicular the injection wall and positive in the direction of positive penetration. The y-axis is defined, since a right-handed coordinate system is used.

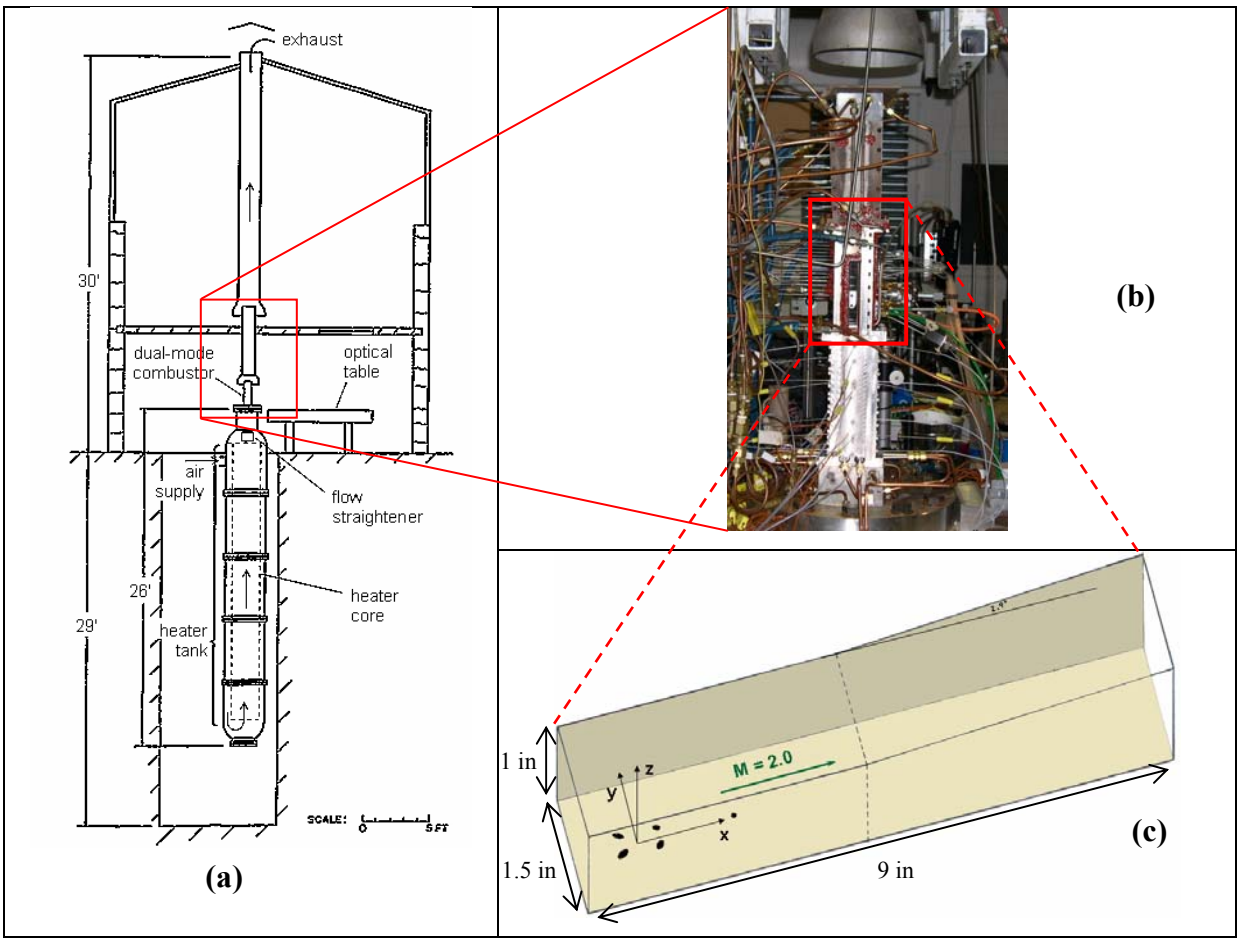

Figure 2.1. (a) UVA's SCF overall geometry [ARL, 2004] with details showing (b) the isolator, combustor and exhaust and (c) the constant area combustor section followed by the diverging nozzle.

The combustor walls and injector wall insert are zirconia coated from x/deq = -16 to 52. Optical access to the test section is facilitated through fused silica windows on the two side walls of the tunnel. The window support frames, injector plate, Mach 2 nozzle and portions of the combustor duct are water cooled.

2.2. Fuel Feed System

Fuel is stored in two fuel barns located, for safety reasons, outside the building. Each farm consists of a manifold capable of holding up to twelve fuel cylinders. This setup ensures that the required fuel mass flow rates are achieved even when the individual cylinder supply pressure is low. Fuel is transferred to the injector through a considerable length of un-insulated tubing. This fact ensures that the fuel total temperature at the injection point is equal to atmospheric temperature. A picture of the fuel farm is shown in Figure 2.2.

Figure 2.2. UVa fuel farm. Visible is the manifold which can hold up to twelve cylinders of fuel.

The fuel mass flow rate is measured using a Hastings ^{TM} model HFM-200 mass flow meter, capable of measuring mass flow rates within ±1% of full scale. A valve in the control room was manually adjusted to achieve the desired fuel mass flow rate. The tunnel room is equipped with sensors, to alert researchers in case of a fuel leak.

2.3. Plasma Torch Power Supply and Setup

Power for the plasma torch operation was provided through the Thermal Dynamics® Pak-Master 100XL Plus welding power supply. It supplies an open circuit voltage of 250 Volts and current between 15 and 80 Amperes. A Miller Electric HF-251-D-1 high-frequency electrical starter is placed in series with the power supplies electrodes and provided a short duration high-frequency burst of current to the torch to initiate the electric arc. The high-frequency starter was typically operated for 0.25 seconds. The power supply and high-frequency starter are shown in Figure 2.3.

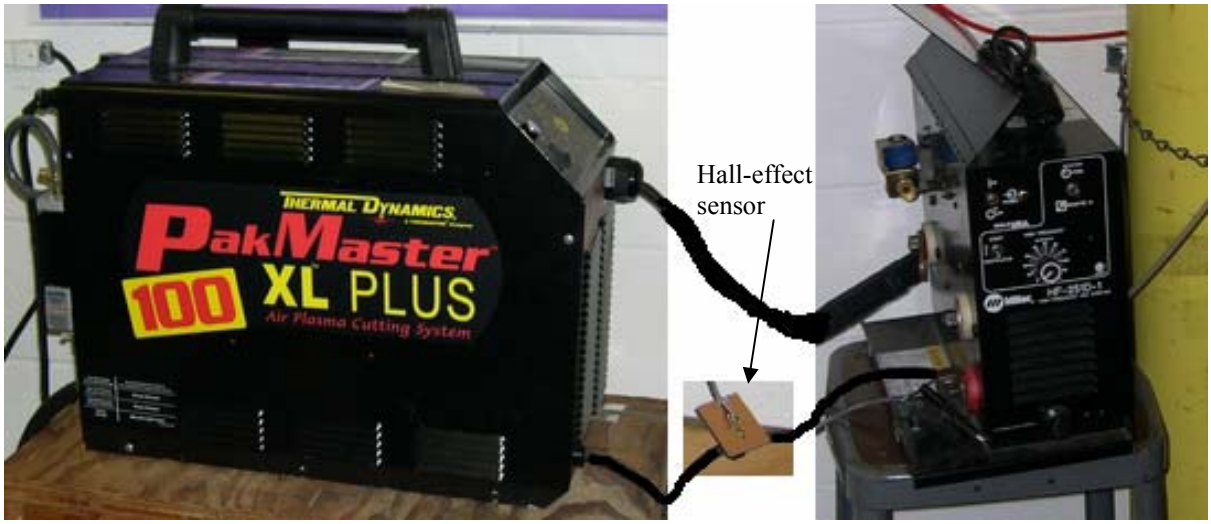

Figure 2.3. The PakMaster 100XL Plus welding power supply (left) and the Miller Electric High-Frequency starter (right). In the center, the hall effect sensor is shown, used to measure the current being sent to the torch.

Feedstock gas was supplied through a high pressure gas cylinder connected to the torch through a Sierra S40™ flow controller and Sierra 902C Digital Dual Channel Readout. The gas cylinder regulator was set to 400 kPa (60 psi) to ensure that the torch remained choked. The flow controller was calibrated for methane and was capable of regulating the feedstock volumetric flow rate between 0 and 30 standard liters per minute (slpm). A conversion factor, the k-factor, is needed to determine the volumetric flow rate of other gases, and was determined based on the gas density and specific heat at constant pressure. It was calculated using the following formula:

$$\frac{K_{feed}}{K_{CH_4}} = \frac{(N/\rho C_p)_{feed}}{(N/\rho C_p)_{CH_4}} \tag{2.1}$$

where ρ is the density, C_p is the specific heat at constant pressure and N is a constant based on the number of atoms of the feedstock gas molecule [Sierra Instruments, 1994]. The values for N are given in Table 2-3. Since methane is the calibration gas, K_{CH4} is equal to unity. For the other feedstock gases used, air and nitrogen, the k-factor is 1.39. Therefore, the flow meter is capable of regulating the volumetric flow between 0 and 42 slpm.

Number of atoms in gas molecule	N
Monoatomic	1.040
Diatomic	1.000
Triatomic	0.941
Polyatomic	0.880

Table 2-3. Values for the constant N to determine the flow meter k-factor

The operating voltage of the plasma torch is fixed and determined by the gap between the anode and cathode. The voltage drifted slightly (±10 Volts or ±8% operating value) with torch operation, as the electrode erosion changed this spacing (as discussed in section 1.6.4), but was on average 120 Volts. Current to the torch was a controllable variable. The power supply is capable of providing 15-80 Amperes, but typical operating ranges were 25-70 Amps. Torch power, $\mathcal{P}$, is determined based on the simple relationship:

$$\mathcal{P} = I \cdot V \tag{2.2}$$

where I and V are the operating plasma torch current and voltage respectively. Power levels vary based on fuel, but typically range between 3 and 7 kW.

2.4. Data Acquisition

2.4.1. Facility Pressures and Temperatures

Several thermocouples and pressure transducers exist throughout the facility to check operating temperatures and pressures. These values are relayed to the control room and displayed on a 286 computer for monitoring purposes. Data acquisition and analog to digital conversion is handled by a Fluke 2280A Data Logger System. Uncertainties in temperature are reported by the manufacturer to be ±2% [Omega, 2001] and for pressures is ±3% [Goyne, 2004-5].

2.4.2. Plasma Torch

The voltage output of the welding power supply is read through Analog Devices AD210 isolator amplifiers, shown in Figure 2.4. Analog Devices [2005] reports a maximum ±2% error for these devices, and so the voltage is known within ±2.5 Volts. A Honeywell® CSLA2DJ Hall-effect sensor, shown in Figure 2.3, is used to measure the operating current levels within ±1% (from calibration). The outputs of these devices are connected to digital multi-meters for visual reference and are read during each run through a LabView code, whenever a power measurement is needed. This code measured the voltage and current levels over a short period (about four seconds) and reported average and RMS power. Based on the uncertainty for the current and voltage levels, the accuracy of the power measurements is ±0.25 kW, or ±4% full scale.

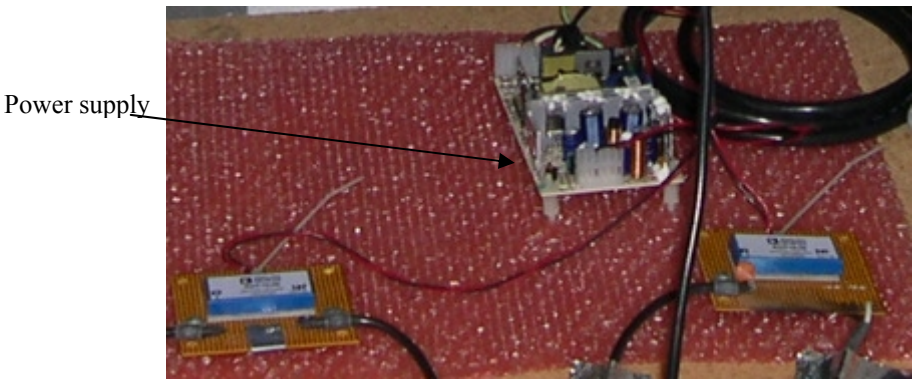

Figure 2.4. Isolation amplifiers used to measure welding power supply voltage.

2.4.3. Wall Static Pressures

Thirty-two pressure ports exist in the isolator and combustor sections of the SCF, on the wall opposite the injection wall. The pressure-tap diameter is 1 mm, and expands to 1.6 mm at 1.3 mm beneath the surface. Tap locations are given in Table 2-4.

Two systems for pressure data acquisition were used. Hydrogen and methane data were obtained using a Scanivalve system, and ethylene data was obtained using a NetScanner system. Both systems are equipped with purging gas (air for the Scanivalve and nitrogen for the NetScanner) to clear the pressure-tap tubing from accumulated water vapor and other combustion products.

Name	x/d_{eq}	Name	x/d_{eq}	Name	x/d_{eq}	Name	x/d_{eq}
isolator-1	-90.75	comb-5	15.39	comb-13	33.03	comb-21	66.47
isolator-2	-70.77	comb-6	17.63	comb-14	35.23	comb-22	70.47
isolator-3	-46.77	comb-7	19.83	comb-15	37.43	comb-23	74.47
isolator-4	-22.71	comb-8	22.03	comb-16	39.63	comb-24	78.47
comb-1	-15.33	comb-9	24.23	comb-17	41.83	comb-25	86.47
comb-2	6.63	comb-10	26.43	comb-18	44.03	comb-26	94.47
comb-3	6.63	comb-11	28.63	comb-19	56.47	comb-27	102.47
comb-4	13.23	comb-12	30.83	comb-20	62.47	comb-28	110.47

Table 2-4. Names and locations of the pressure taps in the isolator and combustor sections.

2.4.3.1. The Scanivalve System

Hydrogen and methane pressure data were measured through a Setra™ pressure transducer and a scanning Scanivalve®. The scanner operated at an interrogation frequency of approximately 0.5 Hz and sequentially measured all ports. A complete purge and scan cycle took approximately 150 seconds to complete. Experimental uncertainties of pressure measurements were estimated to be ±2% [Goyne, 2001].

2.4.3.2. The NetScanner System

A Pressure-Systems NetScanner model 98RK Rackmount Intelligent Pressure Scanner [Pressure Systems, 2000], was used for the ethylene tests. This system had two racks (9816 module) each with sixteen piezo-resistive transducers. The NetScanner was capable of simultaneously interrogating all pressure taps of each module at frequencies up to 100 Hz. It communicated via Ethernet with a PC on which the data acquisition software, provided by Pressure Systems, was operating.

The software was set to an interrogation frequency of 20 Hz and data for each equivalence ratio was acquired over a 5 seconds period. Analysis of the time dependent measurements yields minute variations in pressure (less than 3%), indicating that the combustion process is fairly steady. Any higher frequency variations that might exist are averaged out over the interrogation period and the length of the tubing.

The manufacturers report a ±0.05% full scale accuracy on pressure measurements, achieved through digital temperature compensation and by having integrated calibration curves in the hardware circuitry [Pressure Systems, 2000].

2.4.4. Wall Temperatures

Type-K thermocouples are placed throughout the test section of the facility to monitor and measure temperatures. Of particular interest are the three thermocouples in the tunnel combustor, located at x/d_{eq} = 12.2, 18.7 and 42.9, on the centerline of the wall opposite the

injection wall. Two more thermocouples are located on the injector wall. The first is on the centerline and at $x/d_{eq} = 27.2$ and the second is located at $x/d_{eq} = 20.6$ and $y/d_{eq} = 2.2$. These thermocouples are placed 0.8 mm (1/32 inch) beneath the wall surface in order to obtain wall temperatures.

The thermocouples operated in the recommended temperature range for type-K thermocouples and consequently voltage output calibration curves are well known, helping to reduce errors. Manufacturer reported accuracy is within ±2ºC [Omega, 2001].

C h a p t e r 3

3. Experimental Results

3.1. Visual Observations

During the experiments, a digital camcorder was set up to record the runs and to allow for observations in the control room of the on-going experiments. Typical snapshots of the facility in operation with hydrogen and ethylene fuel are presented in Figure 3.1. On the lower half of the picture, the observation windows are visible, where a bright light can be seen. This is primarily due to light emitted from the plasma torch and to a lesser extent to fuel combustion. The flame due to fuel combustion can be seen at the facility exhaust station. For the hydrogen case, the flame has a green glow, owing to the erosion of the anode which results in the presence of copper in the flame. The ethylene flame has a blue glow, a typical emission for good hydrocarbon combustion. Note that the red arrow indicates the location of the plasma torch.

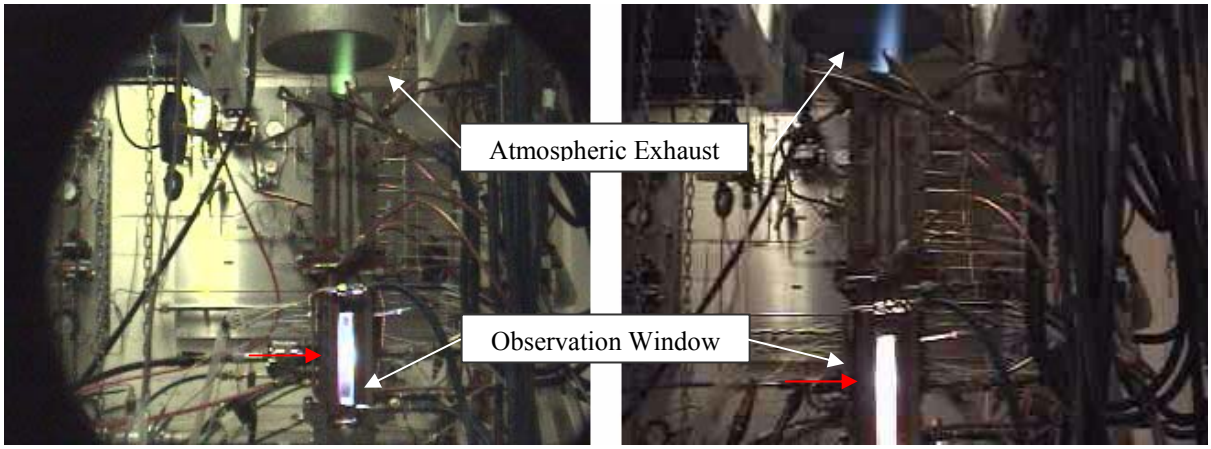

Figure 3.1. The facility in operation with hydrogen (left) and ethylene (right) fuels. The red arrow indicates the location of the plasma torch.

3.2. Wall Static Pressures

Results from the wall static pressure measurements for each fuel are presented in the following sections. All pressure profile graphs present the measured pressure normalized by the freestream static pressure value (typically 41 kPa) versus the non-dimensional length

along the combustor. Operability limits for each fuel are reported as a range of global equivalence ratios. However, it is important to understand what these limits mean. They are the operability limits for a scramjet combustor with similar geometry to that of the SCF. The lower limit is typically the lowest global equivalence ratio tested for which combustion was detected. Two factors contribute to the upper limit. First is the maximum pressure rise ratio achieved, which is maintained below the normal shock pressure rise ratio for a Mach 2 flow, i.e., 4.5. If this pressure rise was obtained, it would cause an engine unstart. The second factor is the amount of heat that can be released into the system, which was limited by safety concerns.

Recall that the center of the aeroramp injector is located at $x/d_{eq} = 0$, the isolator inlet is at -96, the 2.9-deg divergence is at 19 and the atmospheric exhaust is at 114. On the lower part of each pressure profile figure, a schematic of the facility is shown, indicating the injector location, the point at which the divergence begins and the exhaust location.

3.2.1. Heat Release due to the Plasma Torch

A reasonable question to ask is how much of the pressure rises observed are due to the heat input to the system by the plasma torch? Is it possible for the pressure rises to be solely due to the plasma torch and not to the combustion of fuel?

To answer this question, a pressure scan with the plasma torch operating at $\mathcal{P} = 4$ kW and with no fuel injected was obtained. The resulting wall pressure profile is presented in Figure 3.2. There is a localized pressure rise at the location of the plasma torch, but, other than that, the profile is almost identical to the fuel-off/torch-off case. Further, assuming that a typical 10% of the torch power is converted into heating the feedstock, then the heat release due to the torch is less than 1% of the heat released due to combustion of hydrogen for $\varphi = 0.087$. So, we conclude that the effect of the torch on the observed pressure is insignificant.

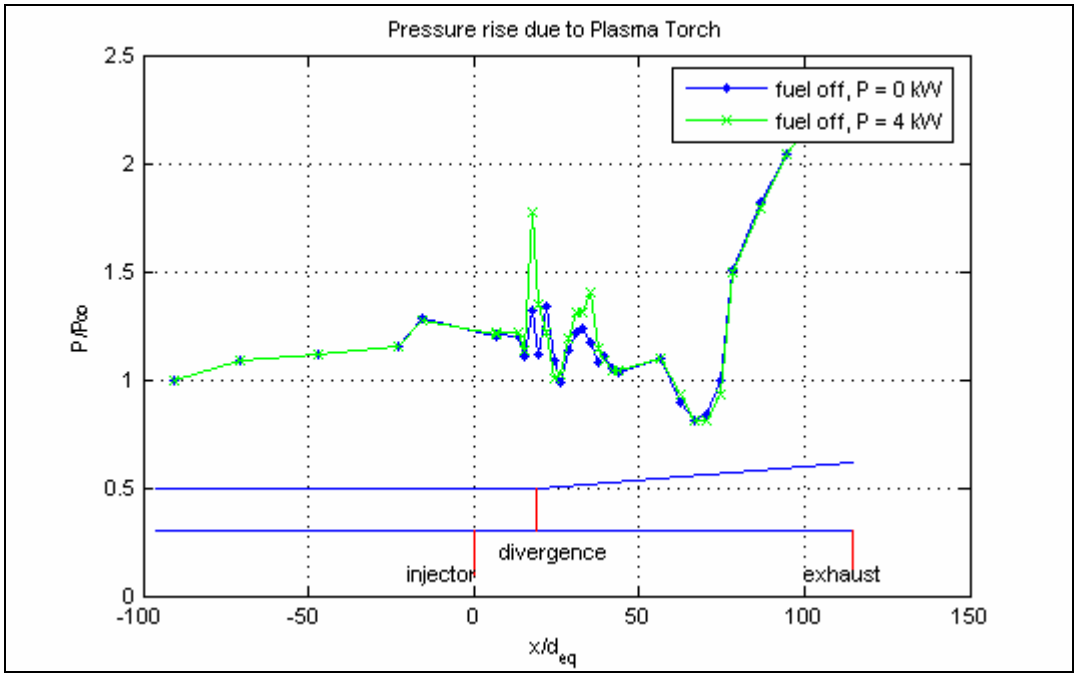

Figure 3.2. Effect of plasma torch power on wall static pressure.

3.2.2. Hydrogen Fuel

3.2.2.1. Base Case, T_o = 1000 K

Hydrogen experiments were performed with the plasma torch at station 2 ($x/d_{eq} = 8$), with nitrogen as the feedstock gas flowing at 40 slpm and an average power of $\mathcal{P} = 3.5$ kW. Combustion was demonstrated through a range of equivalence ratios, namely $0.08 \leq \varphi \leq 0.31$, and the obtained pressure profiles are presented in Figure 3.3. The jet-to-freestream momentum flux ratio was calculated to be between $0.5 \leq \bar{q} \leq 2$, depending on φ.

The first pressure profile of Figure 3.3 is for the fuel off case. This is the baseline profile to which the reacting cases are compared to determine whether combustion is obtained. Since no injection is occurring, the pressure is almost constant. The observed variations are attributed to disturbances from imperfections in the tunnel-injector plate and injector plate-anode unions. Near $x/d_{eq} = 80$, the high backpressure (atmospheric exhaust) causes a shock that decelerates the flow prior to the exhaust. The second and third pressure profiles are for φ's of 0.083 and 0.116, respectively. These are the supersonic combustion cases, since the pressure rise is less than the theoretically predicted pressure rise for thermally choked flow and also because there is no pressure rise in the isolator. At the location of the fuel injector, there is a steep pressure rise indicating ignition and after a peak pressure rise is

reached, the pressure slowly decreases, due to the divergence in the tunnel walls. As the equivalence ratio is further increased, so is the heat release due to combustion. Since the rate of area increase is not sufficient to relieve the thermal blockage, an oblique shock train system with a supersonic core flow will form in the combustor isolator. This is what is observed in the final two pressure profiles of Figure 3.3, for φ's of 0.209 and 0.313.

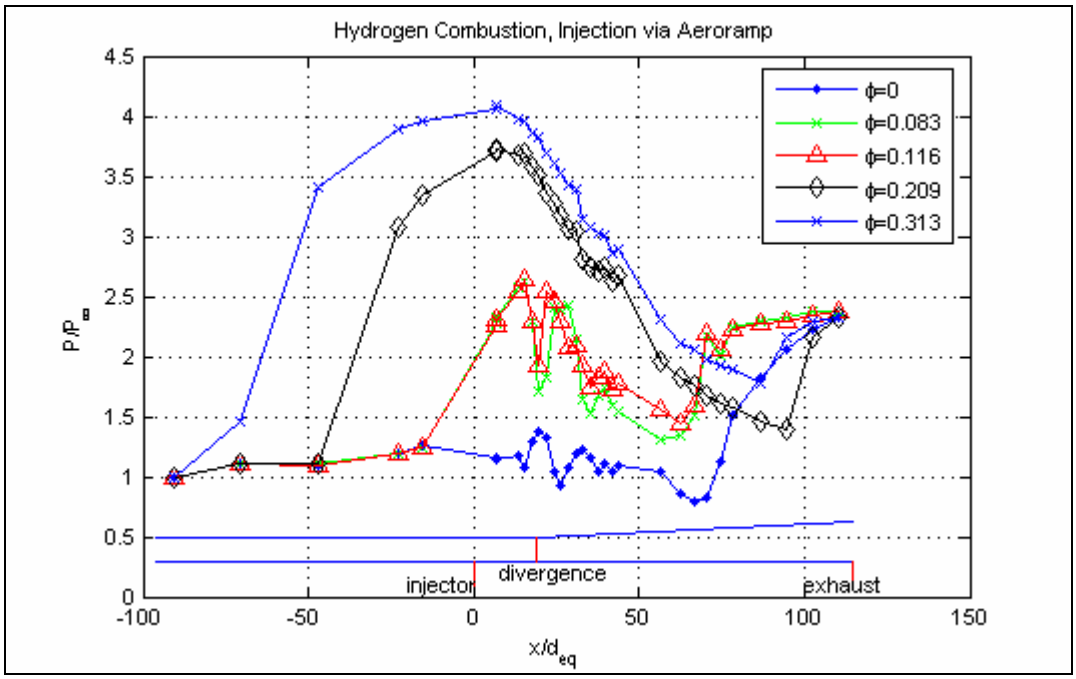

Figure 3.3. Hydrogen combustion with Aeroramp injection at T_o = 1000 K. Normalized wall pressure distributions vs. axial location.

From visual interpolation of the pressure profiles, transition from scram to dual-mode ramjet operation occurred around $\varphi_{trans} \approx 0.18$, at which point the combustor can sustain a maximum pressure rise ratio of ~3, a result that is in good agreement with the theoretical prediction of the Rayleigh flow analysis presented earlier in section 1.1. Further increasing the equivalence ratio will cause the shock train to terminate with a normal shock and combustion becomes subsonic. At the highest equivalence ratio, the maximum wall pressure ratio rise obtained was ~4.1. Note that for M = 2, the normal shock pressure ratio is 4.5.

3.2.2.2. Comparison with Physical Ramp

Experiments have been performed earlier in the SCF for injection of hydrogen through a physical 10-degree unswept compression ramp, as shown in Figure 1.8 (a). Results from this study are presented by Le et al. [2005]. The only differences in the configurations was that the physical ramp was placed on the wall opposite the aeroramp injection wall and

that once ignition was achieved there was no need for a flame-holding device, such as a plasma torch, since the subsonic recirculation region downstream of the ramp was capable of sustaining the combustion. Also, the ramp had a supersonic conical nozzle with an exit Mach number of $M_j = 1.7$. Results from this study are presented in Figure 3.4. The operability range for the 10-deg ramp is $0.07 \leq \varphi \leq 0.31$, and the transitional equivalence ratio is again $\varphi_{trans} \approx 0.18$. The range of jet-to-freestream momentum flux ratios was $0.8 \leq \bar{q} \leq 3.5$.

The pressure profiles for the two systems appear very similar, showing the same maximum wall pressure ratio rise for the same equivalence ratio. Considering the fuel-off case, a much cleaner pressure profile is obtained for the aeroramp (average P/P_∞ variation of ±18% vs. ±32% for ramp); highlighting the design advantage of the aeroramp, namely lower disturbances and total pressure losses, lower heat loads for the combustor and reduced blockage. The initial gradient of the pressure curves is steeper for the ramp, due to the oblique shock off the ramp leading edge. This has the beneficial effect of anchoring the combustion over the injector, thus reducing effective mixing lengths and ignition delay times.

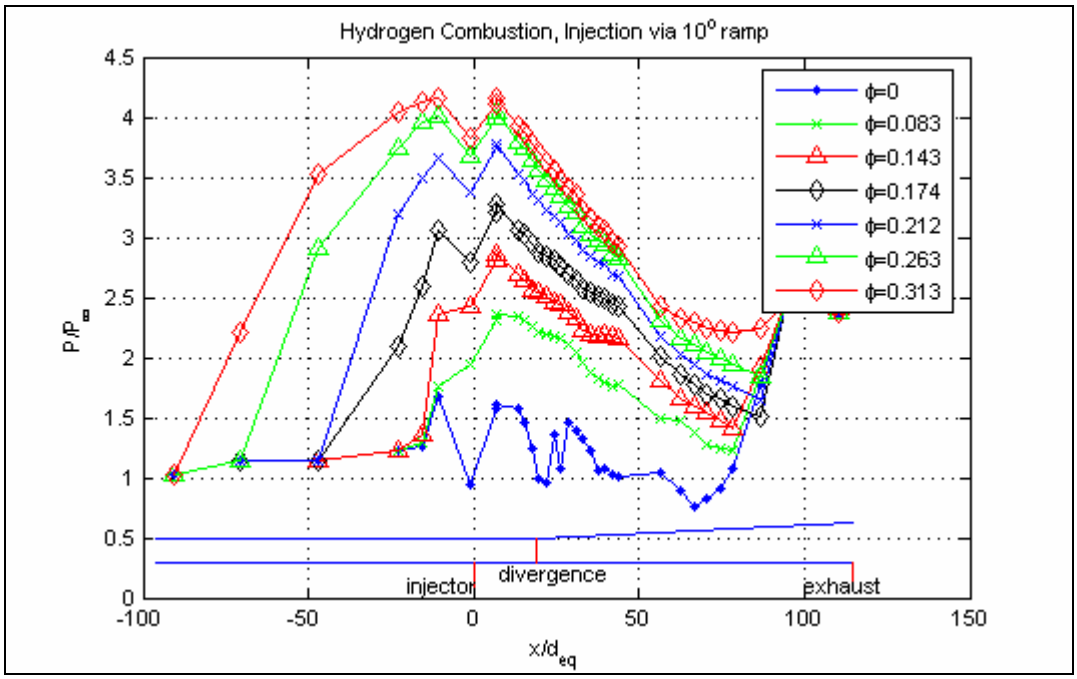

Figure 3.4. Hydrogen combustion with 10-deg ramp injection at T_o = 1000 K. Normalized wall pressure distributions vs. axial location [Le, 2005].

3.2.2.3. Total Temperature Variation

The effect of varying the tunnel total temperature was investigated, with total temperatures of T_o = 820, 610 and 530 K being considered. The range of equivalence ratios

tested was not as wide as for the baseline case, however both supersonic and dual-mode combustion were demonstrated at all temperatures. Wall pressure profiles for supersonic combustion are shown in Figure 3.5. Note that as the total temperature is decreased, less heat release is required to produce thermally choked flow, so the equivalence ratio is decreased. The physical parallel to varying the tunnel total temperature is varying the flight Mach number and altitude, i.e., the base case test conditions correspond to M = 4.22 flight at 88,000 feet and the T_o = 530K case conditions correspond to M = 2.7 flight at 43,100 feet.

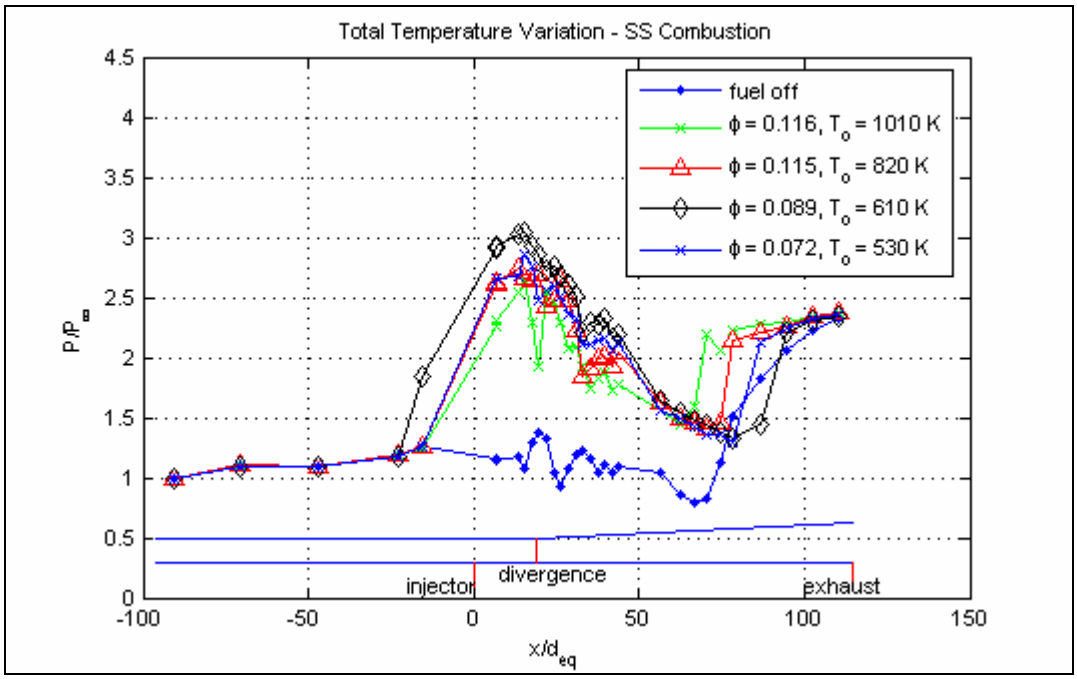

Figure 3.5. Demonstration of supersonic combustion throughout the range of tested air total temperatures with hydrogen fuel.

Figure 3.6 shows the effect of decreasing the total temperature while maintaining a constant φ = 0.11 (±5%). Transition from supersonic combustion to the dual-mode regime can be seen as the air total temperature is decreased passed 820 K. As the total temperature is decreased at constant total pressure, one is, in essence, increasing the mass flow through the engine. Thus, more fuel is required to maintain the constant φ, so there is more heat release at the lower T_o.

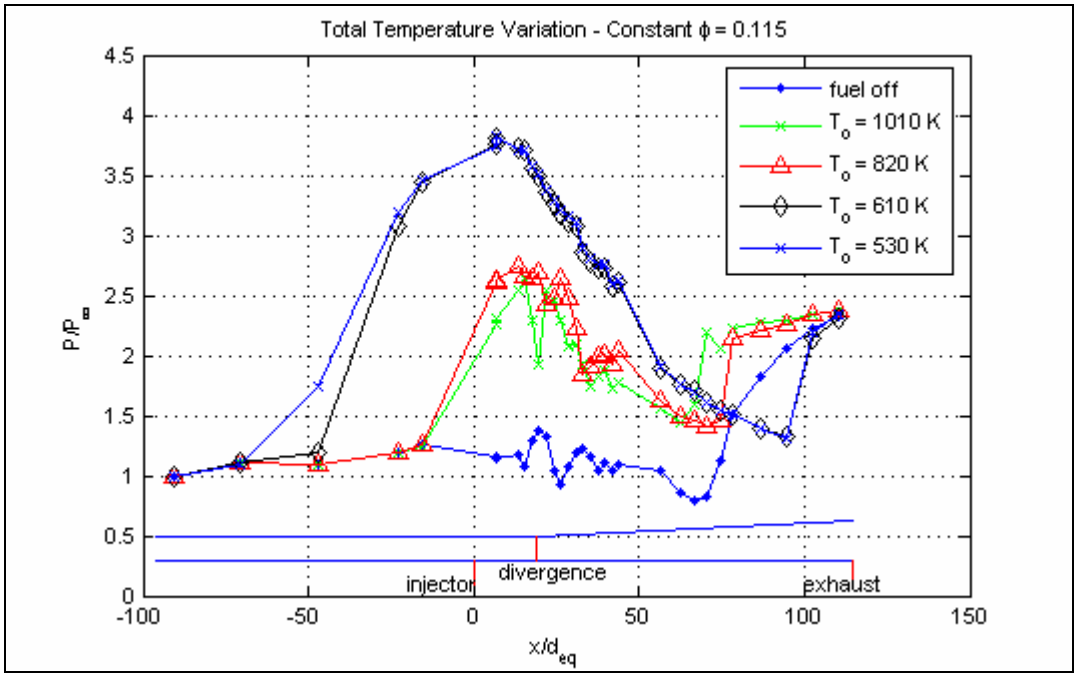

Figure 3.6. Effect on wall pressure from varying the air total temperature while maintaining a constant equivalence ratio.

3.2.2.4. Performance Map

A map showing the operability ranges tested with the current configuration is shown in Figure 3.7. It is created by plotting tunnel total temperature vs. equivalence ratio and is useful guide to indicate the region in which the system can be operated. Again, the upper limit in this graph is determined by the shock strength in the facility isolator, maintaining the pressure rise below the normal shock pressure ratio.

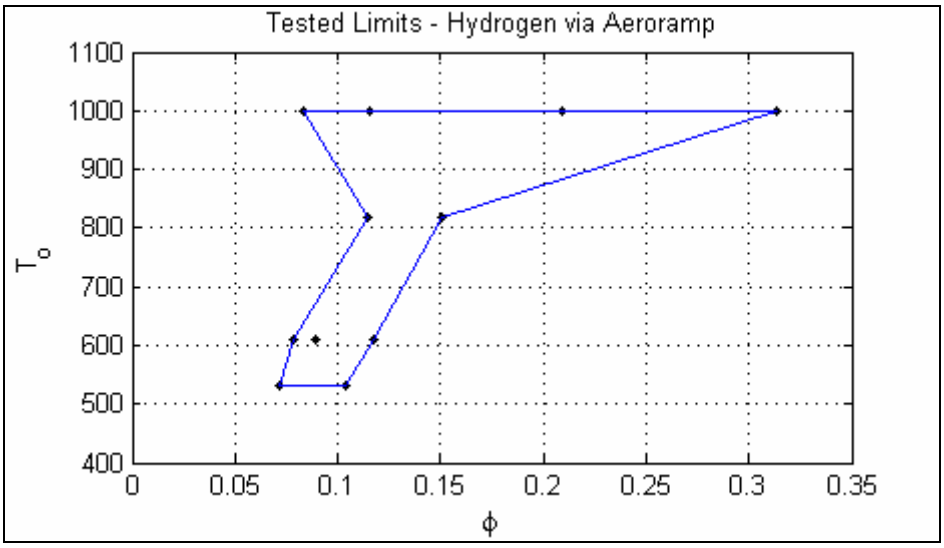

Figure 3.7. Performance map, showing tested equivalence ratio ranges.

3.2.3. Ethylene Fuel

Before the pressure profile results are presented and discussed, a few words about the selection of the location for the plasma torch with respect to the aeroramp injector must be said. Experiments were done with ethylene fuel and the torch in station 2, and no significant pressure rises were observed over a range of equivalence ratios and torch powers. This shows the importance of the correct integration of the injector/igniter and also how the specific fuel's reactivity and ignition limits must be taken into account when considering this design parameter. When the torch was set to station 3 with air as the feedstock gas, good combustion was observed. These results are presented below.

3.2.3.1. Base Case, T_o = 1000 K

Ethylene experiments were performed with the plasma torch at station 3 (x/d_{eq} = 10), with air as the feedstock gas flowing at 40 slpm and an average power of $\mathcal{P}$ = 6.1 kW.

Combustion was demonstrated through a range of equivalence ratios, namely $0.14 \leq \varphi \leq 0.48$, and the obtained pressure profiles are presented in Figure 3.8. The jet-to-freestream momentum flux ratio was calculated to be between $0.6 \leq \bar{q} \leq 1.8$, depending on φ.

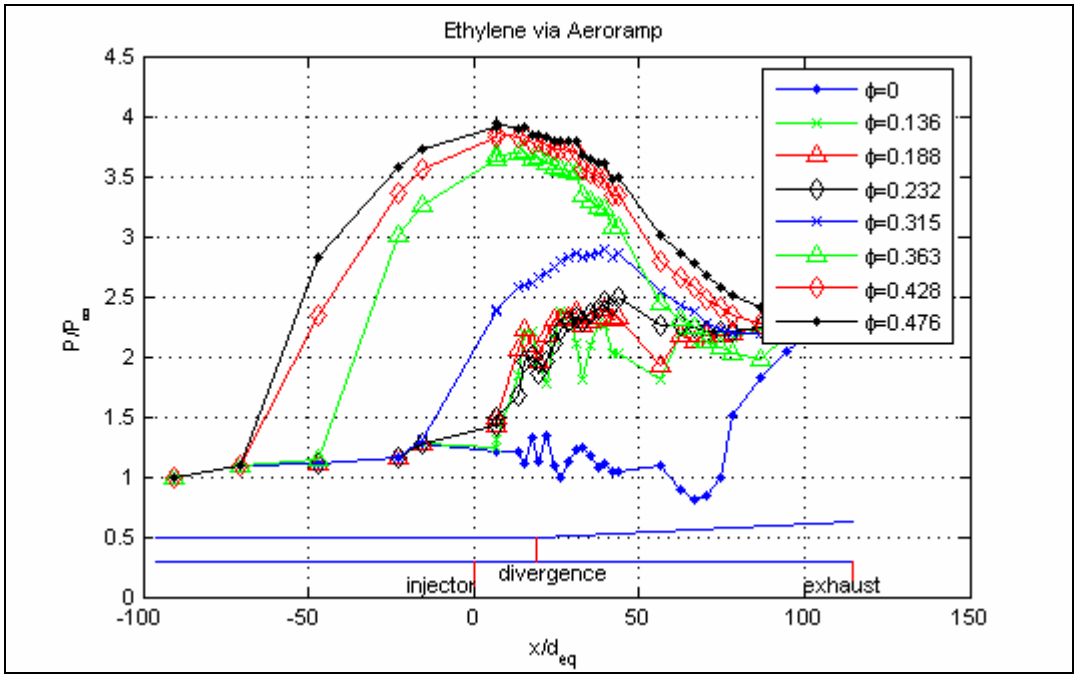

Figure 3.8. Ethylene combustion with Aeroramp injection at To = 1000 K. Normalized wall pressure distributions vs. axial location.

The same features as the hydrogen pressure profiles are apparent, i.e., the supersonic combustion profiles followed by a transition to the subsonic combustion mode with the accompanied pressure rise in the isolator. Again, the fuel-off case is presented as a baseline for comparison. An interesting observation regarding the supersonic combustion cases is that as φ is increased from 0.136 to 0.188 and above, the decrease in pressure at the divergence station (also seen in the hydrogen cases) disappears, indicating that the combustion is steadier and stronger, in the sense that it is not influenced as much from the freestream and is better anchored near the injector.

As with hydrogen fuel, transition from the pure scram mode to the dual-mode ramjet is achieved. From the expected pressure rise ratio predicted by the Rayleigh flow, and from inspection of the pressure profiles, the transition equivalence ratio is approximately $\varphi_{trans} \approx 0.32$, where the combustor can again sustain a maximum pressure rise ratio of ~3. The maximum wall pressure ratio rise obtained for the highest equivalence ratio was ~4, again close to the normal-shock pressure rise. In general, the same pressure rise as with hydrogen could be reached for ethylene with a higher equivalence ratio, which is expected, considering the relative energy density of the two fuels. Higher torch powers were required in order to create local conditions that would favor ignition, since the ignition delay times of the two fuels differ by an order of magnitude.

3.2.3.2. Total Temperature Variation

Again, the effect of varying the tunnel total temperature was investigated, with total temperatures of $T_o = 830$ and 680 K being considered. The range of equivalence ratios tested was not as wide as for the baseline case; however both supersonic and dual-mode combustion were demonstrated at these temperatures. Wall pressure profiles for supersonic combustion over the temperature range tested are shown in Figure 3.9. Due to operational limitations – primarily torch life – further temperatures and equivalence ratios were not investigated.

The measured supersonic combustion profiles have a large region of constant pressure, extending from $x/d_{eq} = 15$ to 40. Since this region is almost entirely past the divergence section, the conclusion that can be reached is that the rate of area increase of the tunnel is just right to provide thermal relief for the heat release due to combustion, and so a constant pressure is obtained throughout this length. Also, since there is heat release, it further indicates that combustion is occurring throughout this length. In the base case of $T_o = 1000$K, the reaction rates are faster, leading to a shorter constant pressure region and eventually a pressure decrease.

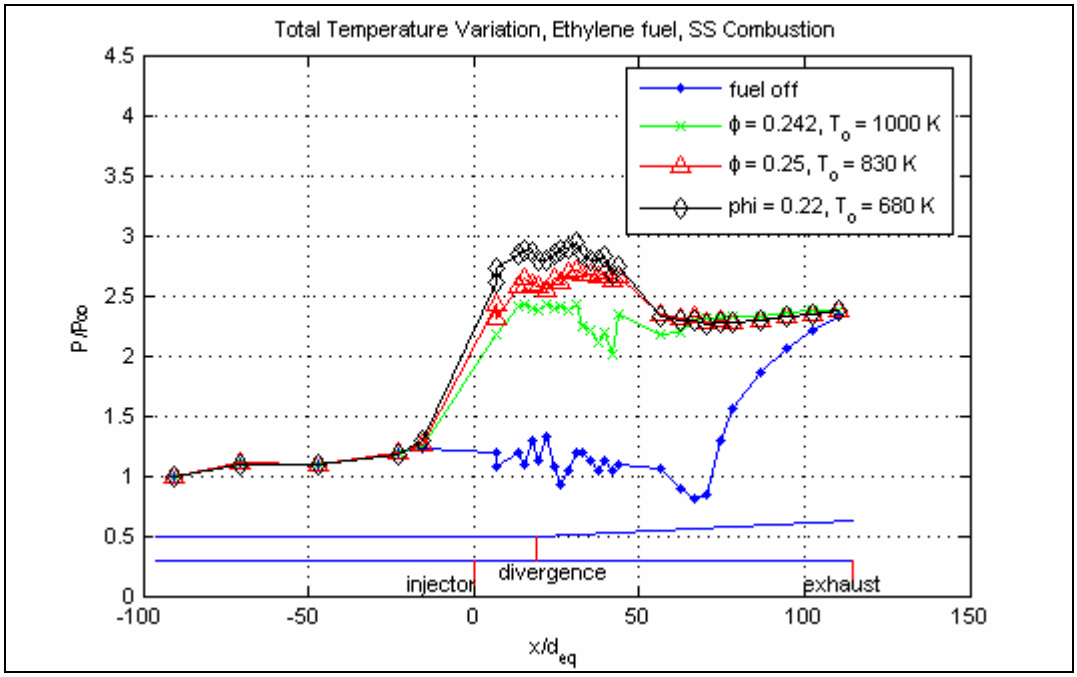

Figure 3.9. Demonstration of Supersonic combustion throughout the range of tested air total temperatures with ethylene fuel. Normalized wall pressure distributions vs. axial location.

3.2.4. Methane Fuel

3.2.4.1. Base Case, T_o = 1000 K

Methane experiments were performed with the plasma torch at station 3 (x/d_{eq} = 10), with air as the feedstock gas flowing at 40 slpm and an average power of $\mathcal{P}$ = 6.5 kW.

Pressure profiles obtained from this study are presented in Figure 3.10. From these profiles, it is apparent that the extent of combustion was very limited. The pressure rise at x/d_{eq} = 6, upstream of the torch, indicates that there is some combustion and flame propagation. The pressure rises around x/d_{eq} = 35 further reinforce this. Note that the pressure rises at x/d_{eq} = 17 are attributed to the torch.

Physically, what is happening is that the high operating power of the plasma torch causes the fuel to ignite locally. However, the high ignition delay times of methane coupled with insufficient mixing and improper local mixture conditions do not allow the flame to propagate, so the flame is quenched downstream in the combustor.

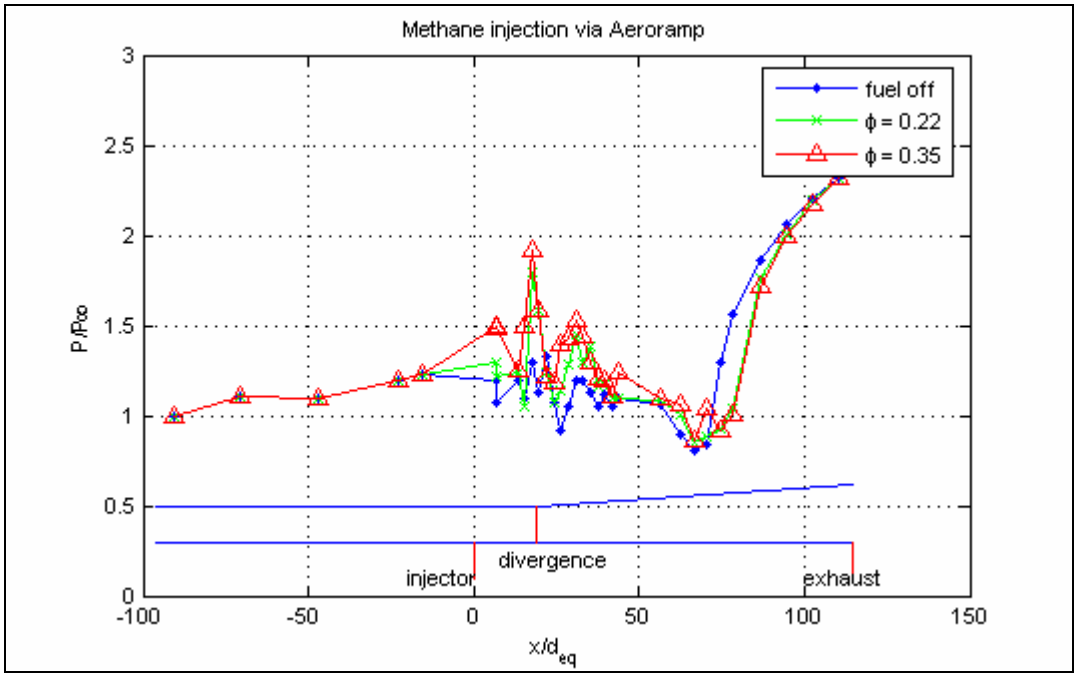

Figure 3.10. Methane injected via aeroramp at T_o = 1000K. Normalized wall pressure distributions vs. axial location.

Similar pressure profiles had been obtained in the early ethylene tests, with the plasma torch in station 2. This indicates that successful methane combustion might be achieved if the torch were to be placed at a different location. A CFD simulation of the methane mixing case was performed, and it predicted that the mixture in station 3 would be too rich for ignition (see section 5.7.2.2 for more details).

Since combustion was not observed at the highest tunnel total temperature, the study was limited to the base case, and lower total temperatures were not investigated.

3.3. Wall Temperatures

Temperatures in the stainless steel wall below the zirconia layer were monitored throughout the experiments and recorded at three locations, at x/d_{eq} = 12.2, 18.7 and 42.9, on the centerline of the wall opposite the injection wall. Table 3-1 shows average temperatures vs. equivalence ratio for hydrogen and ethylene fuels at the three locations, for the base total temperature case. The observed trend is that higher wall temperatures were recorded in the subsonic combustion modes, which makes sense since the subsonic combustion implies that a thermal choke has been reached in the flow because of larger heat release.

fuel	φ	T_1 (°C)	T_2 (°C)	T_3 (°C)	combustion
off	--	102	128	107	--
Ethylene	0.242	117	154	133	supersonic
	0.36	136	180	151	subsonic
Hydrogen	0.083	128	167	130	supersonic
	0.114	121	160	127	supersonic
	0.208	141	186	147	subsonic
	0.311	137	180	145	subsonic

Table 3-1. Average wall temperatures [°C] at three locations for the base case (T_o = 1000 K), T_1 at x/deq = 12.2, T_2 at 18.7 and T_3 at 42.9. Also noted is the combustion mode, supersonic or subsonic.

3.4. Conclusions Based on Direct Data Observed

These data allow some conclusions to be reached at this point. Further interpretation will be presented with the aid of the Ramjet Performance Analysis code, presented in Chapter 4.

Successful subsonic and supersonic combustion was achieved with hydrogen and ethylene fuels, achieving transition from scram to dual mode combustion. Full advantage was taken of the isolator to achieve the range of operating conditions. Different tunnel total temperatures were investigated, and supersonic combustion was achieved for temperatures as low as 530K for hydrogen and 680K for ethylene. This indicates the robustness of the plasma torch as an ignition and flameholding device and how it can be used to minimize effective ignition delay times and ignition energy requirements.

The correct integration of the plasma torch with the injector array was also demonstrated, since combustion was achieved. It is important to note that the plasma torch was also a flameholding device, since when the torch was extinguished the combustion would also stop.

A good starting point for future methane experiments was set. Despite the lack of a large pressure rise, a clear sign of combustion, some heat release was obtained, indicating that combustion might be possible if a more suitable location for the plasma torch is selected.

The conclusions of the experimental part of the study can be summarized as follows:

- Good operational locations of the plasma torch were determined for hydrogen and ethylene fuels.
- For hydrogen fuel at the base case condition of T_o = 1000 K, operability ranges were determined to be $0.07 < \varphi < 0.31$.
- For ethylene fuel at the base case condition of T_o = 1000 K, operability ranges were determined to be $0.14 < \varphi < 0.48$.

- Hydrogen combustion (both subsonic and supersonic) was achieved at total temperatures as low as 530K. This was a facility limit and not an extinction limit.
- Ethylene combustion was achieved at total temperatures as low as 680K. Combustion at lower temperatures seems likely, however it was not tested due to torch life limitations.
- Excellent agreement in wall-static pressure profiles between the aeroramp and a physical 10-degree compression ramp was obtained for hydrogen fuel.
- The importance of careful integration of the aeroramp fuel injector and the plasma-torch igniter was demonstrated.
- Limited heat release was obtained with methane fuel. This result, coupled with the long ignition delay time of methane leads to the conclusion that the torch needs to be placed further downstream.
- On average, temperature rises for subsonic and supersonic combustion were 20 and 40 K respectively.

C h a p t e r 4

4. Data Interpretation with the Ramjet Performance Analysis Code (RJPA)

4.1. RJPA Overview

The Ramjet Performance Analysis code, or RJPA, is a one-dimensional integral simulation code aimed at estimating the performance of scramjets and dual-combustion ramjets as well as rocket operations and supersonic dump combustors [Pandolfini, 1992]. The code has been under continuous development since the 1970's at The Johns Hopkins University Applied Physics Laboratory (JHU/APL) and is considered an industry standard for analysis of scramjet, ramjet and rocket cycles.

The code breaks the engine down into components, based on the flow-field that dominates in each region. These components are the freestream, the diffuser, the combustor and the exhaust nozzle. A control volume defines each of these components allowing the use of an integral approach. A one-dimensional representation of the flow at each component inlet/exit station is made. The program, at each station, searches for conditions that satisfy the integral conservation equations, the equations of state and certain empirical models. A schematic of the engine breakdown is given in Figure 4.1.

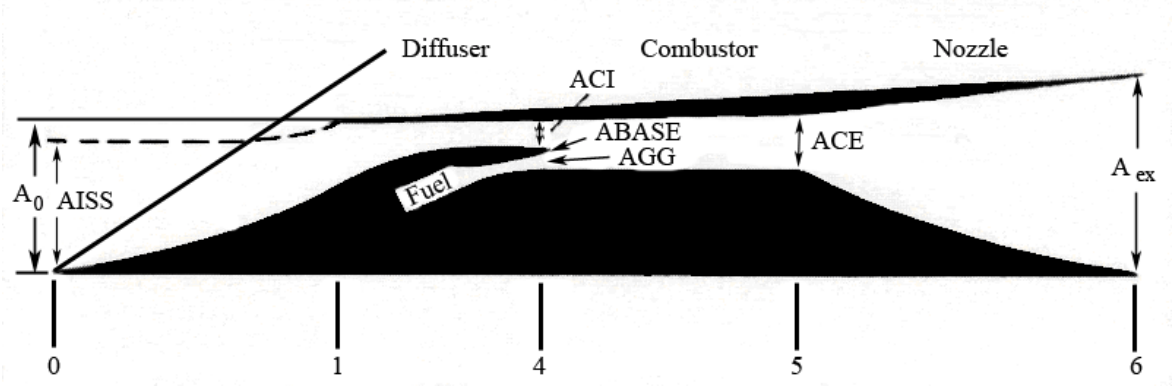

Figure 4.1. Breakdown of a generic engine showing the component analysis regimes [Pandolfini, 1992].

RJPA performs one-dimensional heat addition into a variable area duct calculations, taking friction into account. The properties of the engine cycle fluid (the mixtures of fuel and oxidizer) are obtained from a defined set of atomic mass fractions. Chemical composition is determined, assuming thermochemical equilibrium, using curve fits of JANNAF thermochemical data.

This code is capable of providing a general analysis with an uncertainty in results of about 15% [Billig, 2004-2005]. This is due to the large amount of empirical data that is built into the code for several models it employs, such as the value for the skin friction coefficient, the assumed diffuser efficiencies, etc.

In this chapter, the performance characteristics of the integrated aeroramp/plasma torch system are analyzed using RJPA. The experimental conditions though were obtained through direct-connect testing of the injector igniter design and, we wish to analyze the complete engine with RJPA. To this end, a "theoretical" inlet and nozzle are assumed for the direct-connect tests. The choices made for these components will be justified in the following section.

4.2. RJPA Input Parameters

RJPA takes a great deal of geometry and flow characteristics into account when analyzing each engine. A detailed list of the input variables along with an explanation of what each refers to is given in the RJPA instruction manual by Pandolfini [1992]. The following sections go through these inputs and explain the choices made here for each parameter.

As mentioned above, the code breaks the engine into components. A screenshot of the main deck of the program is shown in Figure 4.2. Here, the user selects the components to be included in the calculations. The "inlet" tab refers to the freestream condition. The order outlined from this figure will be used to specify the inputs for each component.

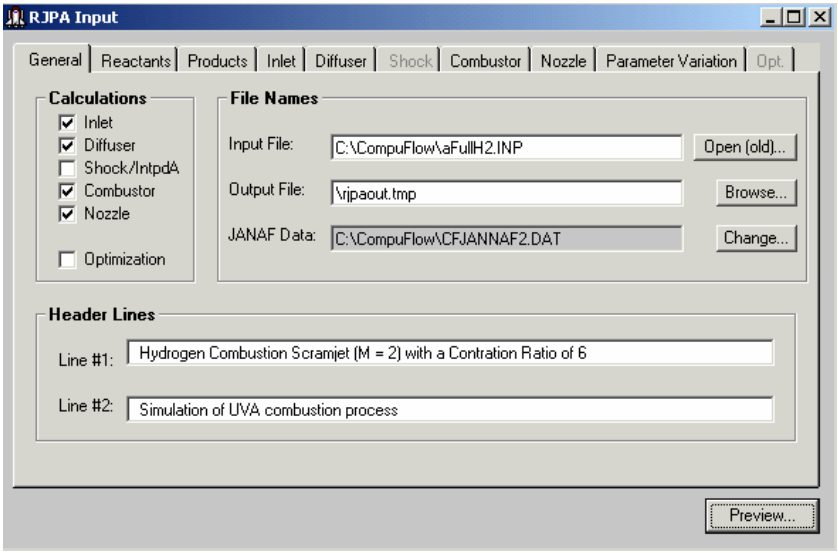

Figure 4.2. RJPA general input deck. The components to be included in the analysis are set here.

4.2.1. Freestream and Diffuser Conditions

The "inlet" module, referring to the freestream conditions, is shown in Figure 4.3. Here, the user can select the flight altitude and Mach number as well as the supersonic inlet capture area. The goal is to select an appropriate combination of values such that the diffuser exit conditions match up with the experimental conditions in the isolator inlet. Based on this criterion, the properties of the "theoretical" inlet were determined.

For a reasonable contraction ratio (inlet capture to combustor area) of 6, and with a freestream flight Mach number $M_\infty = 4.15$ at h = 86,000 ft, the exit conditions (Mach number, pressure and temperature) are within 2% of the current experimental conditions. Note that RJPA has the capability of using a premixed fuel-air mixture as the freestream gas. The initial oxidizer-to-fuel ratio is set to $1.0e^{12}$ to indicate that there is no fuel in the freestream.

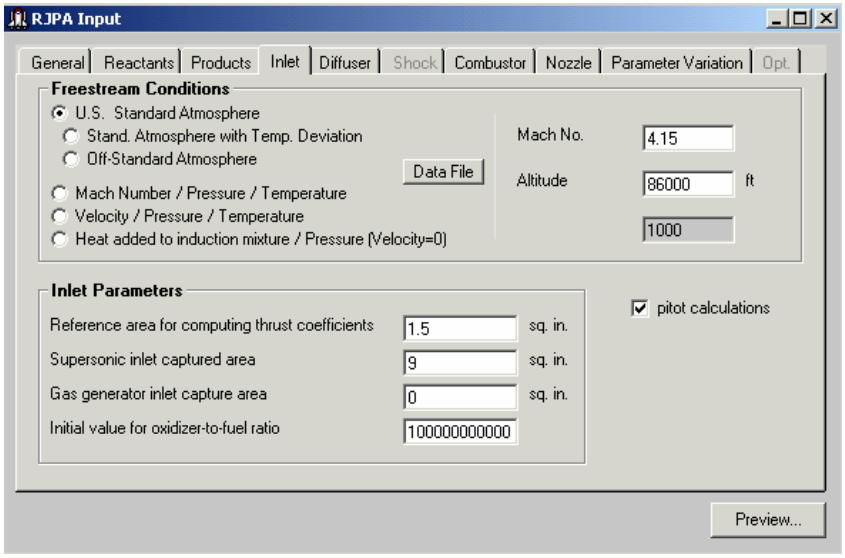

Figure 4.3. RJPA "inlet" module. Here the freestream conditions are defined.

The "diffuser" module is presented in Figure 4.4. Under this tab, the parameters for the diffuser are defined. The diffuser exit parameter is chosen to be the area, set to $9.7e^{-4}$ m^2 (1.5 in^2) since this is the area of the experimental combustor. The program can take friction losses in the diffuser into account. For this purpose, a kinetic energy efficiency parameter is defined and set equal to 98.2%. This is the default value for this parameter and seems like a reasonable choice.

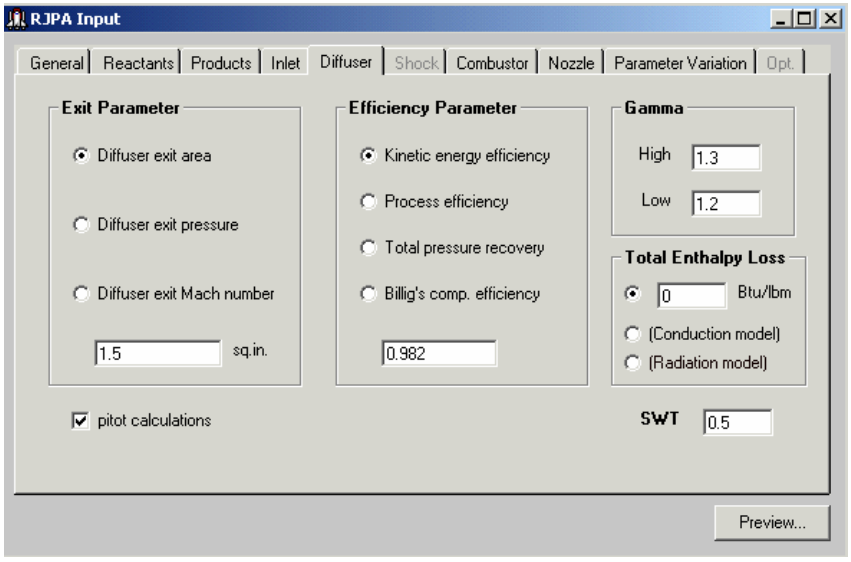

Figure 4.4. The RJPA "diffuser" module.

4.2.2. Shock and Combustor Modules – Reading the Experimental Data

RJPA has the capability of including an oblique or normal shock prior to the combustor. This module could be used to model the pressure rise occurring in the isolator

when the combustor was operating in the dual mode regime. However, this pressure rise can also be modeled in the "combustor" module as the pre-combustion shock pressure rise, or PSPCI, parameter. The latter approach was preferred, so the "shock" module was not used in these calculations.

The "combustor" module, shown in Figure 4.5, is where the majority of the specific current test data is input into the program. The input deck is separated into two main parts, the inputs for the combustor and the inputs for the gas generator. The gas generator is used to specify the properties of the fuel and injector, such as injector area ($7.9e^{-4}$ m^2 or 0.0123 in^2) and angle (30-deg), fuel molecular weight, enthalpy, speed and temperature. The density (RHOGG) is set to zero, such that the program will compute it based on the specific equivalence ratio tested.

There are seven different calculation modes than can be done, but typically only one is appropriate based on the experimental data at hand. In the present calculations, the "Option 1" was selected, namely combustor calculations were performed without entropy limit constraint and with the combustor exit area and PSPCI specified. The result of the calculation would be the combustor exit pressure (PCE). Of course, this value is known from the experimental results, but did not by default match up. The amount of fuel that reacted needed to be altered in order for the PCE to agree. This process will be explained in more detail later.

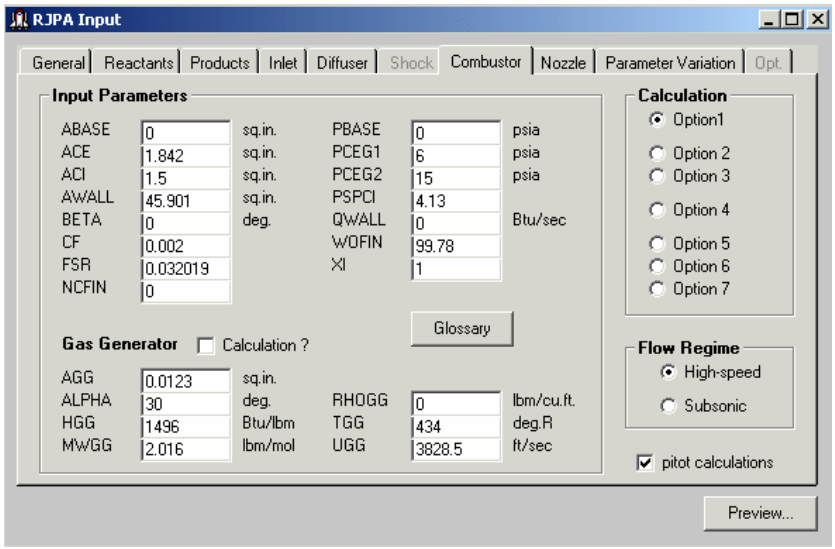

Figure 4.5. The "combustor" module of RJPA.

Specifically, for the combustor parameters, an inlet and exit area needed to be specified. The inlet area is known and equal to $9.7e^{-4}$ m^2 (1.5 in^2), but the exit needed to be determined. An overall combustor length of 23 cm was selected, from -5 to 18 cm (-16 <

$x/d_{eq} < 56$), such that the inlet and exit locations were at stations where the pressure was measured, and also such that the influence of the shock prior to the atmospheric exhaust was not yet realized. This resulted in an exit area of $1.2e^{-3}$ m^2 (1.842 in^2) and a combustor wall area of $2.9e^{-2}$ m^2 (45.9 in^2). The wall area is needed because the skin friction is taken into account. A value for the skin friction coefficient, C_f, can be manually entered or computed through an internal curve fit. The latter approach was used, such that the effect of heat release on skin friction was also taken into account, instead of using a simple constant value. On average, C_f was approximately 0.0023. Finally the fuel-to-air stoichiometric ratio (FSR) was input in this section, and based on this the WOFIN parameter was computed to be 1/FSR/φ. WOFIN is the ratio of the diffuser flow to the total gas generator outflow. Table 4-1 summarizes the "combustor" module input parameters for different test conditions and fuels tested in this work.

Fuel	To	φ	WOFIN	PSPCI	%FRZN	PCE	QWALL
H_2	1000	0.083	376.28	1.27	33.0	8.05	3.407
		0.116	269.24	1.28	36.0	9.66	3.561
		0.209	149.43	3.43	46.6	12.08	4.133
		0.313	99.78	4.06	61.4	14.23	4.995
	820	0.115	271.58	1.28	51.5	10.04	--
		0.151	206.83	3.19	48.3	11.28	--
	610	0.078	400.40	1.25	55.6	9.12	--
		0.089	350.92	1.84	52.5	9.85	--
		0.117	266.94	3.44	50.2	11.40	--
	530	0.072	433.77	1.26	57.1	9.35	--
		0.104	300.30	3.46	51.9	11.46	--
C_2H_4	1000	0.136	99.02	1.31	25.8	10.86	2.919
		0.232	58.04	1.31	48.4	13.60	3.552
		0.363	37.10	3.26	59.14	14.70	4.748
		0.476	28.29	3.73	67.6	15.66	6.086

Table 4-1. RJPA "combustor" module input parameters for different fuels and test conditions. Note that PCE is in [psi] and QWALL in [BTU/sec].

4.2.2.1. Wall-Cooling Considerations

The combustor module of RJPA can account for heat added or removed from the system with the Q_{WALL} parameter. Since the test facility has wall cooling installed, this effect needs to be taken into account. A cooled facility that gives the same pressure rise as an un-cooled facility is more efficient, since the same pressure trace is obtained even though energy is removed from the system.

To estimate the heat loss through the walls, the following formula was used:

$$\overline{q} = h(T_{a,w} - T_w) \tag{4.1}$$

where h is the film coefficient, $T_{a,w}$ is the adiabatic wall temperature and T_w is the wall temperature [Holman, 1990].

The film coefficient can be obtained from rearranging the terms in the Reynolds analogy (relation between skin friction and heat transfer) as follows:

$$h = \frac{C_f k \,\mathrm{Re}\,\mathrm{Pr}^{1/3}}{2L} \tag{4.2}$$

where C_f is the skin friction coefficient, k is the thermal conductivity, Re is the Reynolds Number, Pr is the Prandtl Number and L is the length of the combustor (23 cm). The skin friction coefficient (C_f) is obtained from the same curve fit used in RJPA and is only a function of the equivalence ratio φ:

$$C_f = (7.9291\phi^2 + 1.3203\phi + 1.7699)10^{-3} \tag{4.3}$$

The thermal conductivity of air (at 500K) was k = 0.038 W/m-K and the Prandtl number Pr = 0.706. The Reynolds number for the facility was computed to be $2.8e^6$ and the length used was the combustor length, L = 0.23 m.

With h known, we still need the adiabatic wall temperature and the wall temperature. The former was calculated using:

$$T_{a,w} = T + r(T_o - T) \tag{4.4}$$

with the total and static temperatures (T_o, T) being estimated using RJPA. They were linearly interpolated between the combustor inlet and exit temperature. A turbulent recovery factor was used, $r = \mathrm{Pr}^{1/3}$ [Schetz, 1993].

Since the total heat extracted is a constant, the following formula can be used for the wall temperature:

$$Q = \overline{h}(T_{a,w} - T_w) = \frac{k}{t}(T_w - T_{probe}) \tag{4.5}$$

where T_{probe} is the temperature measured by a type-K thermocouple, at t = 0.8 mm (1/32 inch) beneath the surface, as illustrated in Figure 4.6. This temperature was set equal to the average

of the measured temperature at three stations downstream of the injector. In computing the wall temperature, only the thermal conductivity of the zirconia was assumed to be significant, since it is one order of magnitude lower than the thermal conductivity of the other materials used. We can now solve for T_w and for Q_{WALL}. These results were given in Table 4-1.

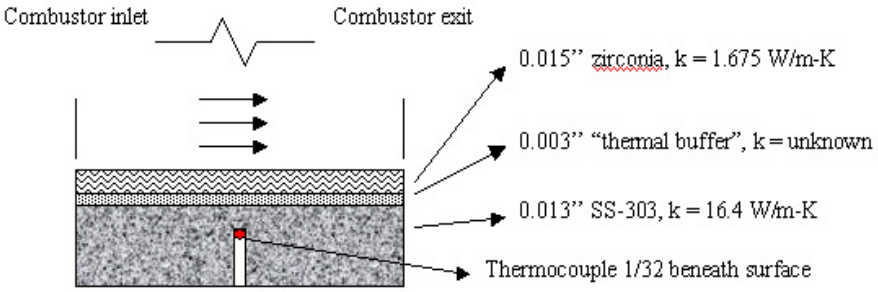

Figure 4.6. Combustor wall cross-section (not to scale) illustrating materials used

4.2.3. The Nozzle Module

The properties for the exhaust nozzle are set in the "nozzle" tab, shown in Figure 4.7. As with the diffuser, this is a "theoretical" nozzle in our case here. The exit parameter was set to the exit pressure, and was chosen to be the freestream pressure for the assumed flight conditions. In this way, the exhaust jet would be perfectly expanded and the thrust would be maximized. The ratio with which the frozen and equilibrium gases are combined in the nozzle is also set in this tab, which in turn affects the produced thrust. Thrust is reported for nozzle efficiencies of 98.5 to 100%. The lower limit of this efficiency can be set by the user, but it was left to its default value here.

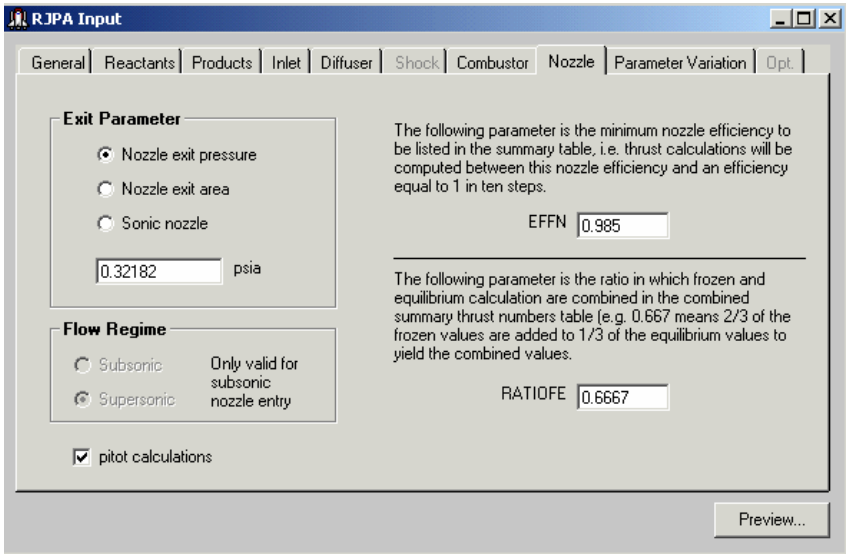

Figure 4.7. The RJPA "nozzle" module.

4.2.4. Fuels and Reactions

Once the fuel and oxidizer have been selected, the amount of fuel that remains frozen and that which actually reacts can be set. These numbers must be altered by the user so that the experimental pressure profiles are matched. In predictive studies, this can account for inefficiencies and in this case it is used to correctly match the experimental data. For example, if one sets 100% of the fuel to react, then the PCE parameter predicted in the "combustor" module will most likely be a lot higher than that found by the experiments. The amount of reacting fuel must be decreased (and the frozen fuel increased) in order for the predicted and experimental PCE to match up. This process was done iteratively until convergence was achieved. The fuel selection tab is shown in Figure 4.8.

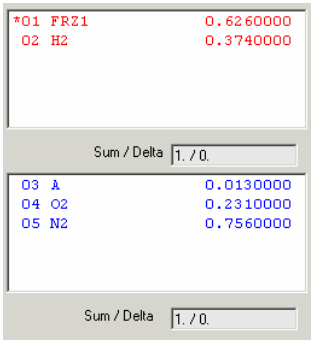

Figure 4.8. The fuels selection in RJPA, where the amounts of frozen and reacting fuel are set.

RJPA determines chemical composition assuming thermo-chemical equilibrium conditions, using JANNAF tables. The air-composition used as the oxidizer in these computations is 23.1% O_2, 75.6% N_2 and 1.3% Ar. For hydrogen fuel, 14 species (including frozen H_2) as products are specified, and for ethylene 15 species are used (including frozen C_2H_4). These species are listed in Table 4-2 for each fuel.

	Hydrogen	Ethylene
1.	A	A
2.	H	CH_4
3.	HO	CO
4.	H_2	CO_2
5.	H_2 (frozen)	H
6.	H_2O_2	HO
7.	N	H_2
8.	NO	NO
9.	NO_2	NO_2
10.	O	O
11.	O_3	H_2O
12.	H_2O	N_2
13.	N_2	O_2
14.	O_2	C_2H_4 (frozen)
15.	--	C

Table 4-2. Species considered by RJPA in the reactions for each fuel

4.2.5. Aeroramp and Physical Ramp calculations

Simulations were run comparing the aeroramp and the physical 10-degree unswept ramp test cases with hydrogen fuel. Some differences exist between the setup files for the two different injection systems. Namely, the area and blockage of the physical ramp needs to be taken into account. The axial projection of the ramp area is inserted as the A_{BASE} parameter, and the base pressure at the ramp face was approximated as one half the wall static pressure at that position. The physical ramp has a 10-degree angle and injection occurs at this angle, so the ALPHA parameter is adjusted accordingly. Finally, there is a slight increase in the wall area (A_{WALL}) to account for the additional area of the ramp vs. the flush-wall aeroramp system. The differences in the input files are summarized in Table 4-3.

	Physical Ramp	Aeroramp
A_{BASE}	0.125 in^2	0
P_{BASE}	½ local wall static	0
A_{WALL}	46.4 in^2	45.9 in^2
ALPHA	10º	30º

Table 4-3. Summary of input parameters in RJPA that must be altered when considering the physical ramp injector, as opposed to the aeroramp.

4.3. RJPA Results

RJPA can analyze experimentally obtained pressure curves from a scramjet combustor to yield engine parameters such as combustion efficiency and specific impulse. The results are presented based on the comparisons performed. First, the aeroramp injector is compared with the 10-degree unswept physical ramp with hydrogen fuel. Then the engine performance with different fuels is compared. Finally, the results for the tunnel total temperature variations are presented.

Combustion efficiency and specific impulse results are presented for each case. Both fuel and air specific impulses are shown. The air specific impulse, plotted against the product of the equivalence ratio times the fuel-to-air stoichiometric ratio times the fuel heating value, allows for a more direct comparison between curves for different fuels and injector types. This parameter tends to collapse the air specific impulse curves. The fuel specific impulse is calculated as:

$$I_{sp} = \frac{\mathcal{F}}{\dot{m}_{fuel}} \tag{4.6}$$

and the air specific impulse is defined as:

$$S_a = \frac{\mathcal{F}}{\dot{m}_{air} + \dot{m}_{fuel}} \tag{4.7}$$

where $\mathcal{F}$ is the engine thrust.

4.3.1. Aeroramp vs. Physical Ramp Case

The experimentally obtained pressure curves for injection of hydrogen through an aeroramp and a physical ramp, shown in Figure 3.5 and Figure 3.6, were analyzed with RJPA and the results are compared. Results for combustion efficiency and air-specific impulse are presented in the plot of Figure 4.9. Recall that for hydrogen fuel, transition from supersonic to dual-mode combustion occurs at $\varphi_{trans} = 0.18$. The combustion efficiency curve indicates that for both injector types, the supersonic combustion mode is more efficient, with an average $\eta_{sup} \approx 81\%$, with the efficiency dropping to $\eta_{sub} \approx 51\%$. The trend of decreasing efficiency with increasing equivalence ratio has been observed by other researchers in various supersonic combustion experiments [Northam, 1986, Andrews, 1993, Situ, 1999]. Further, these researchers present similar efficiencies for the same equivalence ratios for hydrogen.

At first glance, the physical ramp seems to be more efficient in the supersonic combustion region; for the leanest cases almost 100% efficiency is achieved. The explanation for this lies in the fact that the fuel-air mixtures are extremely lean ($\varphi < 0.08$), making the probability of combustion in the favorable region of the subsonic recirculation zone aft of the ramp face high. Once more reasonable (from an operational point of view) equivalence ratios are reached, i.e., $\varphi > 0.12$, the aeroramp is consistently more efficient. However, in all cases the differences are very small, less than 5%. Such small differences can also be attributed to errors introduced in the calculations and from errors in the pressure measurements.

Considering the air specific impulse curves, the aeroramp provides slightly higher values. One explanation for this difference can be deduced by considering the injector designs. The physical ramp forms an oblique shock at its face, which leads to total pressure losses. These total pressure losses can be directly related to the produced thrust, and so for the same pressure rise the ramp, in fact, produces less thrust.

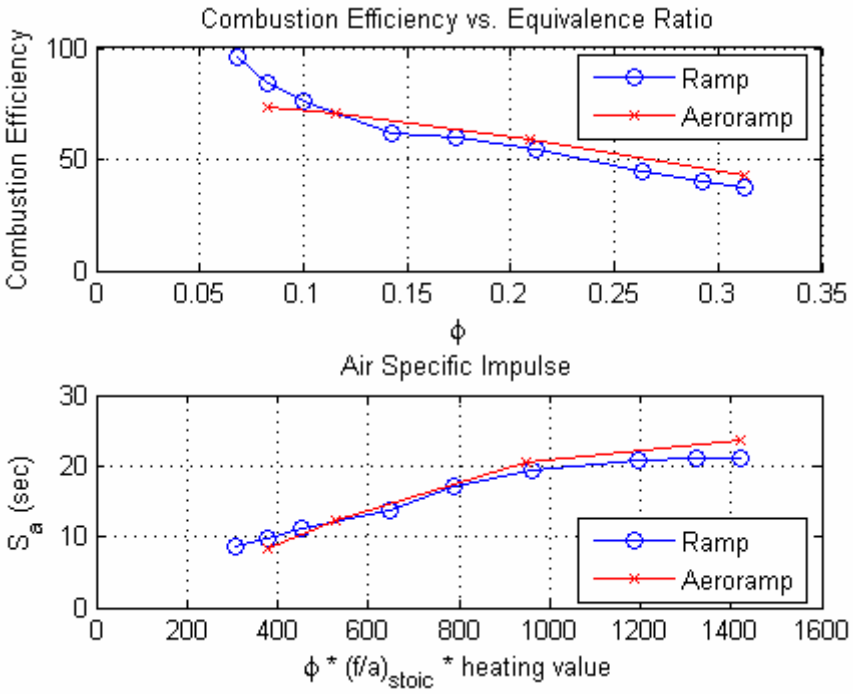

Figure 4.9. Combustion efficiency and air specific impulse curves for hydrogen injected through the aeroramp and the physical ramp injectors.

4.3.2. Ethylene vs. Hydrogen Fuels

Figure 4.10 compares the same performance parameters for hydrogen and ethylene fuels, for injection via the aeroramp at air total temperature of $T_o = 1000K$. For the

overlapping range of equivalence ratios, the two fuels produce the same combustion efficiencies and very similar air-specific impulses. The decreasing trend in combustion efficiency with increasing equivalence ratio is observed for ethylene as well. Recalling that for ethylene $\varphi_{trans} = 0.32$, the ethylene fuel is more inefficient than hydrogen. For the supersonic combustion cases the average efficiency has dropped to $\eta_{sup} \approx 62\%$, whereas for the dual-mode case the efficiency drops even more to $\eta_{sub} = 40\%$. This result is reasonable, if one considers the reactivity of the two fuels. The reaction rate of ethylene is much less than that of hydrogen, so even if more fuel is present in the mixture, it is less likely to ignite/combust.

Considering the air specific impulse results, the observed trend is for increasing impulse with increased φ. As φ is increased, the engine transitions from the scramjet mode to the dual-mode ramjet. However, at the equivalent flight conditions, the ramjet is a more efficient cycle and yields more thrust, so the increase in air-specific impulse is expected.

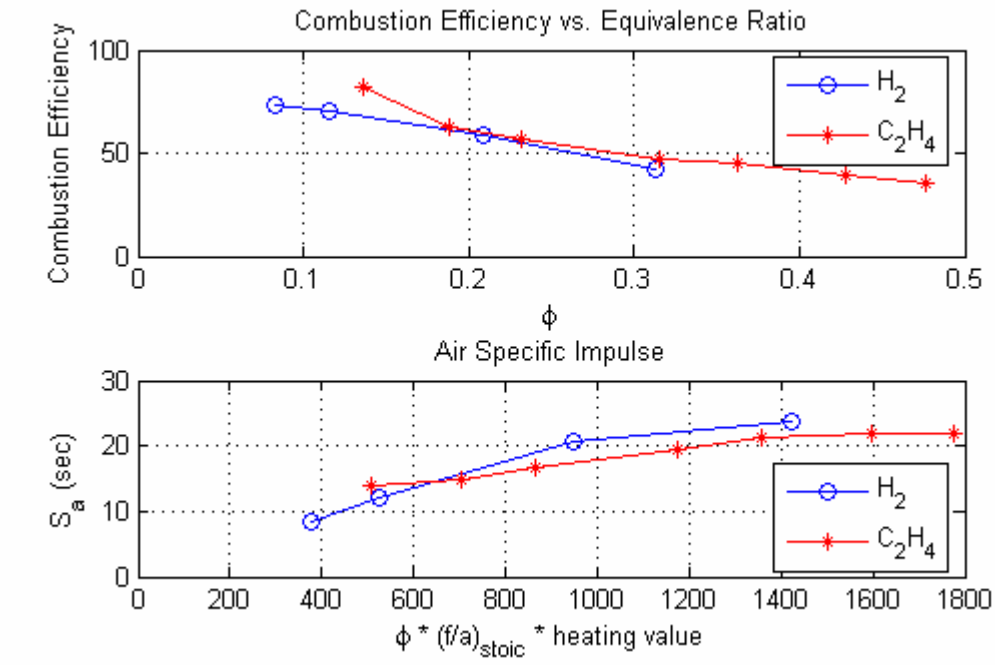

Figure 4.10. Combustion efficiency and air specific impulse results for different fuels.

4.3.3. Air Total Temperature Variation with Hydrogen Fuel and the Aeroramp Injector

In order to make correct predictions for the different air total temperature conditions with RJPA, the freestream ("inlet" module) conditions need to be altered, to represent the experimental conditions. That is to say, the reduction in the total temperature directly leads to a reduction of the supersonic inlet capture area and altitude. This, in turn, affects the flight

Mach number, which needs to be reduced since the combustor-to-inlet contraction ratio is not as large. Table 4-4 summarizes the freestream conditions that need to be altered in RJPA to account for the change in air total temperature.

To	[K]	1010	820	610	530
M	--	4.22	3.67	3.01	2.67
h	[ft]	88000	73000	53300	43100
Inlet Area	[in^2]	9.65	6.1	3.38	2.5
Area Ratio	--	6.43	4.07	2.25	1.67

Table 4-4. RJPA freestream conditions for each total temperature tested.

Results from the air total temperature variation study with hydrogen fuel are presented in Figure 4.11. Overall, a decrease in efficiency and specific impulse is observed as total temperature decreases.

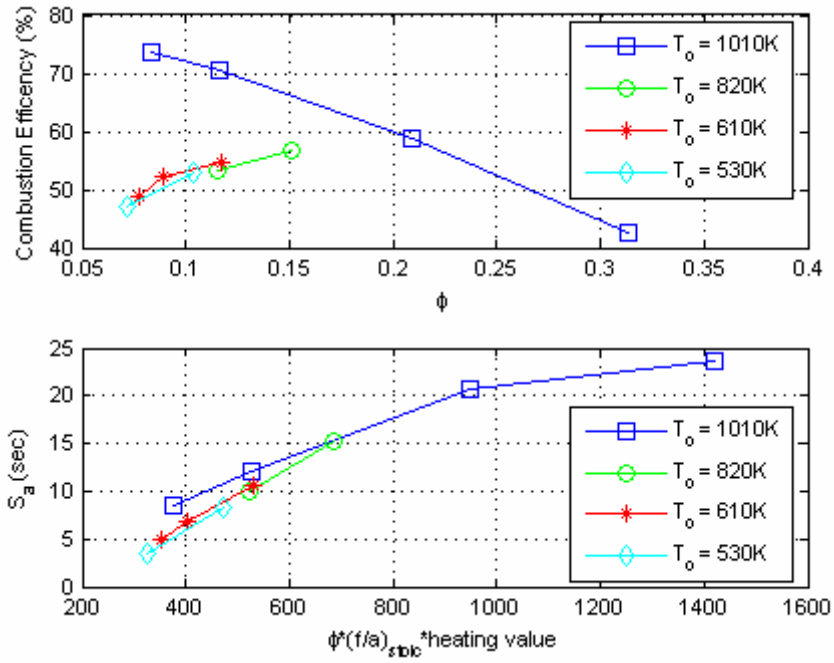

Figure 4.11. Combustion efficiency and air specific impulse for hydrogen fuel injected through the aeroramp at various air total temperatures.

An interesting fact arises when considering the combustion efficiencies. For the baseline case of T_o = 1010 K, efficiency decreases with increasing φ, however, an opposite trend is observed for the lower air temperature cases. Indeed, at the lower T_o, the dual-mode combustion cases (φ > 0.1) have higher efficiencies than the supersonic combustion cases. At the lower total temperatures, the chemical reaction rate decreases, as governed by Arrhenius' reaction rate law [Glassman, 1996]:

$$k = A\exp\{-E_a / RT\} \tag{4.8}$$

where T is static temperature, E_a is the activation energy, R is the universal gas constant and A is a constant. In the dual-mode region, the combustor velocities are substantially lower than in the supersonic combustion cases, allowing more residence time for the fuel. Even with a lower reaction rate at lower temperatures, more fuel can be combusted due to the increased residence times, yielding an increase in efficiency as φ increases.

4.3.4. Air Total Temperature Variation with Ethylene Fuel

Results from the air total temperature variation study with ethylene fuel are presented in Figure 4.12. Overall, a decrease in efficiency and specific impulse is observed as air total temperature decreases. Combustion efficiency decreases with increasing equivalence ratio, whereas the air specific impulse increases with φ.

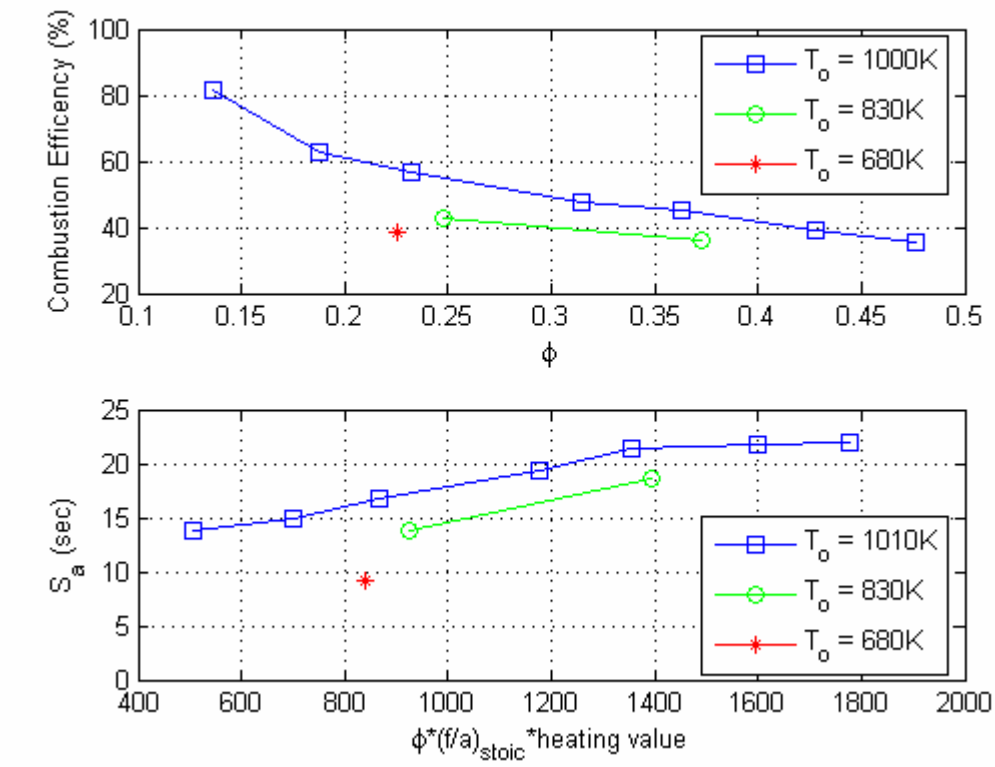

Figure 4.12. Combustion efficiency and air specific impulse for ethylene fuel injected through the aeroramp at various air total temperatures.

4.3.5. Fuel-specific Impulse Results and Thrust-specific Fuel Consumption

From the thrust predicted by assuming a "theoretical" diffuser and nozzle for the engine, fuel specific impulses (I_{sp}) can be calculated. Table 4-5 summarizes the calculated values of I_{sp}, in seconds, for hydrogen and ethylene fuels for the T_o = 1000 K case. For hydrogen, specific impulses on the order of 3000 sec are obtained, which fall in the theoretically predicted limits for scramjet flight at $M_\infty = 4$, as shown in Figure 4.13 [Moses, 2003]. For ethylene, lower specific impulses, on the order of 1000 seconds, are obtained. Again, this is a typical result for hydrocarbon fuels.

To = 1000K	*Hydrogen (H_2)*		*Ethylene (C_2H_4)*	
	φ	I_{sp} (sec)	φ	I_{sp} (sec)
	0.083	4013	0.136	1320
	0.143	3246	0.232	946
	0.212	3260	0.363	785
	0.313	2428	0.476	620

Table 4-5. Summary of Isp for hydrogen and ethylene for selected equivalence ratios.

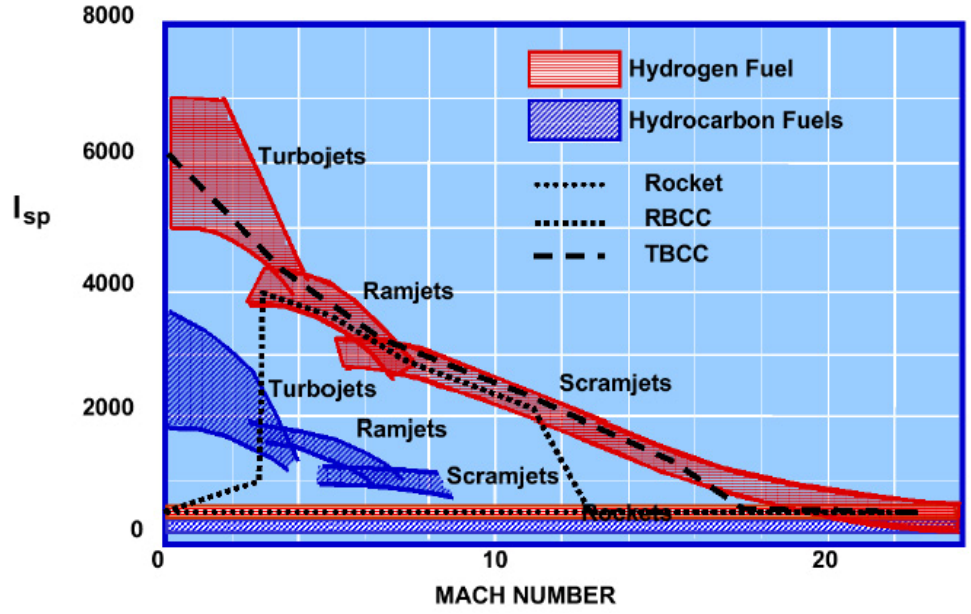

Figure 4.13. Theoretical Isp's for various propulsion types with hydrogen and hydrocarbon fuels, over a range of flight Mach numbers [Moses, 2003].

A performance number commonly reported for airbreathing engines is the inverse of the fuel-specific impulse, the thrust-specific fuel consumption (TSFC). TSFC results for a

scramjet are compared to average experimental results for turbofans, turbojets and ramjets (with hydrocarbon fuels) [Hill, 1992]. A larger TSFC corresponds to a more inefficient engine. The trend of doubling TSFC with each system is followed

	Kg/N·hr	$lb/lb_f \cdot hr$
Scramjets (H_2)	0.084 - 0.15	0.84 - 1.5
Scramjets (C_2H_4)	0.27 - 0.58	2.7 - 5.8
Ramjets	0.17 - 0.26	1.7 - 2.6
Turbojets	0.075 - 0.11	0.75 - 1.1
Turbofans	0.03 - 0.05	0.3 - 0.5

Table 4-6. TSFC for various propulsion systems

The results reported in Hill's text are based on hydrocarbon fuels, and he states that "TSFC of a given engine depends strongly on flight speed", i.e., for each engine type the TSFC remains fairly constant. Figure 4.14 presents the TSFC for four different hydrocarbon fueled engine types, turbofans, turbojets, ramjets and scramjets. The scramjet data is from the current study and appears to follow reasonably the trends set by the first three engine types, i.e., increase both in the value of the TSFC and the range.

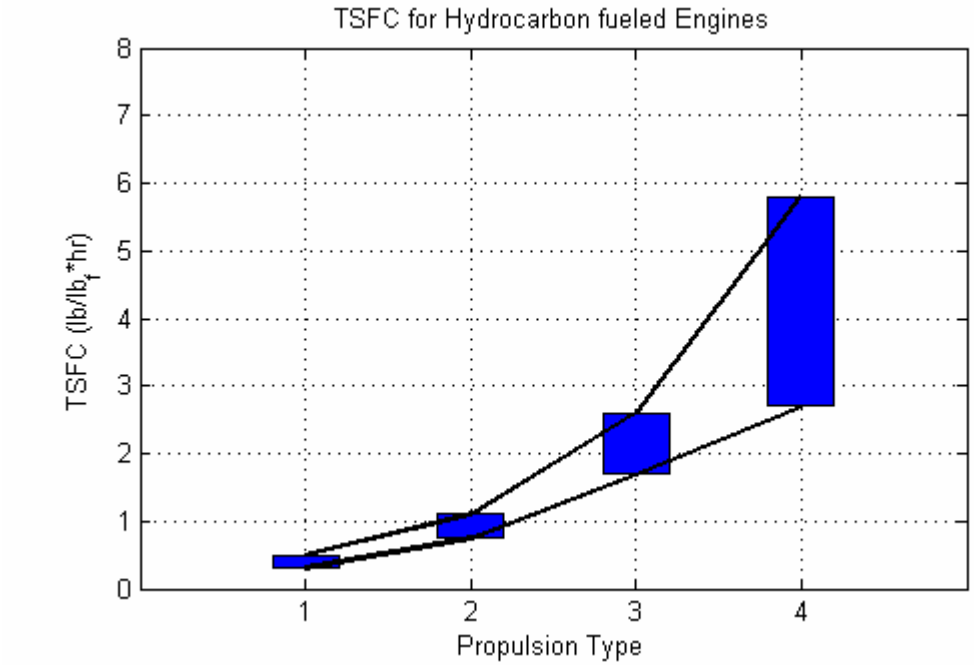

Figure 4.14. TSFC for various propulsion types with hydrocarbon fuels: (1) turbofans, (2) turbojets, (3) ramjets and (4) scramjets. Data for the scramjets is from the current study.

4.4. Uncertainty Analysis

The question of how sensitive the RJPA results are to the experimental uncertainties is a reasonable one. More specifically, the measured wall pressures, which are a key input to RJPA, are known within ±2%, so how does this affect the results?

To answer this question, the base case of ethylene fuel (i.e., T_o = 1000 K) was analyzed with a ±2% difference in the combustor exit pressure (PCE). As shown in Figure 4.15, combustion efficiency errors are less than 3% and decrease with increasing equivalence ratio, whereas the air specific impulse errors are less than 4%. This allows us to have fairly good confidence in the RJPA results.

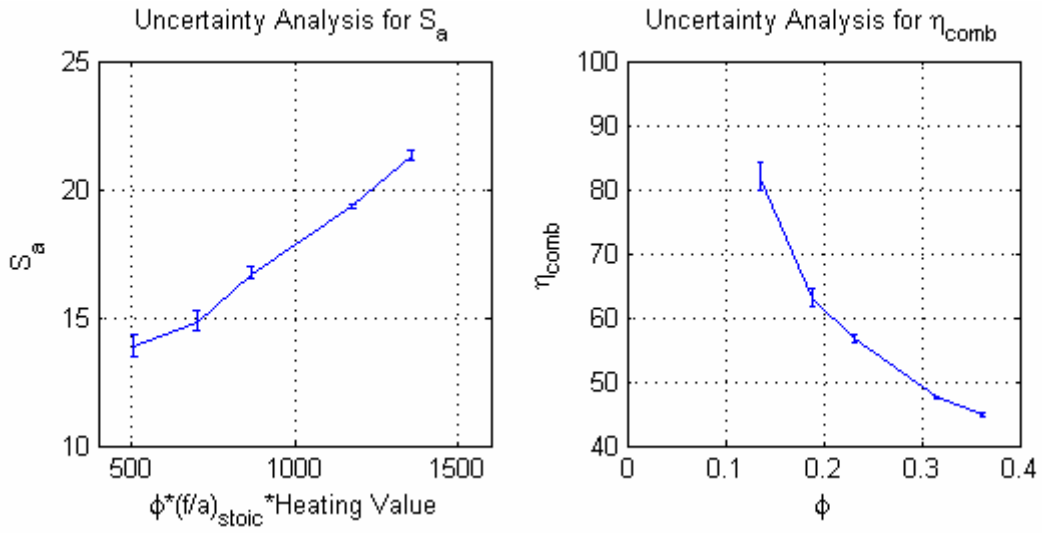

Figure 4.15. Uncertainty analysis of RJPA data. Uncertainty in predicted air specific impulse (left) and combustion efficiency (right) based on ±2% experimental uncertainty in pressure.

4.5. Conclusions

Data from direct connect testing of an integrated aeroramp injector/plasma torch igniter were analyzed using the RamJet Performance Analysis code (RJPA). This allows for combustion efficiency and specific impulses to be deduced from wall static pressure distributions. For this study, a theoretical diffuser and nozzle were assumed to perform a complete engine analysis. The conclusions of this study can be summarized as follows:

- For hydrogen fuel at the base case condition of T_o = 1000 K, combustion efficiencies in the supersonic combustion mode were on average 81%, and this was reduced to 51% in the dual-mode combustion.

- For ethylene fuel at the base case condition of T_o = 1000 K, combustion efficiencies were on average 62% and 40% for the supersonic and subsonic combustion cases, respectively.
- For hydrogen fuel, the combustion efficiency and specific impulse results are very similar for the two injection systems (aeroramp and physical ramp). The aeroramp performs slightly better, however the differences are very small (< 5%) and are probably within the uncertainties for the two experiments.
- The engine performs similarly independent of fuel, as determined by the air-specific impulse results. Air specific impulses are between 10 and 25 seconds, varying with equivalence ratio.
- For hydrogen fuel at the base case of T_o = 1000 K, the trend is for combustion efficiency to decrease with increasing φ. For the other air total temperature cases this trend is reversed. This is due to the reduced reaction rates at the lower temperatures.
- Fuel specific impulses fall within the theoretically predicted values for scramjets at the given flight Mach number, namely 3000 seconds for hydrogen and 1000 seconds for ethylene.

C h a p t e r 5

5. Numerical Investigation of Aeroramp Mixing in a Supersonic Cross-Flow

5.1. Introduction

The use of the aeroramp injector with different fuels dictates the need for a predictive method to guide the injector/igniter integration. Computational Fluid Dynamics (CFD) provides an excellent tool for this type of analysis. The experimental conditions simulated were those of the experiments reported earlier in this dissertation (Chapter 2).

CFD calculations were made using GASP® (General Aerodynamic Simulation Program from AeroSoft, Inc. RANS code). The analysis yielded a complete determination of the flow field created by the aeroramp, as the injected fuel is mixed with the freestream air and convected downstream. Wall static pressure was used as validation, since this data was available from the experimental tests. GASP® was chosen due to its suitability for high-speed flow problems. Several validation/verification reports exist in the literature, such as the turbulence modeling validation of Neel et al. [2003], general validation of supersonic aerodynamics of Loomis et al. [1997], multiple jet interaction in supersonic flows validation by Viti et al. [2002] and the supersonic reacting flow validation of Goyne et al. [2001].

The main results are the fuel distribution, in the form of mass fraction concentration, α, at selected stations downstream of the injector center. By inspection of the local fuel and pressure contours, a region of favorable equivalence ratio can be selected for placement of the plasma torch to maximize ignition probability and combustion efficiency. Since only three discreet stations for the placement of the torch are experimentally available (at 6, 8 and 10 d_{eq} downstream of the injector) the concentrations at each of these stations is examined, and the best one is proposed for use.

5.2. Experimental Conditions Simulated

The experimental conditions modeled were those of the Supersonic Combustion Tunnel of the University of Virginia. The inflow conditions consisted of un-vitiated air

flowing at Mach 2, with a total pressure of P_o = 330 kPa and a total temperature T_o = 1000 K. At these conditions the flow velocity is 990 m/s. A complete summary of the tunnel operating conditions was given in Table 2-1. The simulations did not include an initial boundary layer, since no experimental measurements are available. Instead, a boundary layer was allowed to grow in the simulations over a length of 5 d_{eq} upstream of the injector. The fuel total pressure and temperature used in the simulations are listed in Table 5-1 for each fuel considered. The domain modeled extended from x/d_{eq} = -5 to 56. The simulated fuel mass flow rate was controlled by the fuel total pressure, and was selected based on experimental conditions.

Fuel	Po (kPa)	φ
Hydrogen	303	0.105
Ethylene	212	0.136
Methane	195	0.252

Table 5-1. Fuel conditions used in the simulations. Table presents the fuel total pressure and the corresponding equivalence ratio.

5.3. Computational Methodology

GASP®, a finite volume code capable of solving the complete integral form of the time-dependent, Reynolds-Averaged Navier-Stokes (RANS) equations in three dimensions, was used. The code is of the upwind type and solves the equations on a structured grid. Finite rate reacting flows can be simulated as well. In this case, only the fuel-air mixing was considered (frozen chemistry), and the process was assumed to be steady.

A solution was considered to be converged when one of the following occurred (in order of preference):

- The monitored value at a check node reached a constant level (variations less than 1%),
- The residual decreased by at least five orders of magnitude, or
- Wall static pressures exported from the simulations matched the experimental data.

5.4. Grid Generation

Several grids were generated to simulate the overall problem of injection through a single flush wall injector or an injector array into a supersonic cross-flow. The GRIDGEN® code (v. 15.4) was used for this purpose. GRIDGEN® is a graphical, interactive grid-generating program used for producing structured meshes for CFD solvers such as GASP®. The computational domain consisted of blocks, each block representing a grid volume. The

blocks were designed so as to increase the grid point density near points of interest, i.e. near the injectors, where shocks were expected and near solid surfaces for better boundary layer resolution. This technique optimizes the number of nodes used and helps keep computational time to a minimum.

For each grid developed, the symmetry of the setup was invoked, and only "half" the combustor was modeled, i.e. $0 \leq y/d_{eq} \leq 6$. The physical space modeled began at $x/d_{eq} = -5$, i.e. upstream of the aeroramp injector and extended to $x/d_{eq} = 56$, i.e. the full constant area length of the combustor and approximately half of the length of the section with the 2.9 degree divergence. The full height of the combustor was modeled up to the solid wall surfaces at $z/d_{eq} = 8$ for the constant area section. At the end of the divergence, the total height was $z/d_{eq} = 9.9$. The start and end of the combustor were chosen at locations where a pressure tap existed, so combustor inlet and exit pressure where known. Also, the end was chosen far enough downstream for the mixing to be fairly complete, but not too close to the physical exit so the atmospheric exhaust did not need to be taken into account.

The generated grids include provision for the plasma torch. Along the centerline of the injector surface and at $x/d_{eq} = 10$, a circular jet normal to the injection surface was placed, with a diameter of 0.5 d_{eq}. This, coupled with appropriate boundary conditions, allows for prediction of the mixing process incorporating the plume of the plasma torch, or if a reacting chemistry model is used, the combustion process can be simulated.

5.4.1. Single-Hole Grid

Past experiments have shown that far enough downstream of the injector, the flow-field created by the aeroramp is crudely similar to that of a single, transversely angled, circular jet [Jacobsen, 2003]. Due to this fact, and the simpler geometry of a single-hole injector vs. an aeroramp, the first grid created was that of a single, circular jet at 30 degrees with respect to the freestream (pitch). The diameter of the single jet, by definition, was 1 d_{eq}, or 3.175 mm. An isometric view of the computational domain is shown in Figure 5.1.

The single-hole injector grid contained 1.3 million cells (1,325,688) distributed into 29 zones (see Figure 5.1). This grid size is thought to be sufficient to provide enough detail to analyze the flow features of interest, while allowing the computations to converge in a reasonable amount of time. An H-grid is used in the inflow plane with clustering around the solid wall surfaces. The jet zone curves downstream to follow the expected fuel plume and is merged with the plasma torch plume. At the point of divergence of the channel, the grid is

designed to be fairly orthogonal and is extrapolated out to the exit plane. The grid was not extended to model into the jets.

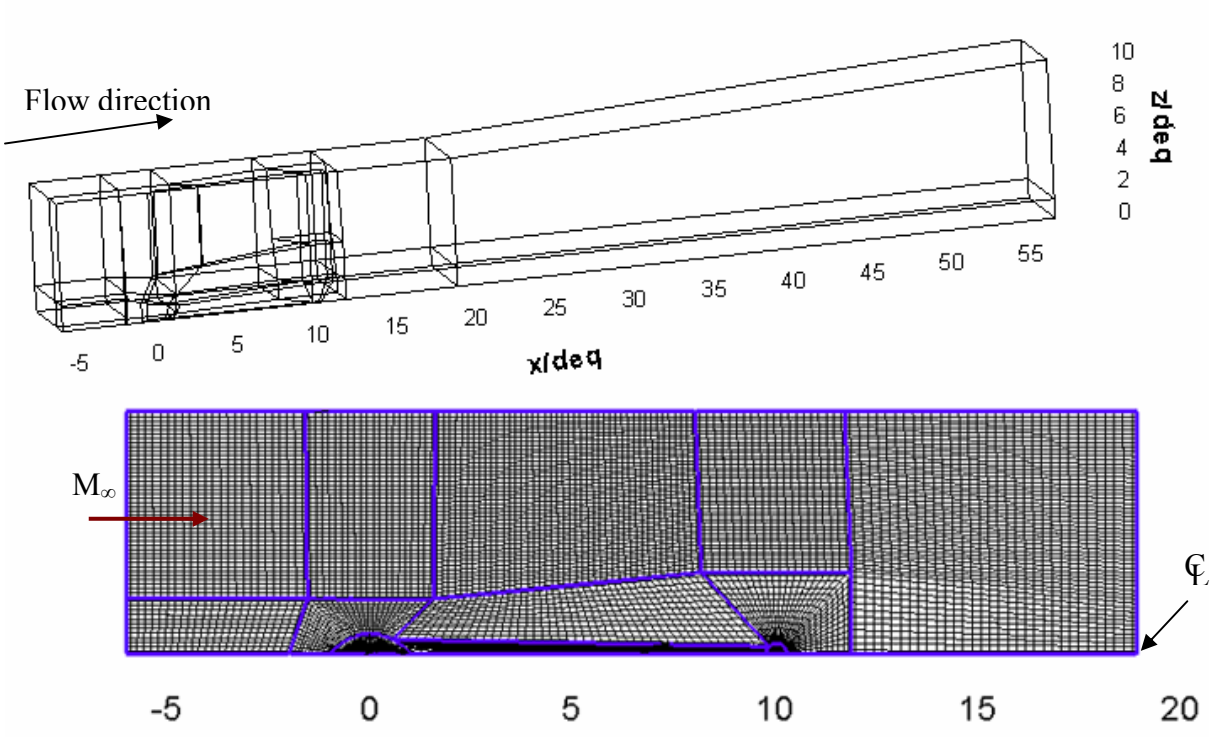

Figure 5.1. Single-hole injector grid. Top illustrates the full computational domain with the zones and bottom shows the injection wall surface. Plasma torch orifice is at $x/d_{eq} = 10$.

5.4.2. Aeroramp Grid

Once enough experience in grid generation was gained by designing the single-hole injector grid, an aeroramp grid was created. Again, the symmetry of the physical setup was employed, so only two of the jets in the four-jet array were modeled. Due to the complexity of the geometry, a simple Cartesian grid was developed by extrapolating from the injection surface up, as shown in Figure 5.2. The grid had 1.6 million cells (1,622,544). The additional cells, compared to the single-hole grid, are justified by the increased complexity of the aeroramp geometry. Again, no grid modeling into the jets was done due to the complex geometry.

There is an additional benefit to creating Cartesian grids. Using skewed sells causes problems with the numerical solvers and increases the possibility of getting grid-related artifacts in the solution. With Cartesian grids the number of skewed cells is minimized, since the cells have a fixed height. The skewness of the cells is calculated by GRIDGEN® by computing the Jacobian for each cell. If this is out of a certain range about the mean, the cell is considered skewed, and it is recommended that the grid be redesigned.

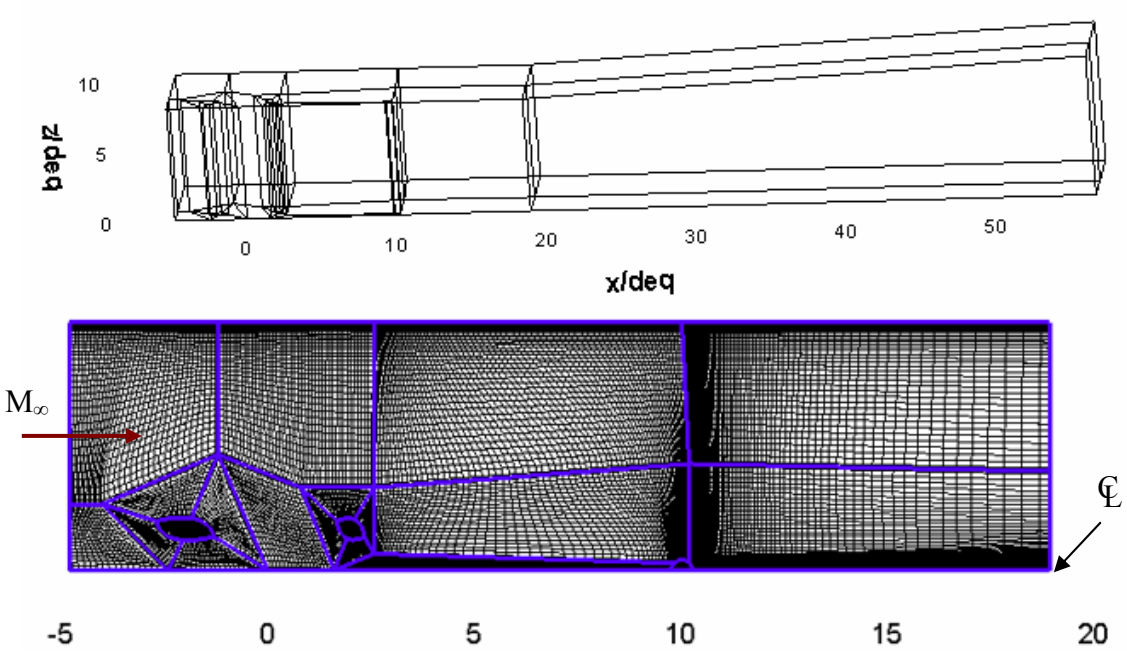

Figure 5.2. **Aeroramp grid. Top illustrates the full computational domain, bottom shows the injection wall surface that was extrapolated to yield the grid.**

5.5. Physical Models

5.5.1. Boundary Conditions

The grid modeled the setup of the Supersonic Combustion Tunnel of the University of Virginia. The physical walls were modeled with the "no slip, adiabatic" boundary condition. The three walls are located on the $z/d_{eq} = 0$, $z/d_{eq} = 8$ and $y/d_{eq} = 6$ planes. Since this is a continuous flow facility, it is reasonable to assume that the insulated walls reach a steady state temperature, so they can be modeled as adiabatic. The effect of the internal wall cooling present in the facility would not be realized since only mixing cases are simulated.

A "symmetry plane" condition was imposed on the $y/d_{eq} = 0$ plane, taking advantage of the symmetry of the physical setup.

The inflow conditions ($x/d_{eq} = -5$) were defined with the "Fixed at Q (not turbulence)" boundary condition. The freestream Q vector was specified as air (20% O_2, 80% N_2 by mass) flowing at Mach 2, at T = 555.56 K, P = 40.2 kPa and $\rho = 0.25$ kg/m^3 with corresponding total conditions of $T_o = 1000$ K and $P_o = 315$ kPa, resulting in a velocity of 950 m/s in the x-direction (slight difference from experimental conditions due to 4% difference in total pressure). Turbulence quantities were left to the default values (Turbulence Intensity = 0.05). The Reynolds number was $8.3e^6$ per meter.

The outflow conditions, at the $x/d_{eq} = 56$ plane, were simply extrapolated with a 1st-order approximation.

In calculations where the plasma torch was used, the "Fixed at Q (not turbulence)" B.C. was used at the torch exit. The following quantities were specified in the plasma torch Q vector. A sonic nitrogen jet (Mach = 1) with T = 900 K (arbitrarily selected), P = 0.1 MPa and $\rho = 0.4$ kg/m^3, with corresponding total conditions $T_o = 1080$ K and $P_o = 0.2$ MPa, resulting in a velocity of 610 m/s in the z-direction.

The fuel-jet also used the "Fixed at Q (not turbulence)" condition. The values used for the fuel Q vector are specified in Table 5-2. The velocity vector for the flow angle of each jet depends on the injection system and is different for the aeroramp and the single-hole injector. A summary of the normalized vectors for each injector is presented in Table 5-3. Note that for the aeroramp injector, the 20-degree jet is the upstream one and the 40-degree jet is downstream.

Quantity	[units]	Hydrogen	Ethylene	Methane
P	[kPa]	160.0	111.1	105.4
P_o	[kPa]	302.8	205.8	195.2
T	[K]	250	250	250
T_o	[K]	300	292	292
ρ	[kg/m^3]	0.29	1.8	0.81
Mach	[-]	1	1	1
V	m/s	1205	314	415

Table 5-2. Summary of Q specification vector values for fuel.

	single-hole	aeroramp	
	30 deg.	20 deg.	40 deg.
x	0.866	0.907	0.663
y	0	-0.246	-0.383
z	0.500	0.342	0.643

Table 5-3. Flow angles for the aeroramp and single-hole injectors

5.5.2. Inviscid Fluxes

The Roe flux vector-splitting scheme was used in all three coordinate directions. It was chosen because of its robustness and accuracy [AeroSoft, 2004]. It is less dissipative than Van Leer's scheme and thus more suitable for boundary layer type flows. Furthermore, Roe's scheme is based on characteristic wave disturbances and so, by design, can capture stationary discontinuities, such as the shocks prior to each injector port (single-hole, aeroramp or plasma torch).

The spatial accuracy was set to 3rd-order with an upstream bias, resulting in a value of $\kappa = 1/3$ in the MUSCL formulation.

The Min-Mod limiter was used in these calculations. Limiters control the monotonicity of the solution, in order to achieve the desired balance between convergence and accuracy. They are needed when discontinuities exist in the flow to obtain valid, well-behaved solutions.

5.5.3. Viscous Fluxes

The viscous fluxes were set to the turbulent mode in order to capture the true nature of the flow. Thin-layer terms were modeled in all I, J and K directions, but no cross-derivative terms were computed. The wall-gradient calculations were set to 2nd-order accuracy. For the laminar properties, the Sutherland viscosity and conductivity models were used with (laminar) Prandtl and Schmidt numbers of 0.72 and 0.7 respectively.

Wilcox's 1998 two-equation k-ω turbulence model was employed. This model has been successfully used in similar flow conditions [Viti, 2002] and is suitable for boundary layer flows with adverse pressure gradients. Viscosity limiting was used (< 2000 x viscosity) to accelerate convergence. Turbulent Prandtl and Schmidt numbers used were 0.9 and 0.5 respectively.

5.6. Grid Convergence Study

In any CFD study it is important to distinguish how the grid affects the obtained solution. How prevalent is the discretization error and does it overwhelm the solution, or can sequenced grids be used to obtain a solution with similar accuracy in less computational time. In other words, is the number of grid points used adequate and optimized?

To answer these questions, a grid convergence study was performed. The aeroramp grid of section 5.4.2 was considered with ethylene fuel. Three sequencing levels were run, coarse, medium and fine grids with $2.1e^4$, $2.0e^5$ and $1.6e^6$ cells respectively. In each case the solution was initialized from the same initial conditions, and flow properties were monitored. Both local (pressure, skin friction coefficient, mass fraction at a point) and global (normalized residual) solution properties were monitored.

Figure 5.3 presents the results of the grid-convergence study. The plot on the lower right hand side of Figure 5.3 shows the convergence of the normalized residual. At each grid point, a vector, say $\vec{Q}_n$, containing the values of flow variables exists, which is updated after each computational cycle (n). The normalized residual is defined as follows:

$$\frac{\bar{Q}_n - \bar{Q}_{n-1}}{\bar{Q}_1} \tag{5.1}$$

So, by monitoring this value a good indication of convergence can be obtained. However, considering this property alone, the solution would be considered converged after 500 iterations, even on the finest grid, since no apparent benefit is obtained from further computational cycles, i.e., the residual does not decrease further. For this reason, local flow properties need to be monitored as well.

The remaining three plots in Figure 5.3 show the convergence of static pressure, mass fraction of ethylene and skin-friction coefficient at a given check-point in the flow. Recall that all solutions were initialized from the same conditions and allowed to develop. The pressures for the medium and fine grids converge to the same value after 2000 iterations, past which they remain constant. The concentration and skin-friction coefficient results do not converge to the same value. However, the final results for both variables on the medium and fine grids are within 13%. Based on these results, the solution can be considered converged even at the medium grid.

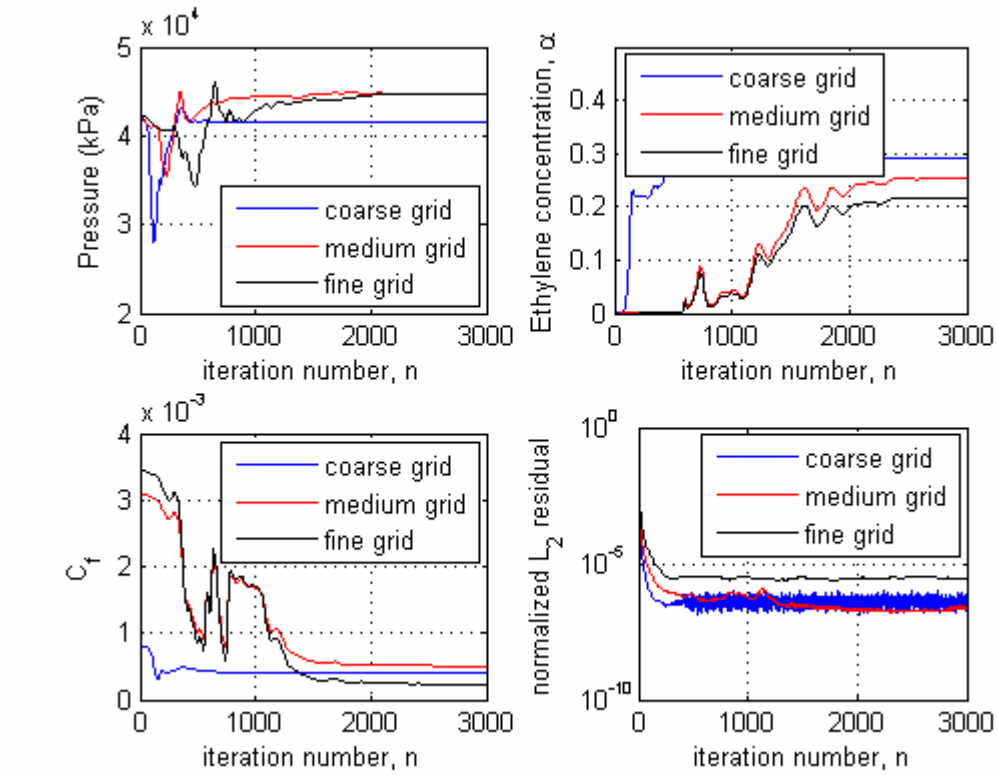

Figure 5.3. Grid independence/convergence study for the coarse, medium and fine mesh sequences. Presented are wall static pressure (kPa - top left), mass fraction (top right), skin friction coefficient (lower left) and residual (lower right).

5.7. Results and Discussion

5.7.1. Single-Hole Injector Case

Initially, the calculations were performed on the single-hole grid with ethylene as the fuel. The reason for using only ethylene in the computation is that this is the primary fuel of interest and also because the single-hole injector is not the injector of main concern. Furthermore, in the interest of time, the plasma torch jet was not included in these computations either.

5.7.1.1. Pressure Contours

The first result considered from this simulation is the pressure field generated by the injector. The wall-static pressure computed along the tunnel centerline and on the wall opposite the injector wall is compared to data from the experiment. The experimental condition used is for ethylene injection via the aeroramp with the torch feedstock on in the heated flow facility.

This comparison is presented in Figure 5.4. The computations seem to capture the initial pressure rise caused by the shock off the injector. Downstream of the 2.9-deg expansion (at 20 d_{eq}), a lower pressure is initially predicted; however, the difference is less than 10%. This difference disappears at the point where the reflected shock hits the top wall (at $x/d_{eq} = 35$), and the pressures in the nozzle are in good agreement. The pressure contours along the symmetry plane are presented in Figure 5.5, and help visualize the process previously described.

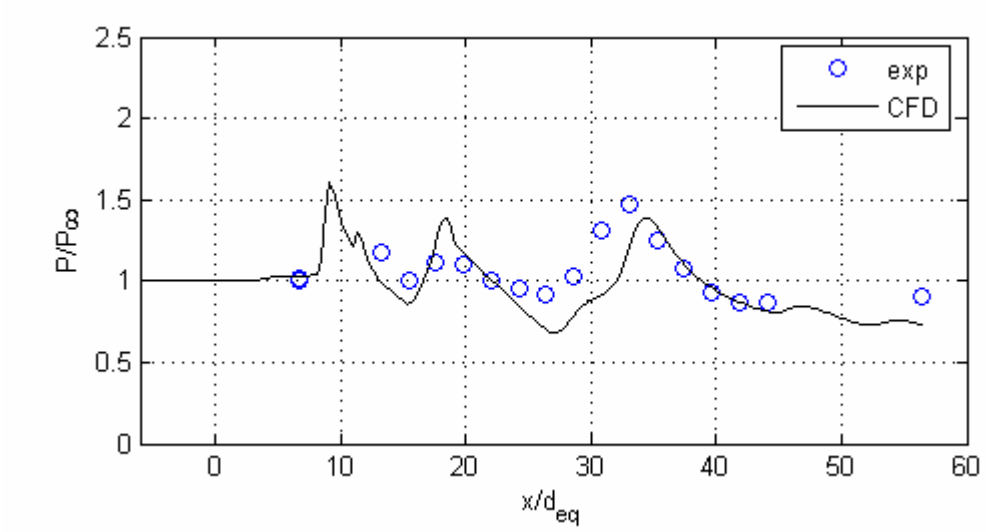

Figure 5.4. Measured and computed pressure profiles. CFD is for injection of ethylene through a single-hole circular injector.

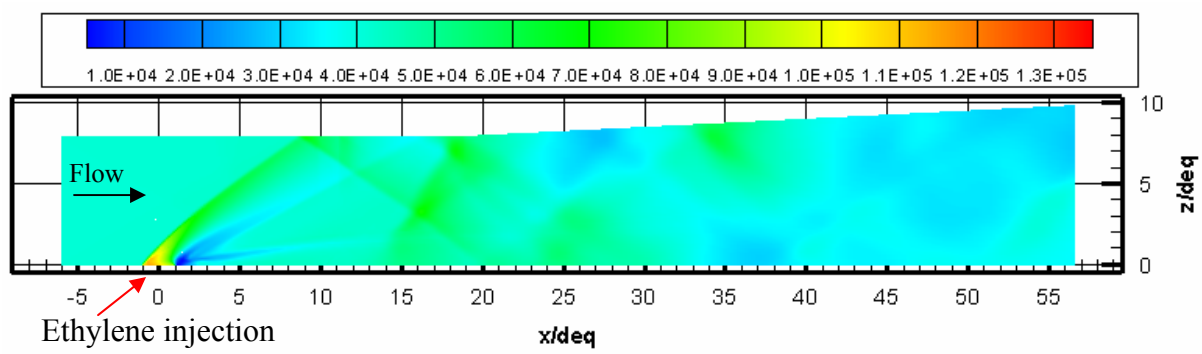

Figure 5.5. Predicted pressure contours along symmetry plane (Pressures in kPa). CFD is for injection of ethylene through a single-hole circular injector at 30-degrees.

The reasonably good agreement between the experimental and numerically predicted profiles serves as a simple validation for the code and proof that no grid-created artifacts are present.

5.7.1.2. Mass Fraction Contours

The mass fraction contours for the mixing of ethylene injected via a single-hole injector at 30-degrees are presented in Figure 5.6. The contours on three stations are presented; these are the stations at which the torch can be placed and are 6, 8 and 10 d_{eq} downstream of the injector center. The $x/d_{eq} = 6$ plane shows the full computational domain, whereas only the region around the jet is shown for the other planes. The fuel penetration obtained at this station is about 2 d_{eq}, which corresponds to 25% of the duct height.

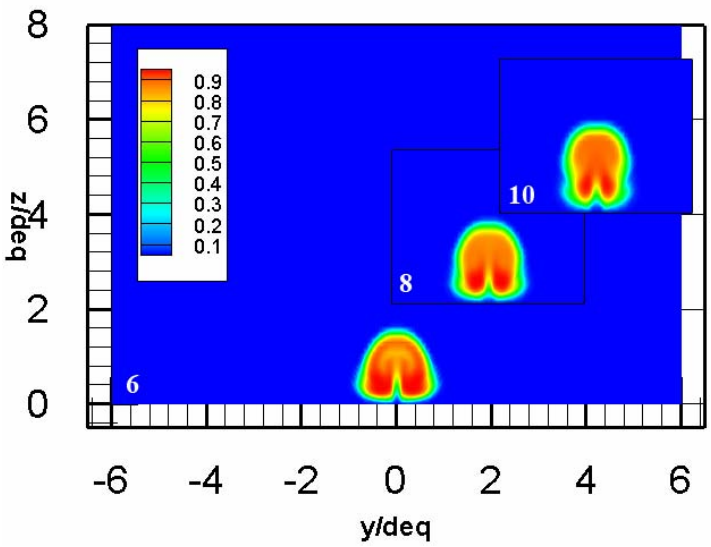

Figure 5.6. Predicted mass fraction contours of Ethylene injected via single-hole injector at x/d_{eq} = 6,8 and 10.

From examining the mass fraction contours, the vortex structure generated from the jet-freestream interaction can be seen. This structure is comprised of a counter-rotating set of vortices emanating from the area in front of the injector and spilling around the sides of the main jet. This causes air to be trapped in the center of the jet near the injection wall, and as we proceed downstream this air pocket moves up into the main core causing additional mixing. Figure 5.7 shows the plume mixing at several downstream stations (shown are stations 2.5 d_{eq} apart between 0 and 35 d_{eq}).

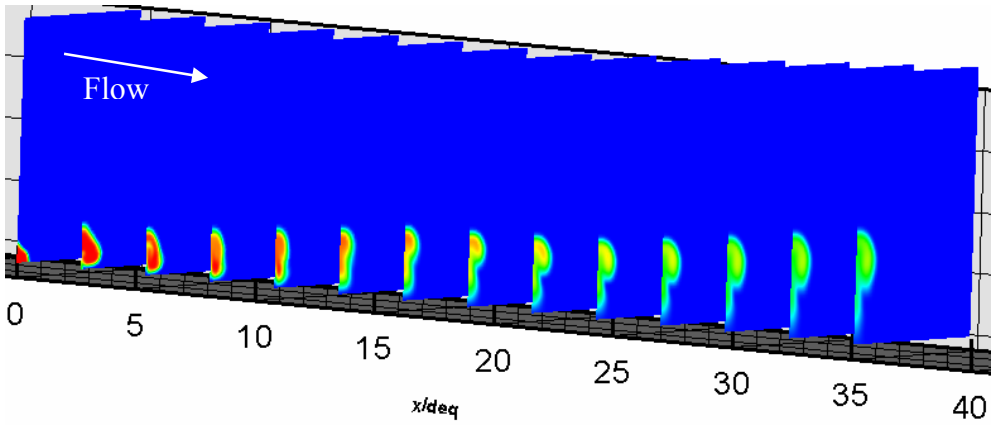

Figure 5.7. Predicted mass fraction contours of ethylene injected through a single-hole on several downstream stations between x/d_{eq} = 0 and 35 (each plane is 2.5 d_{eq} apart).

Consider a representative small ½ x ½ d_{eq}^2 area at the location of the torch (x/d_{eq} = 10). The plasma torch exhaust products would first come into contact with the air/fuel mixture in this region, and so this is where ignition will occur. Selecting an appropriate length scale for a prediction of ignition is a challenge; too small a region will be insufficient to include the physical dimension of the arc and too large a region will give results that approach the global equivalence ratio. The final length scale was selected based on intuition and the aid of pictures of the plasma torch in operation, shown in Figure 5.8. Figure 5.8 (a) shows the plasma torch in operation at typical experimental conditions, in order to obtain an estimate of the plume size. The problem with a direct picture of the torch plume is that it will saturate any CCD or film due to its brightness. The arc region is in fact a lot smaller. Figure 5.8 (b) is presented for the relative length of the anode to be infered. Figure 5.8 (c) is a superposition of images (a) and (b), showing both the anode and the plume area. The integration area is the region within the red box shown.

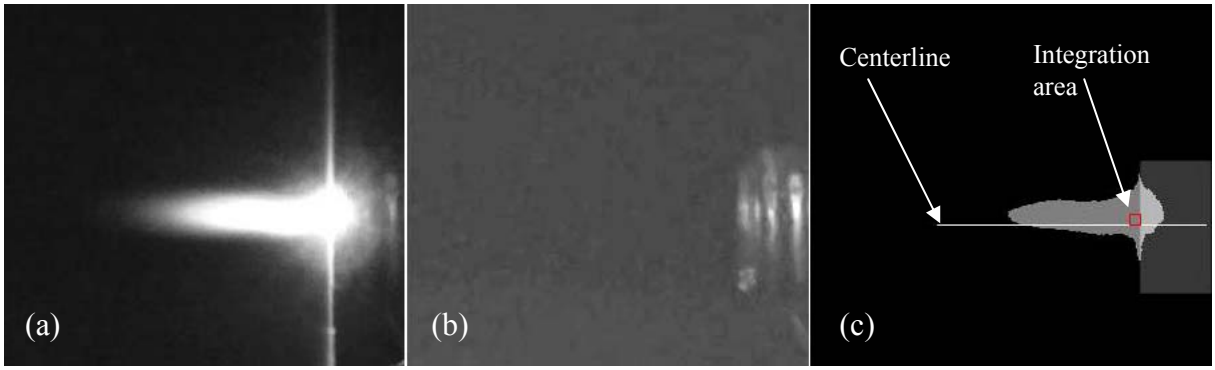

Figure 5.8 (a) The plasma torch operating in a quiescent environment at typical test conditions, (b) a picture of the anode for reference length purposes and (c) the processed image of the torch plume with respect to the anode, indicating the integration area selected in a red box.

Such an area is shown in Figure 5.9. A closer inspection yields a high average concentration ($\alpha \approx 0.44$, corresponding to a fuel-to-air ratio of 0.76) and an almost constant pressure of 36 kPa. Given that the stoichiometric ratio for ethylene is 0.067, the averaged local equivalence ratio in this area is about 11.3. This region seems to be too fuel rich to favor for ignition. Figure 5.10 shows the inflammability limits for gasoline-air mixtures [Olson, 1950]; however most hydrocarbon-air mixtures exhibit similar behavior, so conclusions for ethylene and methane can be drawn as well. From an extrapolation of this curve, the region with the specified pressure and concentration lies outside the region of possible ignition. So, if a single-hole circular injector were to be used, the plasma torch would need to be placed a lot further downstream to allow for adequate mixing to occur.

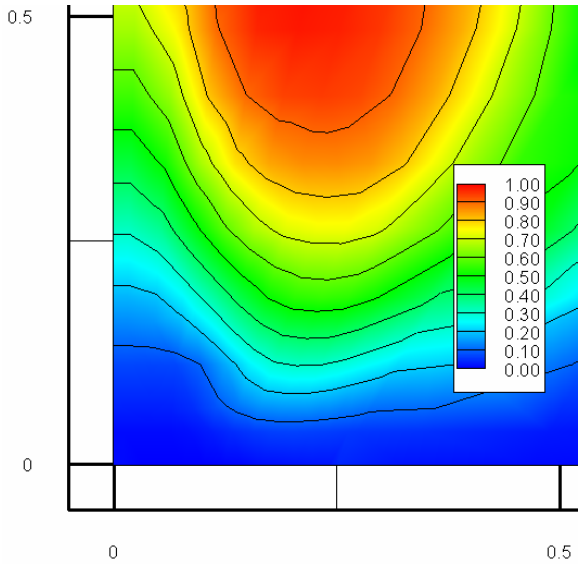

Figure 5.9. Close-up of plume of single-hole injector at x/d_{eq} = 10 station

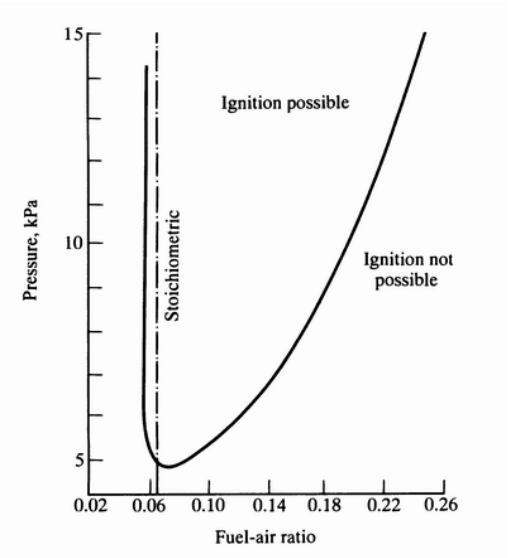

Figure 5.10. Inflammability limits of gasoline-air mixtures [Olson, 1950]

5.7.2. Aeroramp Injector Case

The calculations performed on the aeroramp grid were performed for all fuels considered, namely hydrogen, ethylene and methane. For ethylene fuel, two sets of computations were conducted, with and without the torch plume. In this section the wall static pressures and the mass fractions created by each fuel will be compared.

It is noted that only the ethylene simulations were performed on the full 1.6 million cell grid. The hydrogen and methane simulation were computed on a sequenced grid of medium resolution that had 203,000 cells. This is because the ethylene results are of primary importance, whereas only qualitative trends for the other fuels are of interest. Further, the study of Section 5.6 justifies this course of action.

5.7.2.1. Pressure Contours

Figure 5.11 presents the normalized wall static pressure distributions obtained from the simulations of ethylene, with and without the plasma torch plume operating, and also the methane and the hydrogen fuel simulations. Up to 17 d_{eq}, the two computational profiles for ethylene are identical. However, at this point, the shock from the torch plume reflects off the top wall of the tunnel, causing the two profiles to diverge slightly. The simulation that includes the plasma torch plume seems to follow the experimental data more closely, capturing the small pressure increases at 20 and 28 d_{eq}. The under-prediction of the pressure over the expansion surface (at 30 to 35 d_{eq}) first observed with the single-hole injector case is still present.

Due to the difference in injection pressure for the fuels (because different equivalence ratios were considered) the shock strength differs, and is stronger for hydrogen. This causes a slight deviation of the hydrogen profile from the hydrocarbon cases, but overall the same trends are observed.

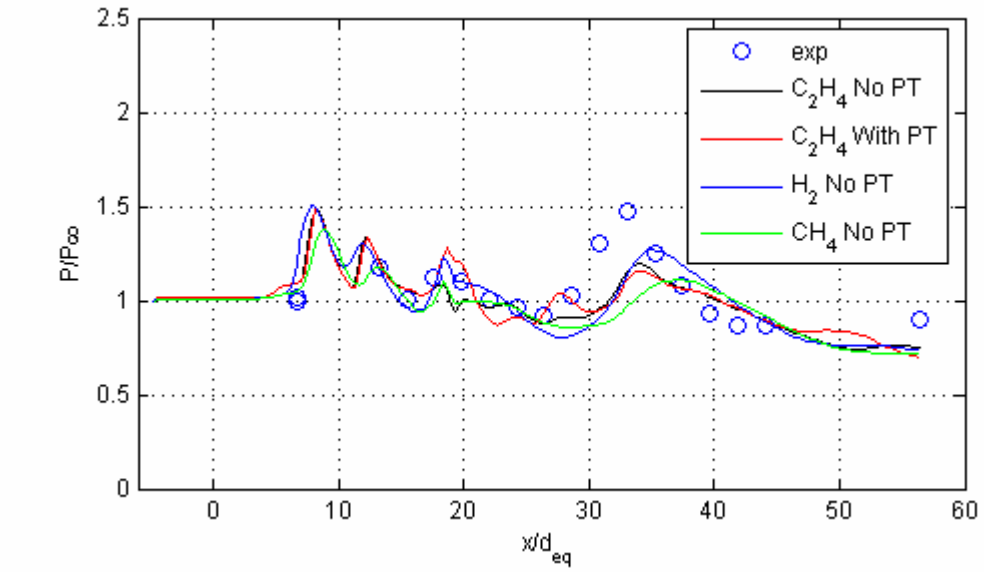

Figure 5.11. Normalized predicted wall static pressure distributions along the combustor centerline. The experimental case is compared with simulations for various fuels injected through the aeroramp with and without the plasma torch.

Figure 5.12 shows the predicted pressure contours along the tunnel symmetry plane obtained for the two cases of ethylene injection (with and without the plasma torch jet simulated) and for the hydrogen case. The bow shocks off each injector can be traced as they propagate downstream and reflect off the solid wall boundaries of the tunnel. Methane pressure contours are not shown because of their similarity to the no-torch ethylene case.

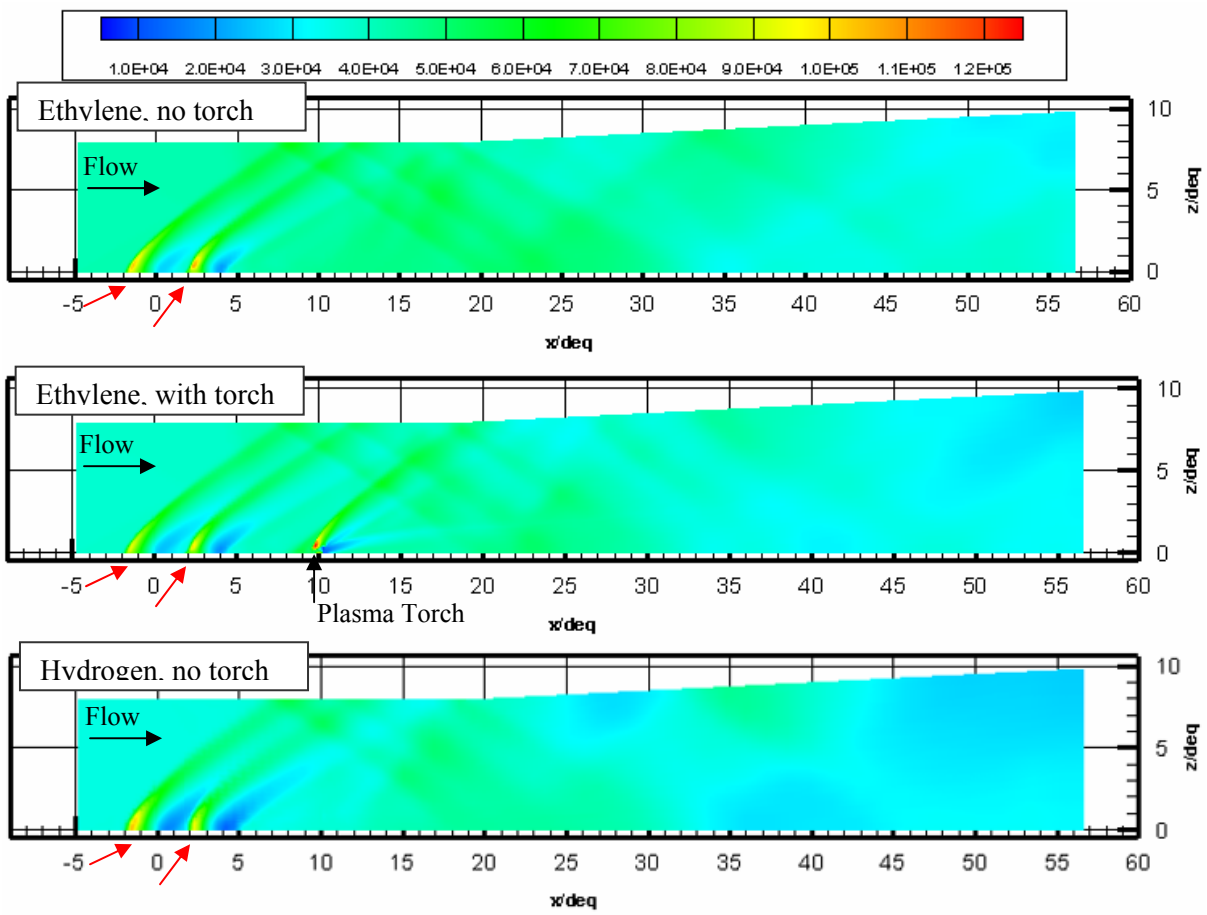

Figure 5.12. Aeroramp injector case simulations, pressure profile along symmetry plane (pressures in kPa). Top is Ethylene without the plasma torch, center is ethylene with plasma torch and bottom is hydrogen without plasma torch jet. The red arrows indicate the location of the aeroramp jets.

5.7.2.2. Mass Fraction Contours

The first feature that differentiates the aeroramp injector from the single-hole injector can be seen by comparing the mass fraction contours. Due to the transverse spacing between the two columns of the aeroramp, a stream of air is allowed to penetrate in the center of the fuel plume. This, coupled with the enhanced vorticity generated by the aeroramp, leads to faster mixing than a simple single-hole injector. Penetration achieved from the aeroramp injector is 2 d_{eq}, the same as with the single-hole injector.

By looking at the mass fraction contours at downstream stations for different fuels, the effect of the fuel molecular weight on the mixing process can be seen. Figure 5.13, Figure 5.14 and Figure 5.15 show mass fraction contours at $x/d_{eq} = 6$, 8 and 10 for ethylene, methane and hydrogen, respectively. Note here that the molecular weight of $[H_2] = 2$, of $[CH_4] = 16$ and of $[C_2H_4] = 28$. It is easily seen that the hydrogen mass fractions are considerably lower

than the corresponding ethylene and methane concentrations at each station. Indeed, at the $x/d_{eq} = 8$ station, $\alpha_{max}[C_2H_4 \& CH_4] = 0.8$, whereas $\alpha_{max}[H_2] = 0.5$.

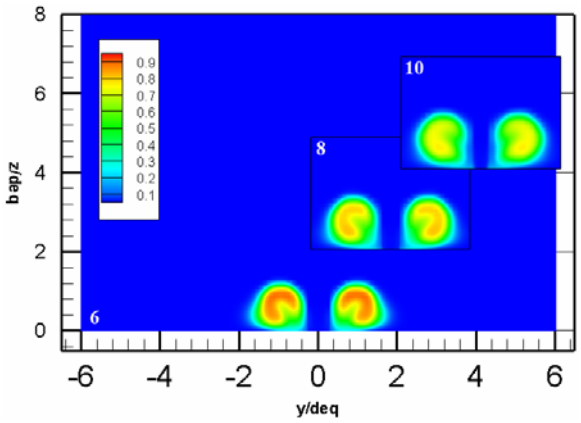

Figure 5.13. Predicted ethylene concentrations, injection via aeroramp without plasma torch

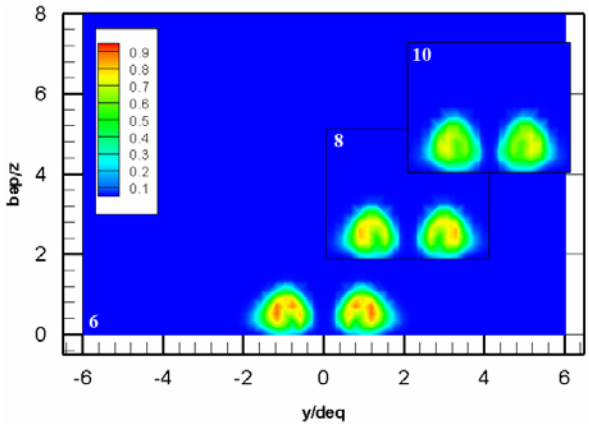

Figure 5.14. Predicted methane concentrations, injection via aeroramp with no plasma torch

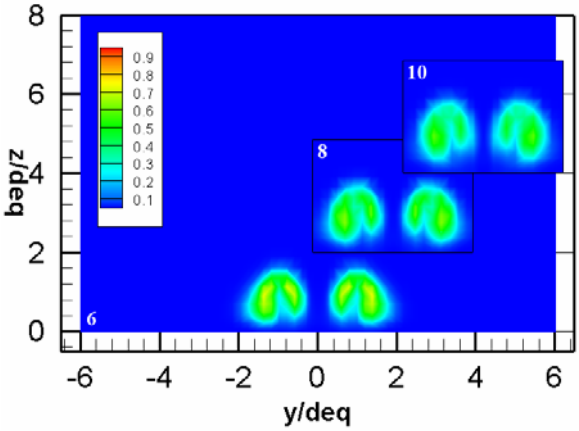

Figure 5.15. Predicted hydrogen concentrations, injection via aeroramp with no plasma torch

It was experimentally determined that for hydrogen fuel the torch can be placed at the $x/d_{eq} = 8$ station, and for ethylene fuel the torch needs to be in the $x/d_{eq} = 10$ station. The logical question that arises at this point is whether the CFD can predict the suitability of these locations, so it can be used as a design tool for other fuels and/or other conditions.

An average concentration can be determined by integrating the local values over the area of interest and dividing by the total area. The ½ x ½ d_{eq}^2 areas over which these calculations are performed are shown in Figure 5.16 for ethylene, Figure 5.17 for methane and Figure 5.18 for hydrogen. The computed values for the average concentration, α_{avg}, the local fuel-to-air ratio and the corresponding equivalence ratio, φ, are summarized in Table

5-4. Also note that the pressure in these regions remains almost constant, at 36 kPa, as with the single-hole injector case.

Fuel	α_{avg}	x/d_{eq}	fuel-to-air ratio	φ_{local}
Hydrogen	0.039	8	0.002	0.08
Ethylene	0.091	10	0.100	1.50
Methane	0.128	10	0.136	2.22

Table 5-4. Local average concentrations, fuel-to-air ratios and corresponding equivalence ratios for the region around the plasma igniter.

Flammability limits for ethylene in air at standard conditions are $0.41 < \varphi < 5.5$ (lean and rich limit [% Vol]/ [% Vol_{ST}]) and for methane are $0.53 < \varphi < 1.6$ [Glassman, 1996]. From visual extrapolation of the graph of Figure 5.10, we can determine that the conditions are sufficient for ignition of the ethylene. The methane mixture is too rich, and this is why flame propagation was not experimentally possible.

Hydrogen is known to be more reactive and more easily ignitable than hydrocarbons. Hydrogen flammability limits in air at standard conditions are $0.14 < \varphi < 2.54$ [Glassman, 1996]. Despite the difference in the experimental conditions from standard conditions, the CFD predicts that the hydrogen mixture is too lean for ignition to be possible. The fact that we do get combustion can be attributed to this difference in conditions. However, a conclusion we can draw is that the torch is not located at the most efficient location possible for the hydrogen fuel; the most upstream station (at $x/d_{eq} = 6$) might be a more suitable candidate. A higher efficiency would be experimentally manifested as less torch power required for steady combustion to be achieved.

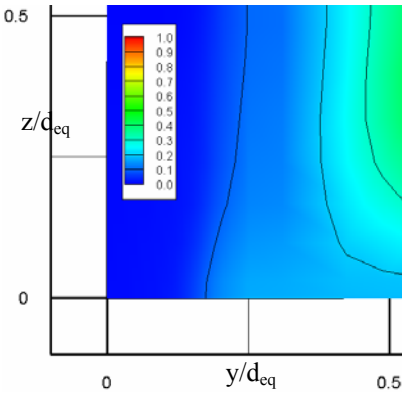

Figure 5.16. Close-up of the predicted ethylene plume at $x/d_{eq} = 10$

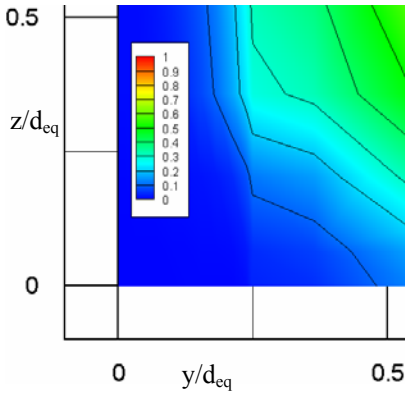

Figure 5.17. Close-up of the predicted methane plume at $x/d_{eq} = 10$

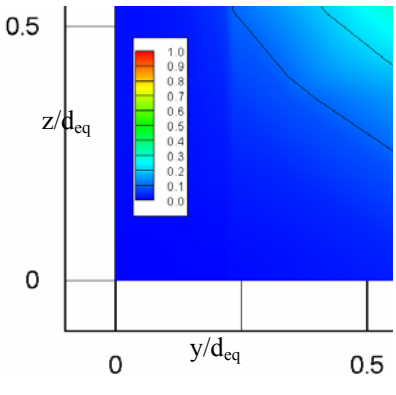

Figure 5.18. Close-up of the predicted hydrogen plume at $x/d_{eq} = 8$

One can conclude that the CFD is capable of predicting whether a given region has favorable conditions for ignition, and thus determine where to place an ignition device. The uncertainties and errors of this prediction are discussed in section "5.9. Sources of Error" below.

5.7.3. Using CFD to Predict Injector/Igniter Spacing

The CFD cases run for each fuel allow for the complete determination of the flowfield, including the pressures and mass fraction contours, as detailed above. The technique of determining the local equivalence ratio in a ½ x ½ d_{eq}^2 area can be applied to a length of the combustor, as opposed to a single station, to obtain a quantitative estimate of the mixing process and determine regions in which ignition is possible, and thus where the torch can be placed. More specifically, in Figure 5.19 (a) – (c) the local equivalence ratio, for each fuel, is plotted versus distance along the combustion and compared to the ignition limits mentioned above.

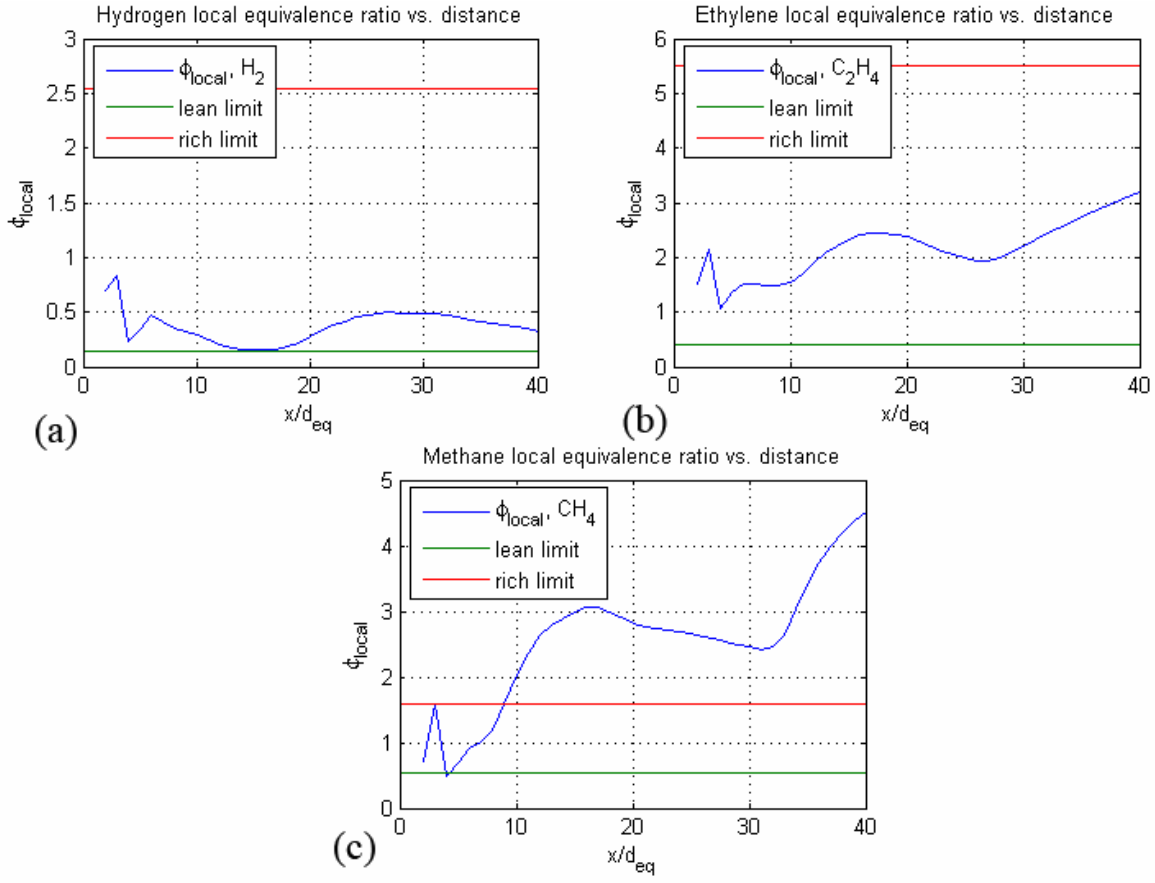

Figure 5.19 Local equivalence ratio versus distance along the combustor for (a) hydrogen, (b) ethylene and (c) methane fuels.

From considering the above plots, the following conclusions can be drawn. In general, the local equivalence ratio shows an increasing trend as the distance from the injector increases. As the fuel is mixed with the freestream air, the maximum concentration decreases, however the plume area increases, thus resulting in the increasing trend for φ_{local}.

For the hydrogen and the ethylene, the CFD predicts that the torch can be placed anywhere in the region interrogated, since φ_{local} is always within the ignition limits. Experiments with ethylene though showed that ignition was not possible with the torch in station 2. The discrepancies are due to the great uncertainties occurring from the averaging process, and also the arbitrariness by which the integration area was selected. For methane, CFD predicts that the torch should be placed further upstream than station 3 and more specifically, at a distance smaller than 8 d_{eq} from the aeroramp.

5.8. Reacting CFD calculations

Reacting CFD was performed with ethylene fuel for the aeroramp case. The torch jet was modeled as the hot jet described in section 5.5.1. The chemistry model used was a simple 3-reaction and 7-species model introduced by Baurle [1998]. The reactions modeled and the forward reaction rates are presented in Table 5-5. This model has been validated both in the aforementioned publication and by the developers of GASP® at AeroSoft.

	Reaction	C	η	ε/k
1.	$C_2H_4 + O_2 \leftrightarrow 2CO + 2H_2$	2.1 e+11†	0	18015.3
2.	$2CO + O_2 \leftrightarrow 2CO_2$	3.48 e+11‡	2	10134.9
3.	$2H_2 + O_2 \leftrightarrow 2H_2O$	3 e+14‡	-1	0
	[C]: $^{\dagger} \rightarrow [m^3/kg\text{-}mol]^2/s$ $^{\ddagger} \rightarrow [m^3/kg\text{-}mol]/s$, [ε/k]: K			

Table 5-5. Baurle's 3-equation reaction mechanism for ethylene. Rates follow $k_f = C\ T_a^{\eta} \exp[-\varepsilon/k\ T]$

The reacting simulations were performed on a sequenced aeroramp grid, with a medium mesh spacing that had 203,000 cells. The first reason for this was the required computational time. Including an extra five species (other than nitrogen and oxygen) in the chemistry model implies that five more equations need to be solved, increasing the required computational time by an order of magnitude, as can be seen by the graph of Figure 5.20. Also, the nature of these simulations is primarily to verify the ability of the CFD to predict the ignition achieved with a plasma torch and the absolute accuracy of the solution is a secondary benefit.

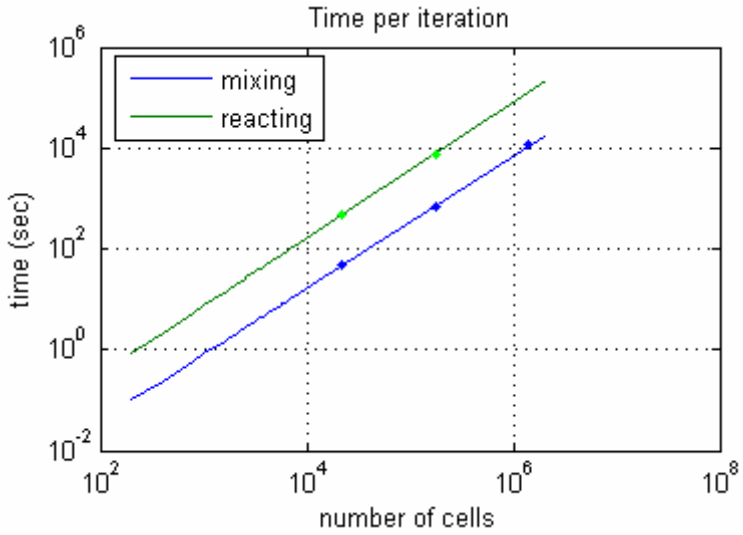

Figure 5.20. Computational time required per iteration as a function of grid points used. Note that logarithmic scales are shown. Reacting calculations which include extra species require an extra order of magnitude in time.

By representing the torch as a hot jet, it was expected to create sufficient local conditions for ignition and flame propagation. The hope was that the inclusion of all the radicals and excited species present in the actual plasma torch plume would not be necessary to model so as to achieve ignition. This, however, was not the case and the importance of the radicals in accelerating the reaction process was demonstrated. Reactions took place to an extremely limited extent. The maximum concentrations of ethylene, carbon dioxide and water are given in Table 5-6, showing how limited the combustion was.

Specie	α_{max}
C_2H_4	1
H_2O	2.31 e-13
CO_2	1.53 e-15

Table 5-6. Maximum concentrations of reactants and products for the reacting CFD case.

In order to correctly model the combustion process, a more detailed model of the plasma torch must be considered. From these calculations, however, we can conclude that the radicals known to be emitted by the plasma torch play a major role in ignition and in accelerating the reaction rates. By studying the torch plume with a spectrometer, as done by Gallimore et al. [2001], one can get a measure of these radicals to include in future calculations.

Kinetics modeling is a very challenging subject. Different reactions are important in the ignition process than in the steady combustion process, and the uncertainties in the (experimentally determined) reaction rates are very high. Further, there is a high dependence on temperature, pressure and equivalence ratio, so existing models are applicable in very narrow ranges. For example, Varatharajan and Williams [2002] present a detailed model of ethylene ignition and detonation in the range of interest to this experiment. However, the model consists of 148 reactions among 34 species, making the use of this model impractical. The kinetics modeling of plasma torch arcs is at a more primitive stage. From all this we see that an accurate representation of the kinetics is very challenging and selecting and appropriate model is key. Thus, no further efforts in simulating reacting flows were made.

5.9. Sources of Error

As with most CFD, the calculations do not match exactly with the experimental data. Several improvements can be made to the computational techniques described above that can significantly improve the quality of the solution.

First of all, the simulated combustor area physically lies downstream of a constant area isolator section. The isolator is fairly long (approximately 80 d_{eq}), allowing a boundary layer to grow. Estimates of the boundary layer thickness made at UVa [Goyne, 2004-5] conclude that the boundary layer thickness at the combustor exit is 2.6 d_{eq}, shown in Figure 5.21. Simple calculations performed on the CTBL applet [www.engapplets.vt.edu], which uses an implicit scheme for computing turbulent boundary layer thicknesses, yields similar results, namely $\delta = 2.4\ d_{eq}$ [CTBL inputs: $\gamma = 1.4$, Gas constant = 287 J/kg/K, Pr = 0.71, Sutherland law offset = 1000 K, Sutherland law slope = 1e-7, $U_e = 990$ m/s, $M_\infty = 2$, $P_\infty =$ 42,000, L = 0.26 m, 1000 x-steps, 5000 y-steps with 2e-5 step size, initial $\delta = 4.13$e-3 m (obtained from UVa data)]. Therefore, specifying an incoming boundary layer profile would increase the accuracy of the solution and make the simulation more realistic.

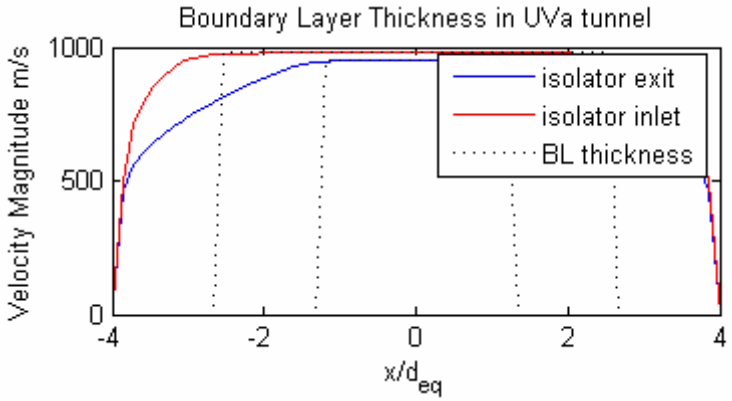

Figure 5.21. Calculated velocity profiles at isolator inlet and exit. Boundary layer thickness is calculated by taking 99% of freestream velocity value, and is shown by the dotted line.

The second consideration is the turbulence model used. Several turbulence models are available in GASP®, and the Wilcox k-ω model was selected based on its usefulness in previous simulations. The model itself though has several parameters that can be fine-tuned to obtain more accurate results, such as the turbulence intensity and the turbulent Schmidt number. A more in-depth analysis of the problem, along with more complementary experimental results, are required to get better estimates for the parameters of the turbulence models and this is why the default values were left.

Finally, there are errors introduced by the discrete nature of the grid. Increasing the grid size would help better capture all the flow features, however, this solutions comes with the increase in computational time and cost. Alternatively, higher clustering of points near the areas of interest, such as the bow shocks in front of the jets and near the solid wall surfaces, should be used to further refine the solution. Modeling into the injectors will also help eliminate errors in the injector outflow conditions and ensure that sonic injection conditions are maintained.

5.10. Conclusions

CFD calculations were performed using GASP® to model the mixing process of a fuel injected via a single-jet or aeroramp injector into a supersonic cross-flow of air. The plume of the plasma torch was modeled in the grid, but was included only in a subset of the calculations. Wall static pressures were compared with an experimental case for code and grid validation. The conclusions from the CFD study can be summarized as follows:

- For both the single-hole and the aeroramp grid, the wall static pressures were in good agreement with the experimental results, namely the maximum error was less than 10%.
- The grid successfully captures the bow shock structures caused by the injection into the supersonic cross-flow. The pressure field output can be used to see how these shocks propagate downstream and interact with the main fuel plume to increase penetration.
- Both grids predict similar fuel plume penetrations for all fuels; at the $x/d_{eq} = 8$ station plume heights of 2 d_{eq} are predicted.
- CFD predicts that the single-hole injector would NOT create suitable conditions for ignition near the region of the torch ($6 < x/d_{eq} < 10$).
- CFD confirms that the aeroramp does create favorable regions for ignition at $x/d_{eq} = 10$ with ethylene.
- For methane fuel, analysis of the near-torch region at $x/d_{eq} = 10$ shows that local concentrations are not favorable for ignition.
- CFD predicts that the $x/d_{eq} = 8$ location for the hydrogen fuel is not the best location for the torch, since the local mixture at this location is lean. Efficiency may be increased by moving the torch to the $x/d_{eq} = 6$ station to get richer mixtures.
- The inability of the simplified reacting simulations to capture the combustion process indicates the importance of modeling the torch correctly, i.e., including all radicals and excited species in the torch plume.
- The existing grids can be used with different chemistry models to aid in the design of future experiments. By changing the fuel and looking at the mass fraction contours predicted, one can find with fair confidence a suitable location for the plasma torch.
- Including an initial boundary layer profile in the inflow conditions may significantly increase the quality of the solution.
- Better turbulence modeling is probably needed to more accurately predict the mixing.

6. Conclusions and Recommendations

6.1. Conclusions

A novel integrated injector-igniter system for scramjet engines was tested in a Mach 2, heated, continuous flow facility. Combustion was determined by considering the increase in wall-static pressures caused by the heat release of the combusting fuel. Supersonic combustion was demonstrated with hydrogen and ethylene fuels, while methane was also tested. The integrated aeroramp injector/plasma-torch igniter configuration, with hydrogen and ethylene fuels, performed well through the full operating range of the facility, i.e., yielding combustor entrance pressures ranging from the freestream pressure at the isolator inlet (supersonic combustion) and pressure rise near that corresponding to a normal shock in the isolator (subsonic combustion mode). Both subsonic and supersonic combustion where achieved in the air total temperature variation study. The lower limits presented here are facility and operational limits, not combustion limits. Although only minimal pressure rises were obtained with methane, good steps were taken towards understanding what modifications need to be made for the system to work.

The wall-static pressure profiles were analyzed to obtain engine performance characteristics, such as air and fuel specific impulses, and combustion efficiency. These were determined by employing the industry standard Ramjet Propulsion Analysis code (RJPA). In the supersonic combustion mode, the hydrogen fuel yielded higher combustion efficiencies, around 80%, whereas for ethylene this number decreased to around 60%. In the subsonic combustion mode the efficiencies were 51% and 40% for hydrogen and ethylene respectively. For both fuels, air specific impulses ranged from 10-25 seconds were obtained. Computed fuel specific impulses fell within the theoretically predicted ranges for scramjets at similar flight conditions.

CFD was employed to further understand the fuel-air mixing process. Fuel mass fractions in a region near the proposed torch location were analyzed to determine whether local conditions favored ignition and flame propagation or not. This study helped explain

why the experiments with methane were unsuccessful (local conditions are too fuel-rich) and verified that indeed good locations have been selected for hydrogen and ethylene fuels.

In summary, the final conclusions obtained are:

- The flush-wall integrated aerodynamic-ramp-injector/plasma-torch-igniter was successfully demonstrated for the first time to be a workable system in realistic scramjet-combustor conditions. Further, the complete engine analysis of RJPA shows that the performance is similar to theoretically predicted results for scramjets.
- Good operational locations of the plasma torch were determined for hydrogen and ethylene fuels, namely at 8 and 10 equivalent diameters respectively. CFD also supports the experimental findings regarding torch location for these fuels.
- For hydrogen fuel:
    - For the base case condition of T_o = 1000 K, operability ranges were determined to be $0.07 < \varphi < 0.31$ and combustion efficiencies in the supersonic combustion mode were on average 81%, reduced to 51% in the dual-mode combustion.
    - Excellent agreement in wall-static pressure profiles were obtained between the aeroramp and a physical 10-degree compression ramp.
    - Combustion (both subsonic and supersonic) was achieved at total temperatures as low as 530K. This was a facility limit and not an extinction limit.
- For ethylene fuel:
    - For the base case condition of T_o = 1000 K, operability ranges were determined to be $0.14 < \varphi < 0.48$ and combustion efficiencies in the supersonic combustion mode were on average 62%, reduced to 40% in the dual-mode combustion.
    - Combustion was achieved at total temperatures as low as 680K.
- The engine performs similarly independent of fuel, as determined by the air-specific impulse results. Air specific impulses are between 10 and 25 seconds, varying with equivalence ratio
- Fuel specific impulses were on average 3000 sec for hydrogen and 1000 sec for ethylene, in good agreement with theoretical predictions.
- For methane fuel:

- Limited heat release was obtained. This result, coupled with the long ignition delay time of methane leads to the conclusion that the torch needs to be placed further downstream.
- CFD analysis of the near-torch region at $x/d_{eq} = 10$ shows that local concentrations are not favorable for ignition.

- For both the single-hole and the aeroramp grid, the wall static pressures were in good agreement with the experimental results, namely the maximum error was less than 10%.
- CFD predicts similar fuel plume penetrations for all fuels; at the $x/d_{eq} = 8$ station plume heights of 2 d_{eq} are predicted.
- The existing grids can be used with different chemistry models to aid in the design of future experiments. By changing the fuel and looking at the mass fraction contours predicted, one can find with fair confidence a suitable location for the plasma torch.

6.2. Future Recommendations

Several improvements can be made to improve the quality of data obtained, analysis performed and phenomena explored.

First of all, regarding the experimental data, the use of the NetScanner pressure acquisition system (described in 2.4.3.2) increases the accuracy of the results by eliminating the time variable. All pressure measurements are obtained simultaneously, so variations due to changes in the plasma torch due to erosion or other unsteadiness are not observed. If possible, this is the preferable method of data acquisition for future work.

Obviously, an integral part of this study is the aeroramp/torch integration. This should be done as a coupled CFD and experimental study, and more specifically, CFD should be used for the hardware design. This would lead to a better design of the available anode locations, increasing the possibility of success with methane fuel. Another factor that can be investigated with methane is the effect of the feedstock pressures and feedstock gas. Ionizing the gas produces radicals that affect the reaction rates. However, different radicals might be responsible for initiating the combustion and different ones for enhancing it. A different feedstock (nitrogen, hydrogen or another hydrocarbon), might produce the radicals required to initiate combustion, again enhancing the possibility of success with methane.

A more complete investigation of the operating limits for all fuels can be done. Aside from varying the air total temperature, the total pressure can also be varied and a map of operating conditions can be made for the specific engine geometry through the use of RJPA.

The plasma torch provides a robust and repeatable ignition source. However, its use for flameholding, while feasible, provides some additional challenges. Torch life is limited to minutes of continuous operation due to erosion; the most achieved in these experiments was 45 minutes. So, it would be of interest to investigate other means of flameholding that follow the flush-wall design mentality. Such a method could be the use of a catalyst to accelerate the reaction rates, or even initiate them without the plasma torch. Early experiments of Billig and Grenleski [1966] come to mind, where platinum was used in conjunction with hydrogen fuel to lower auto-ignition requirements on total temperature.

The nature of the facility, specifically the small cross-sectional area and the steel water-cooled walls, does not lend itself well for direct flow measurements. Drilling holes to insert a movable pressure or concentration probe poses significant logistical difficulties. However, optical access is available to the flow and so non-intrusive laser diagnostics can be employed to determine flow quantities. More specifically, PIV (Particle Image Velocimetry) can be employed to get velocity profiles that can be compared to the numerical simulations. This can be done by seeding the fuel stream with particles and tracking them as they proceed downstream. A two-dimensional PIV system currently exists [Goyne, 2001] and a stereo-PIV system is being set up in the UVA-SCF [Smith, 2005], so the slight modification required to adapt to the aeroramp injector system might be worth the effort for the quality and quantity of data that can be obtained.

An interesting feature to investigate directly would be the heat release from the combustion, which could be done by installing calorimeters in the facility. This would allow for a more direct comparison with the RJPA data and serve as its verification, as heat release rates could be directly compared.

In the interest of minimizing the overall system weight, some modifications can be made to the plasma torch system. A “mini-torch” has been designed that eliminates part of the anode body and air supply tube length, reducing the overall torch length and weight.

Several improvements can be made to the CFD study as well. As machine efficiency and number of processors increase, more cells can be used to model the injector refining the solution. An interesting comparison would be one between different solver types, namely an LES (Large Eddy Simulation) or even perhaps DNS (Direct Numerical Simulation) code to

be compared with the RANS-type GASP® solver. LES solvers are more suitable for boundary layer mixing type flows, which is what the current investigation involves.

Including the upstream boundary layer profile in the incoming flow and refining the turbulence model can also improve the quality of the solution. A study can be made using several different turbulence models and varying parameters such as turbulence intensity in each.

A reacting-flow numerical calculation would be very interesting. Determining the appropriate chemical kinetics model will be a challenge, but once this is established the reacting pressure profiles can be computed again to serve as a complement to the RJPA study, yielding combustion efficiency and heat release data.

Studies on liquid jet injection in supersonic flows have shown that the jets are in fact not steady, but are oscillating at extremely high frequencies (order of 500 kHz). In a recent preliminary study to determine whether the gaseous aeroramp oscillates, the injector was examined visually with high-speed schlieren movies. These movies showed some unsteadiness present in the bow shock prior to the injectors caused by oscillations in the jets, although the sampling rate was not high enough to determine a frequency. So, simulating the injection and mixing process as unsteady and without a symmetry plane could give better results.

References

1. AeroSoft Corporation, "GASP v.4.2 Reference Guide", Blacksburg, VA, April 2004.
2. Analog Devices, www.analog.com, "Precision, Wide Bandwidth 3-Port Isolation Amplifier AD210*", 2005.
3. C.D. Anderson, J.A. Schetz, "Liquid-Fuel Aeroramp Injector for Scramjets", Journal of Propulsion and Power, Vol. 21, No. 2, March-April 2005.
4. J.D. Anderson, *Modern Compressible Flow with Historical Perspective*, Third Edition, McGraw Hill, 2003.
5. E.H. Andrews, E.A. Mackley, "Review of NASA's Hypersonic Research Engine Project", AIAA-1993-2323, Originally presented at 29th AIAA/ASME/ SAE/ASEE Joint Propulsion Conference and Exhibit, Monterey, CA, 1993.
6. ARL – Aerospace Research Laboratory of University of Virginia, 2004, http://www.mae.virginia.edu/arl/
7. E. Barbi, "Uncooled Choked Plasma Torch for Ignition and Flameholding in Supersonic Combustion", Masters Thesis, Virginia Polytechnic Institute & State University, 1986.
8. R.A. Baurle, T. Mathur, M.R. Gruber, K.R. Jackson, "A Numerical and Experimental Investigation of a Scramjet Combustor for Hypersonic Missile Applications", AIAA 1998-3121, Originally presented at 34th AIAA/ASME/ SAE/ASEE Joint Propulsion Conference and Exhibit, Cleveland, OH, 1998.
9. A. Ben-Yakar, R.K. Hanson, "Experimental Investigation of Flame-Holding Capability of Hydrogen Transverse Jet in Supersonic Crossflow", 27th Symposium (International) on Combustion, The Combustion Institute, 1998, pp. 2173-2180.
10. A. Ben-Yakar, R.K. Hanson, "Cavity Flame-Holders for Ignition and Flame Stabilization in Scramjets: An Overview", Journal of Propulsion and Power, Vol. 17, No. 4, July-August 2001.
11. F.S. Billig, S.E. Grenleski, "Experimental Studies of Hydrogen-Air Ignition in a Supersonic Combustor", JHU-APL Technical Memorandum, TG-848, Originally presented at the AIAA Joint Propulsion Specialists Conference, Colorado Springs, CO, 1966.
12. F.S. Billig, "Research on Supersonic Combustion", Journal of Propulsion and Power, Vol. 9, No. 4, July-August 1993.

13. F.S. Billig, Personal Communications, 2004-2005.
14. D.C.C. Chen, J. Lawton, F.J. Weinberg, "Augmenting Flames with Electric Discharges", Tenth Symposium (International) on Combustion, The Combustion Institute, 1965.
15. M.B. Colket, L.J. Spadaccini, "Scramjet Fuels Autoignition Study", Journal of Propulsion and Power, Vol. 17, No. 2, March-April 2001.
16. S.K. Cox-Stouffer, R.P. Fuller, J.A. Schetz, R.W. Walters, "Vortical Interactions Generated by an Injector Array to Enhance Mixing in Supersonic Flow", AIAA-1994-0708, Originally presented at the 32nd Aerospace Sciences Meeting and Exhibits, Reno, NV, 1994.
17. S.K. Cox-Stouffer, M.R. Gruber, "Effects of Spanwise Injector Spacing on Mixing Characteristics of Aerodynamic Ramp Injectors", AIAA-1998-3272.
18. S.K. Cox-Stouffer, M.R. Gruber, "Effects of Injector Yaw on Mixing Characteristics of Aerodynamic Ramp Injectors", AIAA-1999-0086, Originally presented at the 37th Aerospace Sciences Meeting and Exhibit, Reno, NV, 1999.
19. S.K. Cox-Stouffer, M.R. Gruber, "Further Investigation of the Effects of "Aerodynamic Ramp" Design upon Mixing Characteristics", AIAA-1999-2238, Originally presented at the 35th AIAA/ASME/SAE/ASEE Joint Propulsion Conference and Exhibit, Los Angeles, CA, 1999.
20. E.T. Curran, W.H. Heiser, D.T. Pratt, "Fluid Phenomena in Scramjet Combustion Systems", Annual Review of Fluid Mechanics, 1996, 28:323-360.
21. E.T. Curran, S.N.B. Murthy (Editors), *Scramjet Propulsion*, Progress in Astronautics and Aeronautics, Volume 189, AIAA, 2000.
22. D.L. Davis, R.D.W. Bowersox, "Computational Fluid Dynamics Analysis of Cavity Flame Holders for Scrmajets", AIAA-1997-3270.
23. D.O. Davis, W.R. Hingst, " Progress Toward Synergistic Hypermixing Nozzles", AIAA-1991-2264, Originally presented at 27th AIAA/ASME/SAE/ASEE Joint Propulsion Conference and Exhibit, Sacramento, CA, 1991.
24. G.S. Diskin, G.B. Northam, "Evaluation of Storable Fluorine Based Pilot for Scramjets", AIAA-1986-0372, Originally presented at 24th Aerospace Sciences Meeting, Reno, NV, 1986.
25. S.E. Doerner, A.D. Cutler, "Effects of Jet Swirl on Mixing of a Light Gas Jet in a Supersonic Airstream", NASA/CR-1999-209842, December 1999.
26. G.L. Dugger, "A Future for Hypersonic Ramjets", Astronautics, April 1959.

27. G.L. Dugger, F.S. Billig, “Recent Work in Hypersonic Propulsion at the Applied Physics Laboratory, the Johns Hopkins University”, Johns Hopkins University, Applied Physics Laboratory, TG-355, Laurel, MD, 1959.
28. G.L. Dugger, F.S. Billig, “Ramjet Technology, Chapter 11, Hypersonic Ramjets”, JHU-APL TG 610-11, March 1970.
29. DuPont, www.dupont.com, “Properties of DuPont Vespel® Parts”, 2005.
30. D.R. Eklund, M.R. Gruber, “Study of a Supersonic Combustor Employing an Aerodynamic Ramp Pilot Injector”, AIAA-1999-2249, Originally presented at the 35th AIAA/ASME/SAE/ASEE Joint Propulsion Conference and Exhibit, Los Angeles, CA, 1999.
31. Engineering Applets, www.engapplets.vt.edu.
32. A. Ferri, “Possible Directions of Future Research in Air-Breathing Engines”, Fourth AGARD Combustion and Propulsion Colloquium, Milan, Italy, April 1960, Pergamon, New York, 1960, pp. 3-15.
33. A. Ferri, “Review of Problems in Application of Supersonic Combustion”, The Seventh Lanchester Memorial Lecture, Royal Aeronautical Society, London, England, 1964.
34. A. Ferri, “Mixing-Controlled Supersonic Combustion”, Annual Review of Fluid Mechanics, Vol. 5, pp. 301-338, 1973.
35. L.E. Foster, W.A. Engblom, “Computation of Transverse Injection into Supersonic Crossflow with Various Injector Orifice Geometries”, NASA TM/–2003-212878 (AIAA-2004-1199).
36. E.J. Fuller, R.B. Mays, R.H. Thomas, J.A. Schetz, “Mixing Studies of Helium in Air at High Supersonic Speeds”, AIAA Journal, Vol. 30, No. 9, September 1992.
37. R.P. Fuller, P.K. Wu, A.S. Nejad, J.A. Schetz, “Fuel-Vortex Interactions for Enhanced Mixing in Supersonic Flow”, AIAA-1996-2661, Originally presented at 32nd AIAA/ASME/SAE/ASEE Joint Propulsion Conference and Exhibit, Lake Buena Vista, FL, 1996.
38. R.P. Fuller, P.K. Wu, A.S. Nejad, J.A. Schetz, “Comparison of Physical and Aerodynamic Ramps as Fuel Injectors in Supersonic Flow”, Journal of Propulsion and Power, Vol. 14, No. 2, March-April 1998.
39. J.E. Funk, S.D. Heister, R. Humble, N. Purcell, “Development Testing of Non-Toxic, Storable Hypergolic Liquid Propellants”, AIAA-1999-2878, Originally presented at 35th AIAA/ASME/SAE/ASEE Joint Propulsion Conference and Exhibit, Los Angeles, CA, 1999.

40. S.D. Gallimore, A Study of Plasma Ignition Enhancement for Aeroramp Injectors in Supersonic Combustion Applications, PhD Dissertation, Blacksburg VA, 2001.
41. S.D. Gallimore, L.S. Jacobsen, J.A. Schetz, W.F. O'Brien, "An Integrated Aeroramp Injector/Plasma-Igniter for Hydrocarbon Fuels in a Supersonic Flow, Part B: Experimental Studies of the Operating Conditions", AIAA-2001-1767, Originally presented at the 10th International Space Planes and Hypersonic Systems and Technologies Conference, Kyoto, Japan, 2001
42. H.E. Gilreath, "The Beginning of Hypersonic Ramjet Research at APL", Johns Hopkins APL Technical Digest, Vol. 11, No. 3 and 4, 1990.
43. I. Glassman, *Combustion*, Third Edition, Academic Press, 1996.
44. C.P. Goyne, J.C. McDaniel, R.H. Krauss, S.W. Day, "Velocity Measurement in a Dual-Mode Supersonic Combustor Using Particle Image Velocimetry", AIAA-2001-1761.
45. C.P. Goyne, J.C. McDaniel, T.M. Quagliaroli, R.H. Krauss, S.W. Day, "Dual-Mode Combustion of Hydrogen in a Mach-5, Continuous Flow Facility", Journal of Propulsion and Power, Vol. 17, No. 6, November-December 2001.
46. C.P. Goyne, Personal communications, 2004-2005.
47. M. Grimes, W. Harris, E. O'Hair, L. Hatfield, M. Kristiansen, M. Baker, "Continuous Characteristic V-I Curves for a 30kWe Nitrogen Arcjet", AIAA-1991-2225, Originally presented at 27th AIAA/ASME/SAE/ASEE Joint Propulsion Conference and Exhibit, Sacramento, CA, 1991.
48. M.R. Grubber, A.S. Nejad, J.C. Dutton, "Circular and Elliptical Transverse Injection Into a Supersonic Crossflow – The Role of Large Scale Structures", AIAA-1995-2150, Originally presented at the 26th Fluid Dynamics Conference, San Diego, CA, 1995.
49. M.R. Gruber, R.A. Baurle, T. Mathur, K.Y. Hsu, "Fundamental Studies of Cavity-Based Flameholder Concepts for Supersonic Combustor", AIAA-1999-2248, Originally presented at 35th AIAA/ASME/SAE/ASEE Joint Propulsion Conference and Exhibit, Los Angeles, CA, 1999.
50. A.J. Harrison, F.J. Weinberg, "Flame Stabilization by Plasma Jets", Proceedings of the Royal Society of London, Vol. 321, 1971.
51. R.J. Hartfield, S.D. Hollo, J.C. McDaniel, "Experimental Investigation of a Supersonic Swept Ramp Injector Using Laser-Induced Iodine Fluorescence", Journal of Propulsion and Power, Vol. 10, No. 1, January-February 1994.
52. W.H. Heiser, D.T. Pratt, *Hypersonic Airbreathing Propulsion*, AIAA Educational Series, 1994.

53. P. Hill, C. Peterson, *Mechanics and Thermodynamics of Propulsion*, Second Edition, Addison Wesley, 1992.
54. J.P. Holman, *Heat Transfer*, Seventh Edition, McGraw Hill, 1990.
55. L.S. Jacobsen, J.A. Schetz, W.F. Ng, "The Flowfield Near a Multiport Injector Array in a Supersonic Flow", AIAA-1998-3126.
56. L.S. Jacobsen, J.A. Schetz, S.D. Gallimore, W.F. O'Brien, "Mixing Enhancement by Jet Swirl in a Multiport Injector Array in Supersonic Flow", FEDSM99-7248, Originally presented at the 3rd ASME/JSME Joint Fluids Engineering Conference, 1999.
57. L.S. Jacobsen, "An Integrated Aerodynamic-Ramp-Injector/Plasma-Torch-Igniter for Supersonic Combustion Applications with Hydrocarbon Fuels", PhD Dissertation, Virginia Polytechnic Institute & State University, 2001.
58. L.S. Jacobsen, S.D. Gallimore, J.A. Schetz, W.F. O'Brien, L.P. Goss, "An Integrated Aeroramp Injector/Plasma-Igniter for Hydrocarbon Fuels in a Supersonic Flow, Part A: Experimental Studies of the Geometric Configuration", AIAA-2001-1766, Originally presented at the 10th International Space Planes and Hypersonic Systems and Technologies Conference, Kyoto, Japan, 2001.
59. L.S. Jacobsen, S.D. Gallimore, J.A. Schetz, W.F. O'Brien, L.P. Goss, "Improved Aerodynamic-Ramp Injector in Supersonic Flow", Journal of Propulsion and Power, Vol. 19, No. 4, July-August 2003.
60. L.S. Jacobsen, Personal communications, 2004.
61. R.H. Krauss, J.C. McDaniel, "A Clean Air Continuous Flow Propulsion Facility", AIAA Paper 92-3912, July 1992.
62. R.H. Krauss, J.C. McDaniel, J.E. Scott, R.B. Whitehurst, C. Segal, G.T. Mahoney, J.M. Childers, "Unique, Clean-Air, Continuous Flow, High-Stagnation Temperature Facility for Supersonic Combustion Research", AIAA Paper 88-3509, July 1988.
63. P. Kutschenreuter, "Supersonic Flow Combustors", Scramjet Propulsion, Chapter 8, Progress in Astronautics and Aeronautics, Vol. 189, 2000.
64. D.B. Le, C.P. Goyne, R.H. Krauss, J.C. McDaniel, "Experimental Study of a Dual-Mode Scramjet Isolator", AIAA 2005-23, Originally presented at 43rd AIAA Aerospace Sciences Meeting and Exhibit, Reno, 2005.
65. M.H. Loh, M.A. Cappelli, "Supersonic DC-Arcjet Plasma at Subtorr Pressures as a Medium for Diamond Film Synthesis", AIAA-1992-3534, Originally presented at 28th AIAA/ASME/SAE/ASEE Joint Propulsion Conference and Exhibit, Nashville, TN, 1992.

66. M.P. Loomis, E. Venkatapathy, P. Papadopoulos, C.B. Davies, S. Berry, T. Horvath, C. Campbell, "Aeroheating and Aerodynamic CFD Validation and Prediction For the X-38 Program", AIAA-1997-2478, Originally presented at the 32nd Thermodynamics Conference, Atlanta, GA, 1997.
67. L. Maddalena, T.L. Campioli, J.A. Schetz, "Experimental and Computational Investigation of an Aeroramp Injector in a Mach Four Cross Flow", AIAA-2005-3235, Originally presented at the 13th International Space Planes and Hypersonic Systems and Technologies Conference, Capua, Italy, 2005.
68. T. Mathur, G. Streby, M. Gruber, K. Jackson, J. Donbar, W. Donaldson, T. Jackson, C. Smith, F. Billig, "Supersonic Combustion Experiments with a Cavity-Based Fuel Injector", AIAA-1999-2102, Originally presented at 35th AIAA/ASME/SAE/ASEE Joint Propulsion Conference and Exhibit, Los Angeles, CA, 1999.
69. R.B. Mays, R.H. Thomas, J.A. Schetz, "Low Angle Injection into a Supersonic Flow", AIAA-1998-2461, originally presented at 25th Joint Propulsion Conference, Monterey, CA, 1989.
70. R. Minato, T. Niioka, "Effect of Hydrogen Jet Position Relative to Plasma Torch on Supersonic Combustion", AIAA-2003-6908, Originally presented at 12th International Space Planes and Hypersonic Systems and Technologies Conference, Norfolk, VA, 2003.
71. T.O. Mohieldin, S.N. Tiwari, "Effects of Tandem Injection on Compressible Turbulent Shear Layer", AIAA-1998-1638, Originally presented at 8th International Space Planes and Hypersonic Systems and Technologies Conference, Norfolk, VA, 1998.
72. P.L. Moses, "X-43C Plans and Status", AIAA-2003-7084, Presented at 12th AIAA International Space Planes and Hypersonic Systems and Technologies Conference, Norfolk, VA, 2003.
73. K. Murakami, A. Nishikawa, K. Takita, G. Masuya, "Ignition Characteristics of Hydrocarbon Fuels by Plasma Torch in Supersonic Flow", AIAA-2003-6939, Originally presented at 12th International Space Planes and Hypersonic Systems and Technologies Conference, Norfolk, VA, 2003.
74. R. Neel, A. Godfrey, D. Slack, "Turbulence Model Validation in GASP Version 4", AIAA-2003-3740, Originally presented at 33rd AIAA Fluid Dynamics Conference and Exhibit, Orlando, FL, 2003.
75. G.B. Northam, C.R. McClinton, T.C. Wagner, W.F. O'Brien, "Development and Evaluation of a Plasma Jet Flameholder for Scramjets", AIAA-1984-1408, Originally presented at 20th AIAA/SAE/ASME Joint Propulsion Conference, Cincinnati, OH, 1984.

76. G.B. Northam, A.G. McLain, G.L. Pellet, G. Diskin, “Effect of Silane Concentration on the Supersonic Combustion of a Silane/Methane Mixture”, AIAA-1986-1396, Originally presented at the 22nd AIAA/ASME/SAE/ASEE Joint Propulsion Conference, Huntsville, AL, 1986.
77. G.B. Northam, I. Greenberg, C.S. Byington, D.P. Capriotti, “Evaluation of Parallel Injection Configurations for Mach 2 Combustion”, Journal of Propulsion and Power, Vol. 8, No. 2, March-April 1992.
78. W.T. Olson, J.H. Childs, E.R. Jonash, "Turbojet Combustor Efficiency at High Altitudes," NACA RM E50I07, October, 1950.
79. Omega Engineering Inc., www.omega.com, “The Omega® Temperature Handbook and Encyclopedia”, Vol. MMV™, 5th Edition, 2001.
80. P.H. Oosthuizen, W.E. Carscallen, *Compressible Fluid Flow*, McGraw-Hill Series in Mechanical Engineering, 1997.
81. P.P. Pandolfini, M.A. Friedman, “Instructions for Using Ramjet Performance Analysis (RJPA) IBM-PC Version 1.24”, JHU/APL AL-92-P175, June 1992.
82. J.L. Perbola, “Performance of a Plasma Torch with Hydrocarbon Feedstocks for Use in Scramjet Combustion”, Masters Thesis, Virginia Polytechnic Institute & State University, 1998.
83. Pressure Systems, Inc., www.pressuresystems.com, Rackmount Intelligent Pressure Scanners User’s Manual (Model 98RK & Model 9816), 2000.
84. D.W. Riggins, C.R. McClinton, R.C. Rogers, R.D. Bittner, “Investigation of Scramjet Injection Strategies for High Mach Number Flows”, Journal of Propulsion and Power, Vol. 11, No. 3, May-June 1995.
85. D.W. Riggins, P.H. Vitt, “Vortex Generation and Mixing in Three-Dimensional Supersonic Combustors”, Journal of Propulsion and Power, Vol. 11, No. 3, May-June 1995.
86. R.C. Roggers, D.P. Capriotti, R.W. Guy, “Experimental Supersonic Combustion Research at NASA Langley”, AIAA-1998-2506, Originally presented at 20th AIAA Advanced Measurement and Ground Testing Technology Conference, Albuquerque, NM, 1998.
87. P.M. Rubins, R.C. Bauer, “A Review of Supersonic Combustion Research at AEDC with Hypersonic Applications”, AIAA-1993-2326, Originally presented at the 29th AIAA/ASME/SAE/ASEE Joint Propulsion Conference and Exhibit, Monterey, CA, 1993.

88. T.W. Ryan, S.T. Schwab, W.W. Harlowe, "Aluminum Alkyl Derivatives – Ignition and Combustion Enhancers for Supersonic Combustors", Journal of Propulsion and Power, Vol. 11, No. 1, January-February 1995.
89. J.A. Schetz, *Injection and Mixing in Turbulent Flow*, Progress in Astronautics and Aeronautics, Vol. 68, AIAA, 1980.
90. J.A. Schetz, R.H. Thomas, F.S. Billig, "Mixing of Transverse Jets and Wall Jets in Supersonic Flow", Separated Flows and Jets, IUTAM Symposium, Novosibirsk, USSR, 1990.
91. J.A. Schetz, *Boundary Layer Analysis*, Prentice Hall, 1993.
92. J.A. Schetz, S. Cox-Stouffer, R. Fuller, "Integrated CFD and Experimental Studies of Complex Injectors in Supersonic Flows", AIAA-1998-2780.
93. J.A. Schetz, Personal Communications, 2005.
94. Sierra Instruments, Inc., www.sierrainstruments.com, Sierra Series 830/840/860 Mass Flow Meter and Controller Instruction Manual, Sierra Instruments, 1994.
95. M. Situ, Y.Y. Sun, S.D. Zhang, C. Wang, "Investigation of Supersonic Combustion of Hydrocarbon Fuel-Riched Hot Gas in Scramjet Combustor", AIAA-1999-2245, Originally presented at 35th AIAA/ASME/SAE/ASEE Joint Propulsion Conference and Exhibit, Los Angeles, CA, 1999.
96. C.T. Smith, C.P. Goyne, R.H. Krauss, J.C. McDaniel, "Development of a Three-component Particle Image Velocimetry Technique for a Scramjet Combustor", AIAA-2005-4104, Originally presented at the 41st AIAA/ASME/SAE/ASEE Joint Propulsion Conference & Exhibit, Tucson, AZ, 2005.
97. S. Stouffer, "Development and Operating Characteristics of an Improved Plasma Torch for Supersonic Combustion Applications", Masters Thesis, Virginia Polytechnic Institute & State University, July 1989.
98. S.D. Stouffer, N.R. Baker, D.P. Capriotti, G.B. Northam, "Effects of Compression and Expansion-Ramp Fuel Injector Configurations on Scramjet Combustion and Heat Transfer", AIAA-1993-0609, Originally presented at 31st Aerospace Sciences Meetings, Reno, NV, 1993.
99. J. Swithenbank, "Hypersonic Air-Breathing Propulsion", Progress In Aeronautical Sciences, Vol. 8, Pergamon Press, 1966.
100. K. Takita, T. Sato, Y. Ju, G. Masuya, "Effects of Addition of Radicals Supplied by Plasma Torch on Burning Velocity", AIAA-1999-2247, Originally presented at 35th

AIAA/ASME/SAE/ASEE Joint Propulsion Conference and Exhibit, Los Angeles, CA, 1999.

101. S. Tomioka, L.S. Jacobsen, J.A. Schetz, "Sonic Injection from Diamond-Shaped Orifices Into a Supersonic Crossflow", Journal of Propulsion and Power, Vol. 19, No. 1, January-February 2003.

102. United Aircraft Research Laboratories, "Hydrocarbon-Fueled Scramjet", Report J910755-25, 1970.

103. B. Varatharajan, F.A. Williams, "Ethylene Ignition and Detonation Chemistry, Part 1: Detailed Modeling and Experimental Comparison", Journal of Propulsion and Power, Vol. 18, No. 2, March-April 2002.

104. V. Viti, J. Schetz, R. Neel, "Numerical Studies of the Jet Interaction Flowfield with a Main Jet and an Array of Smaller Jets", ICAS 2002-4.7.1, 23rd International Congress of Aeronautical Sciences, 2002.

105. T.C. Wagner, W.F. O'Brien, G.B. Northam, J.M. Eggers, "Plasma Torch Igniter for Scramjets", Journal of Propulsion, Vol. 5, No. 5, 1989. Originally presented at the 23rd JANNAF Combustion Meeting, 1986.

106. I.A. Waitz, F.E. Marble, E.E. Zukoski, "Investigation of a Contoured Wall Injector for Hypervelocity Mixing Augmentation", AIAA Journal, Vol. 31, No. 6, June 1993.

107. S. Wallis, "Innovative Transverse Jet Interaction Arrangements in Supersonic Crossflow", Masters Thesis, Virginia Polytechnic Institute & State University, 2001.

108. A.M. Warris, F.J. Weinberg, "Ignition and Flame Stabilization by Plasma Jets in Fast Gas Streams", Twentieth Symposium (International) on Combustion, The Combustion Institute, 1985.

109. F.J. Weinberg, "Plasma Jets in Combustion", Institute of Mechanical Engineers, London, Paper C 45/83. 1983.